NUMERICAL MODELING OF FRACTURE PERMEABILITY CHANGE IN NATURALLY FRACTURED RESERVOIRS USING A FULLY COUPLED DISPLACEMENT DISCONTINUITY METHOD

A Dissertation

by

QINGFENG TAO

Submitted to the Office of Graduate Studies of
Texas A&M University
in partial fulfillment of the requirements for the degree of

DOCTOR OF PHILOSOPHY

May 2010

Major Subject: Petroleum Engineering

NUMERICAL MODELING OF FRACTURE PERMEABILITY CHANGE IN NATURALLY FRACTURED RESERVOIRS USING A FULLY COUPLED DISPLACEMENT DISCONTINUITY METHOD

A Dissertation

by

QINGFENG TAO

Submitted to the Office of Graduate Studies of
Texas A&M University
in partial fulfillment of the requirements for the degree of

DOCTOR OF PHILOSOPHY

Approved by:

Co-Chairs of Committee,	Christine A. Ehlig-Economides
	Ahmad Ghassemi
Committee Members,	A. Daniel Hill
	Ding Zhu
	Yalchin Efendiev
Head of Department,	Stephen A. Holditch

May 2010

Major Subject: Petroleum Engineering

ABSTRACT

Numerical Modeling of Fracture Permeability Change in Naturally Fractured Reservoirs Using a Fully Coupled Displacement Discontinuity Method. (May 2010)

Qingfeng Tao, B.S., China University of Geosciences;

M.S., University of North Dakota

Co-Chairs of Advisory Committee: Dr. Christine A. Ehlig-Economides
Dr. Ahmad Ghassemi

Fractures are the main flow channels in naturally fractured reservoirs. Therefore the fracture permeability is a critical parameter to production optimization and reservoir management. Fluid pressure reduction caused by production induces an increase in effective stress in naturally fractured reservoirs. The change of effective stress induces fracture deformation and changes fracture aperture and permeability, which in turn influences the production. Coupled interactions exist in the fractured reservoir: (i) fluid pressure change induces matrix deformation and stress change; (ii) matrix deformation induces fluid volume change and fluid pressure change; (iii) fracture deformation induces the change of pore pressure and stress in the whole field (the influence disappears at infinity); (iv) the change of pore pressure and stress at any point has an influence on the fracture and induces fracture deformation. To model accurately the influence of pressure reduction on the fracture permeability change in naturally fractured reservoirs, all of these coupled processes need to be considered. Therefore, in this dissertation a fully coupled approach is developed to model the influence of production

on fracture aperture and permeability by combining a finite difference method to solve the fluid flow in fractures, a fully coupled displacement discontinuity method to build the global relation of fracture deformation, and the Barton-Bandis model of fracture deformation to build the local relation of fracture deformation.

The fully coupled approach is applied to simulate the fracture permeability change in naturally fracture reservoir under isotropic in situ stress conditions and high anisotropic in situ stress conditions, respectively. Under isotropic stress conditions, the fracture aperture and permeability decrease with pressure reduction caused by production, and the magnitude of the decrease is dependent on the initial effective in situ stress. Under highly anisotropic stress, the fracture permeability can be enhanced by production because of shear dilation. The enhancement of fracture permeability will benefit to the production of oil and gas.

ACKNOWLEDGEMENTS

I would like to thank one of my co-advisors, Dr. Ehlig-Economides, for her support and guidance. She provided me the opportunity to study the naturally fractured reservoirs and supported me to choose the topic of the dissertation which I am very interested in. I will forever be indebted to my other co-advisor, Dr. Ghassemi, who led me into the field of geomechanics. The idea of using the displacement discontinuity method in this study is from the discussions with Dr. Ghassemi two years ago. He provided me lots of help during the past six years and is always available whenever I need help in my study and work. I would like also to thank the other committee members, Dr. Hill, Dr. Zhu and Dr. Efendiev, for their help. The discussions on this topic with Dr. Zeng of University of North Dakota and Dr. Wu of Colorado School of Mines are greatly appreciated. I am grateful to my parents for their continuous support and to my wife for her understanding and love. Finally I would like to thank all professors I took classes from and all my friends.

TABLE OF CONTENTS

Page

Page

Page

LIST OF FIGURES

Page

Page

Page

Page

Page

LIST OF TABLES

Page

CHAPTER I

INTRODUCTION

A large percent of oil and gas around the world are produced from naturally fractured reservoirs. Naturally fractured reservoirs are found in essentially all types of lithologies including sand stones, carbonates, shales, cherts, siltstones, etc. (Aguilera, 1995). A natural fracture is "a naturally occurring macroscopic planar discontinuity in rock due to deformation or physical diagenesis" (Nelson, 1985). Generally fractures are the main flow channels, and the matrix provides the main storage capacity. Some reservoirs, e.g. tight gas reservoirs, are not possible to produce without the existence of natural fractures (microfractures). Therefore the fracture permeability is critical to the hydrocarbon production. This chapter will start with an explanation of the problem and the objective of this research. Next will be a review of the previous numerical methods on the modeling of deformable fractured reservoirs. Finally there will appear a summary of the dissertation.

This dissertation follows the style of *SPE Reservoir Evaluation and Engineering*.

1.1 Problem and objective

Warren and Root (1963) presented a dual-porosity model to represent naturally fractured reservoirs (Figure I-1). The highly heterogeneous system was treated as a homogeneous system with two media – fractures and matrix. Both the matrix and the fractures were characterized by two parameters – porosity and permeability. Pseudosteady state flow was assumed in the matrix, as well as an interporosity flow parameter for flow between matrix and fractures. Later a dual-porosity model with transient flow in matrix for low permeability reservoirs was presented by De Swaan (1976), Najurieta(1980), Cinco and Samaniego(1982). Both fracture permeability and matrix permeability were treated as constant during production and independent of stress and pressure. In all of these cases, flow to the well was only via fractures.

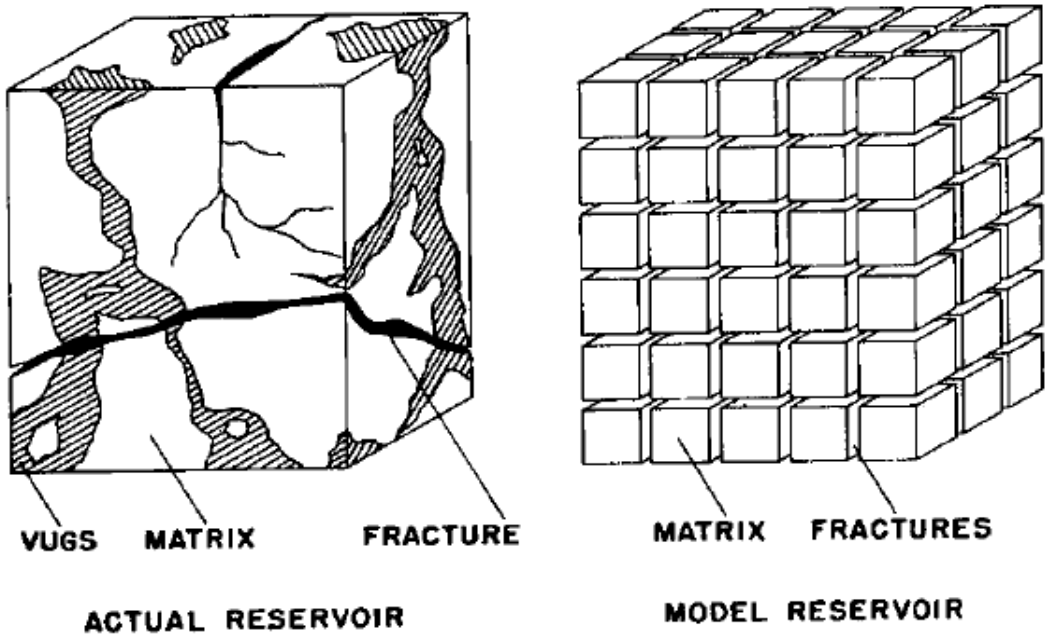

Figure I-1. Dual-porosity model (Warren and Root, 1963).

In reality, reservoir pressure decreases with production for most cases, and the effective stress in the reservoir increases, and both fractures and matrix can deform with the increase of effective stress. For hard rocks, the deformation due to normal stress change is small and can be neglected. However, the deformation for weak rocks or fractured rocks can be large enough to change the reservoir properties and influence the production. The dependence of formation permeability on pressure for a single porosity system has been investigated by Gray et al. (1963), Vairogs et al. (1971), Thomas and Ward (1972), Raghavan et al. (1972), Vairogs and Rhoades (1973), Samaniego et al. (1976, 1977), Jones and Owens (1980), Samaniego and Cinco-Ley (1989), Buchsteiner et al. (1993), Chin et al. (1998), and Davies and Davies (1999). The pressure dependence of matrix permeability occurs as the porosity and connectivity of pores decrease with increase in effective stress. But the permeability change in tight gas reservoirs mainly results from the closure of microcracks with the increase of effective stress (Ostensen, 1986).

Generally fractures are more deformable than the matrix in a naturally fractured reservoir, and the permeability of fractures, not the matrix, dominates the flow behavior. Furthermore, fractures are more sensitive to pressure and stress change than the matrix, and the fracture deformation mechanism is much more complicated than matrix deformation. The effect of stress on the aperture and permeability of a single fracture has been well investigated in laboratory by Iwai (1976), Goodman (1976), Bandis et al. (1983), and Barton et al. (1985). Experimental data show a nonlinear relation between

normal stress and fracture closure. Bandis et al. (1983) presented a hyperbolic formula to represent the normal stress–fracture closure relation. For shear deformation experimental data show an approximately linear relation between shear stress and shear displacement before yielding, and then shows a complicated relation after yielding. Shear deformation can also induce fracture opening as the opposed asperities of a fracture slide over each other and cause an increase in aperture. Chapter III will elaborate on these mechanisms.

In naturally fractured reservoirs, there are coupled interactions between porous matrix and fluid, as well as between fractures. Biot (1941, 1956) developed a theory of poroelasticity for porous media saturated with incompressible fluid to account for the coupled diffusion–deformation mechanism. Rice and Cleary (1976) extended the theory for porous media saturated with compressible fluid. Biot's theory of poroelasticity is a continuum theory for a porous medium consisting of an elastic matrix containing interconnected fluid-saturated pores. The fluid diffusion in porous media induces porous matrix deformation (Figure I-2) and stress redistribution, and porous matrix deformation also induces fluid flow (Figure I-3) and fluid pressure redistribution. If there is a discontinuous surface (fracture) in the continuum porous media shown in Figure I-4, the deformation of the fracture (opening or closing) will induce the deformation of the porous matrix and also pore pressure change and fluid flow, which will be elaborated in Chapter II.

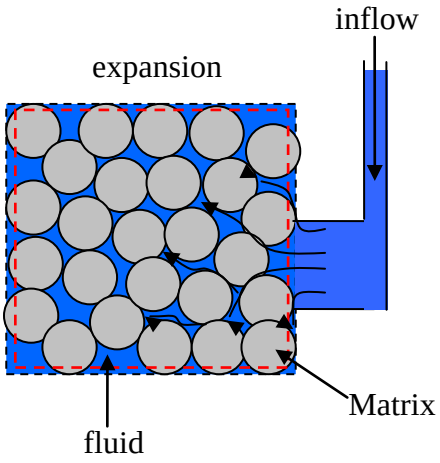

Figure I-2. Illustration of the fluid flow in the interconnected pores in a porous matrix and the induced deformation of the porous matrix (influence of fluid flow on the matrix deformation). The dashed red line represents the boundary of the porous matrix before fluid injection/production.

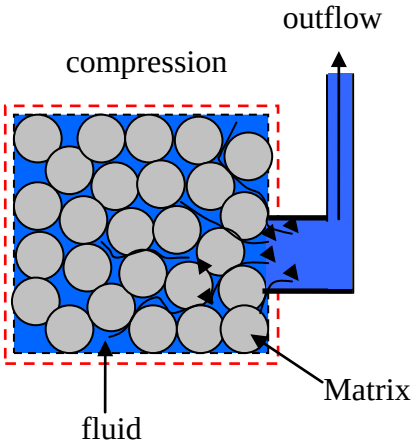

Figure I-3. Illustration of the compression of a continuum porous matrix and the induced pore pressure change and fluid flow in the interconnected pores (influence of matrix deformation on the fluid flow and pore pressure change). The dashed red line represents the boundary of the porous matrix before deformation.

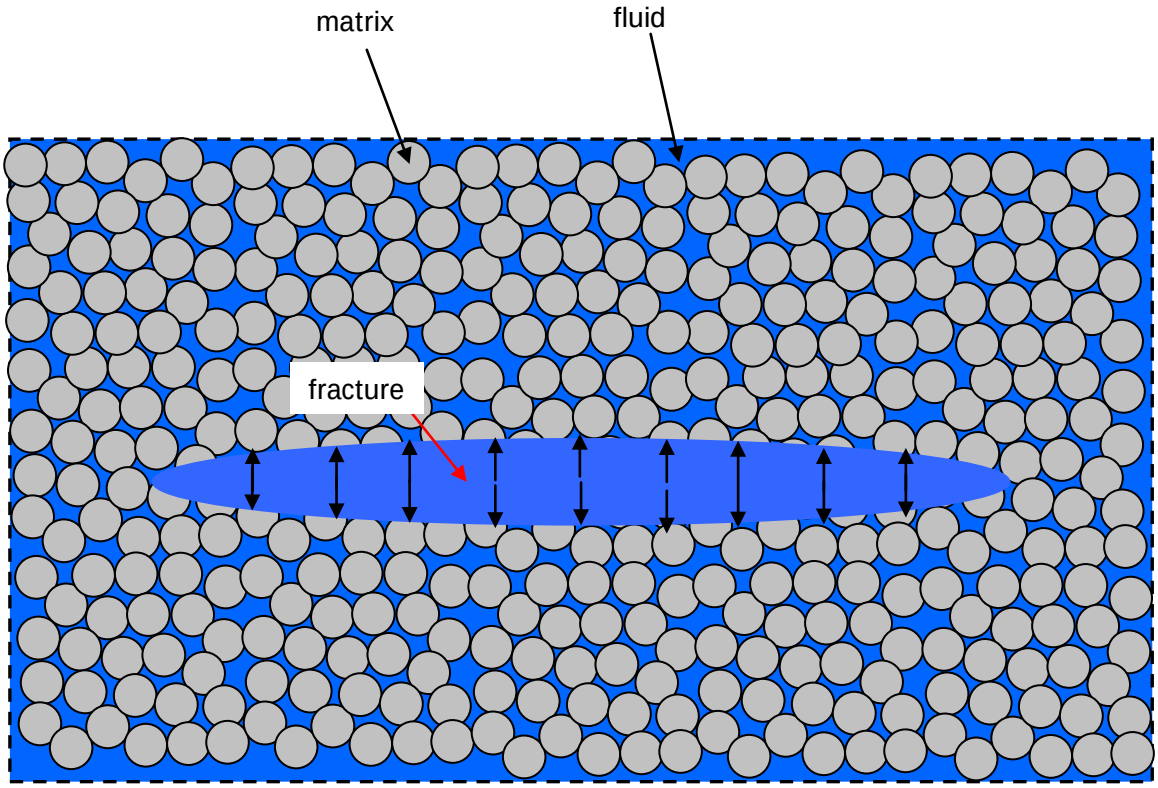

Figure I-4. Illustration of a fracture in a fluid-saturated porous media.

In a naturally fractured reservoir, there are many fractures in the porous medium. In addition to the interactions of fluid, porous matrix and fracture, there are interactions between fractures including mechanical deformation and fluid flow, which will be elaborated in Chapter II. One fracture deformation will cause stress change in the field and induce deformation of other fractures (Crouch and Starfield, 1983, Curren and Carvalho, 1987, Cheng and Predeleanu, 1987, Carvalho, 1990). The fluid injection or production from one fracture can also induce fluid pressure change in other fractures, as well as mechanical deformation. Crouch and Starfield (1983) developed a displacement discontinuity method (DDM) to model the interactions between fractures and also the

influence of fracture deformation on the stress redistribution in elastic nonporous media. Curren and Carvalho (1987), Cheng and Predeleanu (1987) and Carvalho (1990) developed a poroelastic DDM for fluid-saturated porous media with many discontinuous surfaces (fractures) in it. The poroelastic DDM can be applied to model the coupled interactions of fractures, porous matrix and fluid in porous media with fractures. This method has been applied to simulate the hydraulic fracturing in continuum porous media (Vandamme and Roegiers, 1990). But the poroelastic DDM has not been applied to model the interactions of fracture, porous matrix and fluid in fractured porous media.

The oil and gas production from naturally fractured reservoirs will induce the change in fracture aperture and permeability, thereby changing reservoir properties and influencing production. The objective of this study is to develop an approach to investigate the change in fracture aperture and permeability in naturally fractured reservoirs. This approach will consider the coupled interactions of porous matrix, fluid and fractures and the real mechanism of fracture deformation.

1.2 Numerical methods for deformable fractured reservoirs

Many researchers have investigated the deformation of fractures in fluid-saturated fractured porous media using numerical methods (Asgian, 1988, 1989; Sun, 1994; Chen and Teufel, 1997; Gutierrez and Makurat, 1997; Lewis and Ghasouri, 1997; Meng, 1998; Shu, 1999; Min et al., 2004; and Bagheri, 2006). The numerical methods can be classified as continuum methods, the discrete element method, and the displacement discontinuity method. The continuum methods treat the fractured media as

an equivalent continuum media for fluid flow model, or mechanical deformation, or both. The stress and pore pressure in the equivalent continuum media are solved by using a finite difference method (FDM) or a finite element method (FEM). The discrete element method (DEM) treats matrix elements divided by fractures as discrete, and calculates the contact and deformation of the matrix element boundaries. The displacement discontinuity method (DDM) is an indirect boundary element method. The DDM gives an analytical solution for the influence of a fracture in a continuum media and then sums the influences of all fractures for a fractured media by the superposition method (refer to Chapter II for details).

1.2.1 Continuum methods

Lewis and Ghafouri (1997) developed a finite element dual porosity model. They modeled fluid flow using a dual porosity model – the fracture and matrix were treated as overlapping continuum media (Figure I-5). Flow properties (fracture permeability, matrix permeability, etc.) were assumed to be independent of pore pressure and stress. The fluid pressure change was uncoupled with the mechanical deformation of the fractured media. The fractured media were treated as continuum elastic media. Fluid pressure change caused by production was solved separately from porous matrix deformation. The effective stress change resulting from pore pressure change was derived using Terzaghi's effective stress law (effective stress = total stress – fluid pressure). Finally the deformation of fractured media was modeled according to the effective stress change.

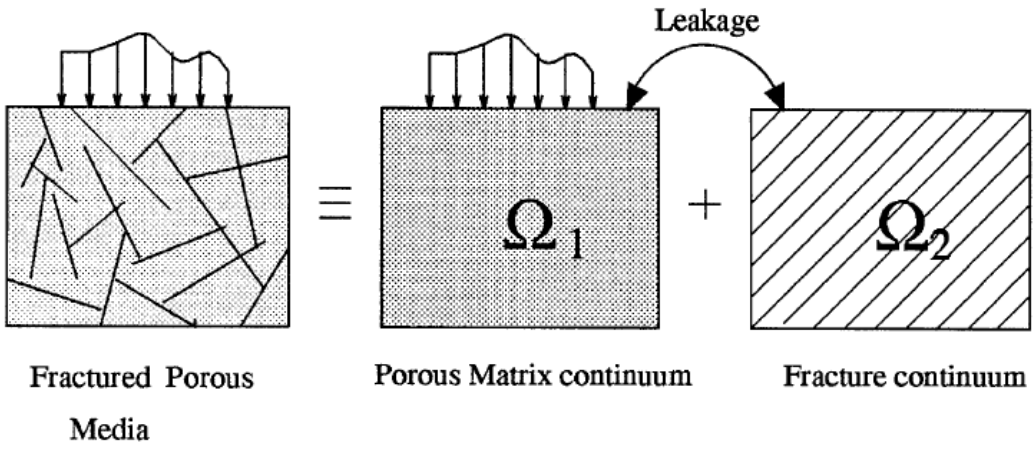

Figure I-5. Schematic representation of double porosity model (Lewis and Ghafouri, 1997).

Chen and Teufel (1997) presented a partially coupled method for deformable fractured media. For fluid flow, the fractured media was assumed as a dual porosity model – fracture and matrix are two overlapping continuum media. For geomechanics, the fractured media was assumed as continuum poroelastic media and the coupling between porous matrix and fluid was based on Biot's theory of poroelasticity. The fracture and matrix were virtually combined into one media with one combined porosity and compressibility in the mechanical model. Therefore the fracture deformation was oversimplified as matrix deformation. The fracture aperture and permeability was independent of pressure and stress. Meng (1998) and Shu (1999) used similar models to model the coupled processes considering two fluid phases.

Sun (1994) used a discrete fracture element approach to model the deformable fractured porous media. Fluid flow was modeled in both the porous medium and a discrete fracture network. The transient flow rate between fracture network and porous media was determined by the pressure gradient. For the mechanical model, each

fracture was treated as equivalent elastic medium having the same stress-displacement relation as the fracture deformation. The shear displacement and dilation of fracture was neglected, and only normal deformation was considered. The coupling of fluid flow and mechanical deformation was based on Biot's theory of poroelasticity. The stress dependent fracture permeability was calculated according to the fracture aperture, which was idealized as a smooth fracture approximating the real rough fracture (Figure I-6).

Bagheri (2006), and Bagheri and Setteri (2008) developed an equivalent continuum media for fractured porous media considering both fluid flow and a mechanical model. For the fluid flow model, an element of fractured porous media was transformed to an element of equivalent continuum media with a tensor permeability to make the continuum media element have similar flow properties to the fractured medium element. For the deformation model, the fractured medium was transformed to an equivalent continuum poroelastic medium with the same deformation characteristics as the fractured medium. Only normal deformation of fractures was considered. And only small fracture deformation was allowed in the model. The fracture permeability and porosity was dependent on pressure and stress.

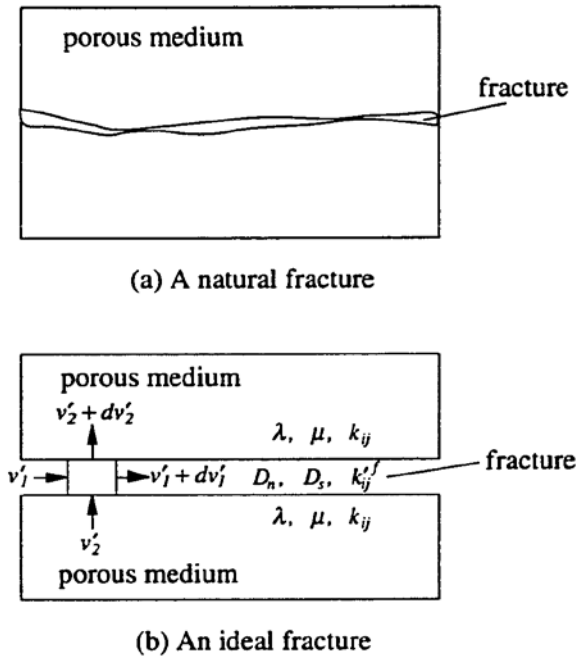

Figure I-6. A real rough fracture in porous media and its idealized smooth fracture in two dimensions (Sun, 1994).

1.2.2 Discrete element method (DEM)

Gutierrez and Makurat (1997) combined a thermal reservoir fluid flow simulator code PROFHET (Propagation of fluid and heat) and a discrete element code UDEC (Universal distinct element code) to analyze the hydro-thermo-mechanical behavior of fractured hydrocarbon reservoirs. Fluid flow was modeled in both the discrete fracture network and the porous matrix, and the interface flow rate was determined by pressure gradient between fracture and matrix. The stress change induced by fluid flow was input into UDEC to calculate the fracture deformation. The Barton-Bandis model of fracture deformation was applied. The results from UDEC were not used to recalculate the fluid

flow. The matrix in UDEC was defined as impermeable, which reduced the coupling of porous matrix and fluid described by Biot's theory of poroelasticity.

Min et al. (2004) used UDEC to model the effect of stress on fracture permeability for a fractured media (Figure I-7). The matrix was assumed as impermeable and the fluid flow was only in the fracture network. The fracture aperture changed with different stress loading according to the fracture deformation model. They modeled the fracture aperture changes at various stress conditions including isotropic stress loadings of different magnitudes and anisotropic loadings of different magnitudes and ratios of the maximum principal stress to the minimum principal stress. Then they modeled the flow rate through the fracture network with a fluid pressure loading. After comparing with the Darcy's flaw, the permeability for the fracture network was determined and the effect of stress on the permeability of fracture network was evaluated.

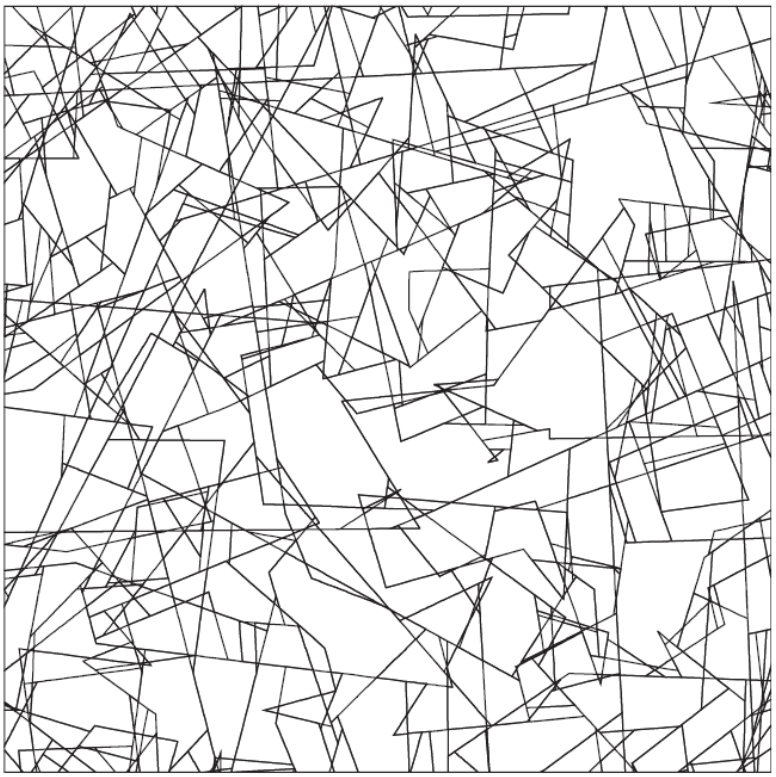

Figure I-7. Geometry of fracture system in the DFN model (Min et al., 2004).

1.2.3 Displacement discontinuity method (DDM)

Asgian (1988, 1989) investigated the coupled fluid and porous matrix deformation in fractured media using an elastic DDM. The elastic DDM (an indirect boundary element method) was developed (Crouch and Starfield, 1983) to model the deformation of elastic nonporous media containing discontinuous surfaces (fractures). The matrix was assumed as impermeable and fluid flow was only in fractures. The fluid flow in fractures was coupled with the fracture deformation. The fracture permeability was also dependent on the fracture aperture according to the cubic law and the fracture

aperture varied with the change of fluid pressure and effective stress. This method allowed the fracture to deform in normal and shear with a large displacement. But the matrix was assumed as impermeable in the elastic DDM, which limits its application in fractured hydrocarbon reservoirs where the matrix is the main storage.

1.3 Summary of the dissertation

Chapter I describes the problem to be solved and the objective of the study, and also critically reviews previously published methods. Pressure reduction caused by production in naturally fractured reservoirs induces the effective stress change. The effective stress change affects the reservoir properties, which in turn influences the production. Up to now the effect of production on reservoir properties including fully coupled interactions of porous matrix, fluid and fractures in naturally fractured reservoirs, especially fracture permeability change, has not really been addressed. The objective of this study is to develop an approach to investigate the change in fracture aperture and permeability in naturally fractured reservoirs.

Chapter II describes the DDM including elastic DDM and fully coupled poroelastic DDM. The elastic DDM gives the analytical solutions of induced stress and displacement at any point in a continuum elastic nonporous medium by a small thin discontinuous surface (fracture) with finite length and then sums the influences of all discontinuous surfaces (fractures) at any point using superposition. The fully coupled DDM is based on Biot's theory of poroelasticity. The fundamental solutions for stress and pore pressure at any point induced either by a small discontinuous surface (fracture)

with finite length or by constant rate fluid injection/production to a line source (fracture at a well) are derived analytically. At any point, the influences by all fractures due to displacement discontinuities or fluid injection/production can be obtained by the superposition method. The fully coupled poroelastic DDM is verified using the classic pressurized crack problem. Provided the stress and pore pressure change in the fractures in a fractured porous media, the fracture aperture change can be determined using the fully coupled poroelastic DDM.

Chapter III describes the characteristics of fracture surfaces, the nonlinear Barton-Bandis model of fracture deformation, and the relation of fracture permeability to fracture aperture in rough fractures. In the nonlinear fracture deformation model, the relation of normal stress and fracture closure is represented by a hyperbolic formula. The relation of shear stress and shear displacement is linear before yielding and too complicated to represent using simple functions after yielding. The model also includes shear dilation which is the fracture opening caused by shear displacement. The fracture conductivity has a cubic relation to the effective hydraulic aperture but not the average mechanical aperture. The effective hydraulic aperture is related with the average mechanical aperture using the parameter for the surface roughness of fracture.

Chapter IV presents a new numerical method to determine the fluid pressure, fracture aperture change and stress change simultaneously by combining a finite difference method (FDM) for solving the diffusivity equation for fluid flow in fractures, a fully coupled displacement discontinuity method (DDM) to build the global relation of fracture deformation, and the nonlinear Barton-Bandis model of fracture deformation to

build the local relation of fracture deformation. The fracture permeability changes with the fracture aperture change.

Chapter V illustrates applications of the method described in Chapter IV under both isotropic in situ stress conditions and highly anisotropic in situ stress conditions. The increase of the compression stress induced by pressure depletion in naturally fracture reservoirs tends to reduce fracture aperture and permeability, but fracture slip caused by shear stress can increase fracture aperture and permeability due to shear dilation.

Chapter VI gives conclusions of the dissertation and recommendations for future work.

CHAPTER II

DISPLACEMENT DISCONTINUITY METHOD

The displacement discontinuity method (DDM) is an indirect boundary element method of solving linear elastic problems given the boundary conditions and assuming continuous stress and discontinuous displacement at the boundaries. Crouch and Starfield (1983) developed an elastic DDM for elastic nonporous media and applied the elastic DDM to model the joint deformation and slip due to mining jointed rock. In the fluid-saturated porous media, there are coupled processes between the porous matrix and fluid. Both porous matrix deformation and fluid pressure change can cause redistribution of stress and fluid flux. Curran and Carvalho (1987), Cheng and Predeleanu (1987), and Carvalho (1990) presented a coupled DDM for fluid-saturated porous media and provided the fundamental solutions of stress, displacement and pore pressure induced by constant displacement discontinuities or continuous fluid injection/production along a line fracture in an infinite continuum porous medium saturated with a compressible singe-phase fluid. The induced stress and pore pressure by the displacement discontinuities or fluid injection/production from all fractures in a porous medium are the sum of the fundamental solutions using superposition. All fractures in an infinite fluid-saturated porous medium are treated as boundaries. If the change of stress and pore pressure in all fractures in the fluid-saturated system are provided as boundary conditions, the displacement discontinuities and fluid injection/production rate in all fractures can be determined by solving a set of linear

equations established from the fully coupled DDM, and vice versa. Therefore, the fully coupled DDM can be applied to investigate the change of fracture aperture and the interface flow rate between fracture and matrix (similar to the fluid injection/production rate from a fracture into the surrounded matrix) if the stress and pore pressure in all fractures in fractured porous media is provided. A pressurized crack problem is provided as a case to verify the fully coupled DDM and show the coupled interactions between the fluid and porous matrix.

This chapter will describe the elastic DDM in Section 2.1. Section 2.2 will provide the fully coupled poroelastic DDM. Section 2.3 will verify the fully coupled poroelastic DDM with an analytical solution, and Section 2.4 will provide conclusions of this chapter.

2.1 Elastic DDM

The elastic DDM is an indirect boundary element method to cope those problems involving pure elastic nonporous media containing thin fractures. The elastic DDM is based on an analytical solution for the constant discontinuity of a displacement (e.g., a finite fracture segment) in an infinite elastic nonporous medium. For an infinite elastic nonporous medium containing multiple fractures, the fractures are divided into N elemental segments with the displacement in each segment assumed to have a constant discontinuity. At any point, the influence of displacement discontinuities from all fractures in the system can be obtained by summing the effects of all N elements using the fundamental analytical solutions.

Crouch and Starfield (1983) developed the fundamental solutions (Eq. (2-1)) of induced stresses at any point (x, y) for an infinite two-dimensional homogeneous and isotropic elastic nonporous medium containing a finite small thin fracture with constant normal and shear displacement discontinuities (Figure II-1). The fracture length is $2a$ (a is the half length of fracture segment) and its center is located at (0, 0).

The stress components, σ_{xx}, σ_{yy}, σ_{xy} at the field point (x, y) induced by the normal displacement discontinuity, D_n ,and Shear displacement discontinuity, D_s, are given by

$$\sigma_{xx} = 2GD_n\left(\frac{\partial^2 f}{\partial y^2} + y\frac{\partial^3 f}{\partial y^3}\right) + 2GD_s\left(2\frac{\partial^2 f}{\partial x\partial y} + y\frac{\partial^3 f}{\partial x\partial y^2}\right)$$

$$\sigma_{yy} = 2GD_n\left(\frac{\partial^2 f}{\partial y^2} - y\frac{\partial^3 f}{\partial y^3}\right) - 2GD_s y\frac{\partial^3 f}{\partial x\partial y^2} \qquad (2\text{-}1)$$

$$\sigma_{xy} = -2GD_n y\frac{\partial^3 f}{\partial x\partial y^2} + 2GD_s\left(\frac{\partial^2 f}{\partial y^2} + y\frac{\partial^3 f}{\partial y^3}\right)$$

where G is the shear modulus, and f is a function of the position (x, y) of the field point relative to the center of the fracture and the half length of the fracture segment a given by:

$$f(x,y) = -\frac{1}{4\pi(1-\upsilon)}\left[y\left(\arctan\frac{y}{x-a} - \arctan\frac{y}{x+a}\right) - (x-a)\ln\sqrt{(x-a)^2+y^2} + (x+a)\ln\sqrt{(x+a)^2+y^2}\right], \qquad (2\text{-}2)$$

with Poisson's ratio, υ. *Note that in this dissertation SI units are used in all equations except for the specified equations, but oilfield units are shown in the results.*

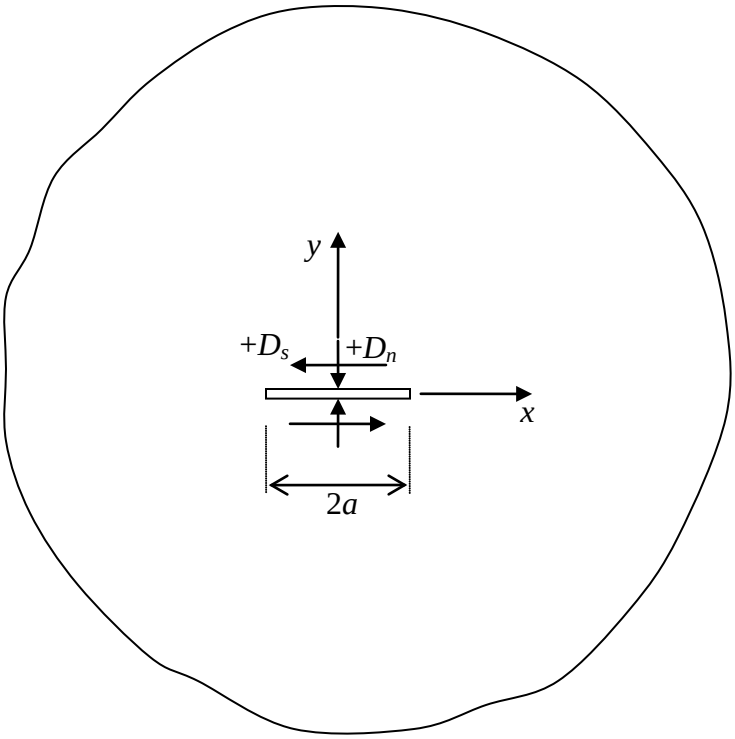

Figure II-1. A small discontinuous segment in an infinite two-dimensional nonporous medium (after Crouch and Starfield, 1983).

Following is an illustration of the elastic DDM method:

The curvy fracture in a two-dimensional infinite nonporous medium shown in Figure II-2 is discretized into 5 segments and the influence of displacement discontinuities on an arbitrary field point (x, y) from the curvy fracture can be approximated by summing the influences from the 5 fracture segments on the point (x, y).

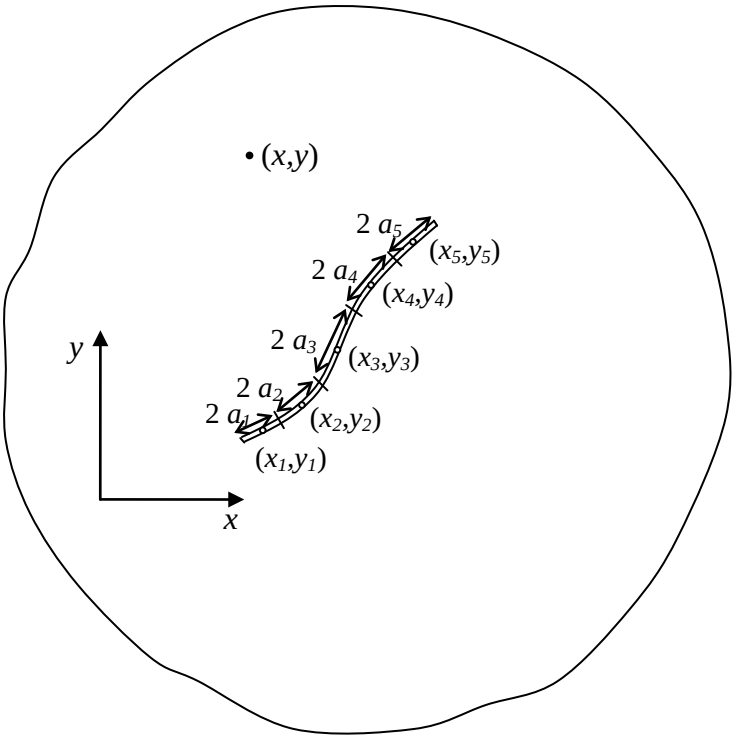

Figure II-2. A curvy fracture discretized into 5 segments in an infinite two-dimensional nonporous medium.

The fundamental solutions (Eq. (2-1)) are for a fracture segment parallel to the x-axis and the center of the fracture segment located at (0, 0). To apply the fundamental solutions, the field point (*x*, *y*) shown in Figure II-2 must be transformed into a local co-ordinate system for the *jth* fracture segment with an angle β_j with *x*-axis, as in Figure II-3. The $\bar{x}$-axis of the local co-ordinate system is parallel to the orientation of the *jth* fracture segment. The field point (*x*, *y*) is transformed to the local $\bar{x}$, $\bar{y}$ co-ordinate.

$$\bar{x} = (x - x_j)\cos\beta_j + (y - y_j)\sin\beta_j$$
$$\bar{y} = -(x - x_j)\sin\beta_j + (y - y_j)\cos\beta_j \qquad (2\text{-}3)$$

where (x_j, y_j) is the midpoint of the *jth* fracture segment. The induced stresses on the field point in the local $\bar{x}$, $\bar{y}$ co-ordinate system by the normal and shear displacement discontinuities of the *jth* fracture are:

$$\begin{aligned}
\overset{j}{\sigma}_{\bar{x}\bar{x}} &= 2G\,\overset{j}{D}_n\left(\frac{\partial^2 \bar{f}}{\partial \bar{y}^2}+\bar{y}\frac{\partial^3 \bar{f}}{\partial \bar{y}^3}\right)+2G\,\overset{j}{D}_s\left(2\frac{\partial^2 \bar{f}}{\partial \bar{x}\partial \bar{y}}+\bar{y}\frac{\partial^3 \bar{f}}{\partial \bar{x}\partial \bar{y}^2}\right)\\
\overset{j}{\sigma}_{\bar{y}\bar{y}} &= 2G\,\overset{j}{D}_n\left(\frac{\partial^2 \bar{f}}{\partial \bar{y}^2}-\bar{y}\frac{\partial^3 \bar{f}}{\partial \bar{y}^3}\right)-2G\,\overset{j}{D}_s\,\bar{y}\frac{\partial^3 \bar{f}}{\partial \bar{x}\partial \bar{y}^2}\\
\overset{j}{\sigma}_{\bar{x}\bar{y}} &= -2G\,\overset{j}{D}_n\,\bar{y}\frac{\partial^3 \bar{f}}{\partial \bar{x}\partial \bar{y}^2}+2G\,\overset{j}{D}_s\left(\frac{\partial^2 \bar{f}}{\partial \bar{y}^2}+\bar{y}\frac{\partial^3 \bar{f}}{\partial \bar{y}^3}\right)
\end{aligned} \tag{2-4}$$

where

$$\begin{aligned}
\bar{f}(\bar{x},\bar{y}) = -\frac{1}{4\pi(1-\upsilon)}\Bigg[&\bar{y}\left(\arctan\frac{\bar{y}}{\bar{x}-a_j}-\arctan\frac{\bar{y}}{\bar{x}+a_j}\right)\\
&-(\bar{x}-a_j)\ln\sqrt{(\bar{x}-a_j)^2+\bar{y}^2}+(\bar{x}+a_j)\ln\sqrt{(\bar{x}+a_j)^2+\bar{y}^2}\Bigg]
\end{aligned} \tag{2-5}$$

The induced stresses on the field point (*x*, *y*) in the *x*, *y* co-ordinate system by the jth fracture segment are obtained by transforming the Eq. (2-4) from the local $\bar{x}$, $\bar{y}$ co-ordinate system to the *x*, *y* co-ordinate system using the transformation formula (Crouch and Starfield, 1983).

$$\begin{aligned}
\overset{j}{\sigma}_{xx} &= \overset{j}{\sigma}_{\bar{x}\bar{x}}\cos^2\beta_j-\overset{j}{\sigma}_{\bar{x}\bar{y}}\sin 2\beta_j+\overset{j}{\sigma}_{\bar{y}\bar{y}}\sin^2\beta_j\\
\overset{j}{\sigma}_{yy} &= \overset{j}{\sigma}_{\bar{x}\bar{x}}\sin^2\beta_j+\overset{j}{\sigma}_{\bar{x}\bar{y}}\sin 2\beta_j+\overset{j}{\sigma}_{\bar{y}\bar{y}}\cos^2\beta_j\\
\overset{j}{\sigma}_{xy} &= \left(\overset{j}{\sigma}_{\bar{x}\bar{x}}-\overset{j}{\sigma}_{\bar{y}\bar{y}}\right)\sin\beta_j\cos\beta_j+\overset{j}{\sigma}_{\bar{x}\bar{y}}\left(\cos^2\beta_j-\sin^2\beta_j\right)
\end{aligned} \tag{2-6}$$

The induced stresses on an arbitrary point (*x, y*) by the displacement discontinuities of the curvy fracture are approximated by superposition as the sum of the influences from all 5 fracture segments.

$$\sigma_{xx} = \sum_{j=1}^{5} {}^{j}\sigma_{xx}$$

$$\sigma_{yy} = \sum_{j=1}^{5} {}^{j}\sigma_{yy} \qquad \text{(2-7)}$$

$$\sigma_{xy} = \sum_{j=1}^{5} {}^{j}\sigma_{xy}$$

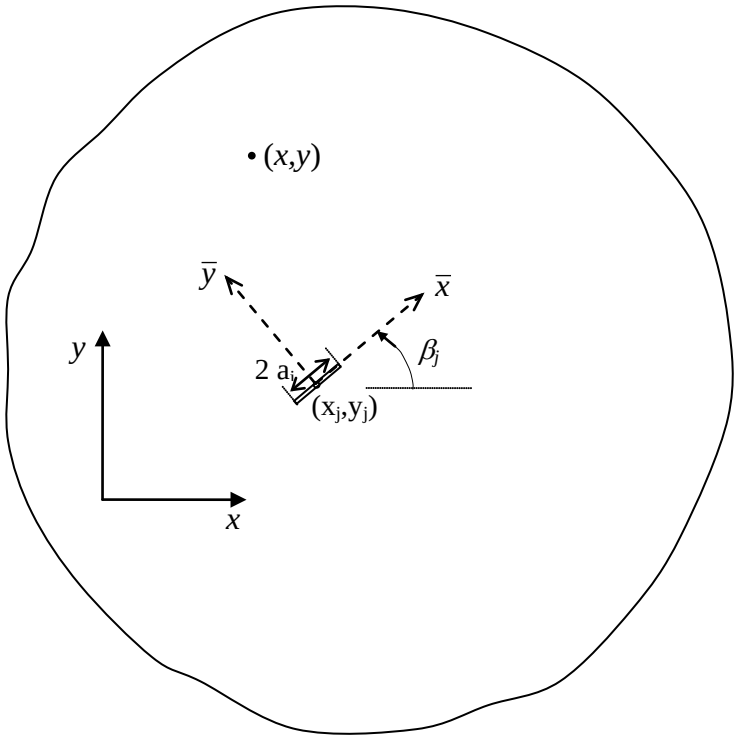

Figure II-3. Local co-ordinate for the *jth* fracture segment in an elastic nonporous medium.

If the field point (x, y) coincides with the midpoint (x_i, y_i) of the *ith* fracture segment, the Eq. (2-4) are the induced stresses on the *ith* fracture segment by the normal and shear displacement discontinuities of the *jth* fracture segment in the local $\bar{x}$, $\bar{y}$ co-ordinate system (Figure II-4). The induced stresses on the *ith* fracture segment by the *jth* fracture segment can be transformed into normal and shear stresses to the *ith* fracture segment using the following formula.

$$\begin{aligned}
\overset{ij}{\sigma}_n &= \overset{j}{\sigma}_{\bar{x}\bar{x}} \cos^2 \overset{ij}{\gamma} + \overset{j}{\sigma}_{\bar{x}\bar{y}} \sin 2\gamma' + \overset{j}{\sigma}_{\bar{y}\bar{y}} \sin^2 \overset{ij}{\gamma} \\
\overset{ij}{\sigma}_s &= \left(\overset{j}{\sigma}_{\bar{x}\bar{x}} - \overset{j}{\sigma}_{\bar{y}\bar{y}} \right) \sin \overset{ij}{\gamma} \cos \overset{ij}{\gamma} - \overset{j}{\sigma}_{\bar{x}\bar{y}} \left(\cos^2 \overset{ij}{\gamma} - \sin^2 \overset{ij}{\gamma} \right)
\end{aligned} \tag{2-8}$$

where $\overset{ij}{\gamma} = \frac{\pi}{2} + \beta_i - \beta_j$, and $\overset{ij}{\sigma}_n$, $\overset{ij}{\sigma}_s$ are the induced normal and shear stresses on the *ith* fracture segment by the *jth* fracture segment. Combining Eqs. (2-4) and (2-8) yields:

$$\begin{aligned}
\overset{ij}{\sigma}_n &= \overset{ij}{A}\, \overset{j}{D}_n + \overset{ij}{B}\, \overset{j}{D}_s \\
\overset{ij}{\sigma}_s &= \overset{ij}{E}\, \overset{j}{D}_n + \overset{ij}{F}\, \overset{j}{D}_s
\end{aligned} \tag{2-9}$$

where

$$\begin{aligned}
\overset{ij}{A} &= 2G \left[\frac{\partial^2 \bar{f}}{\partial \bar{y}^2} + \left(\cos^2 \overset{ij}{\gamma} - \sin^2 \overset{ij}{\gamma} \right) \bar{y} \frac{\partial^3 \bar{f}}{\partial \bar{y}^3} - \sin 2\overset{ij}{\gamma}\, \bar{y} \frac{\partial^3 \bar{f}}{\partial \bar{x} \partial \bar{y}^2} \right] \\
\overset{ij}{B} &= 2G \left[\cos^2 \overset{ij}{\gamma} \left(2 \frac{\partial^2 \bar{f}}{\partial \bar{x} \partial \bar{y}} + \bar{y} \frac{\partial^3 \bar{f}}{\partial \bar{x} \partial \bar{y}^2} \right) - \sin^2 \overset{ij}{\gamma}\, \bar{y} \frac{\partial^3 \bar{f}}{\partial \bar{x} \partial \bar{y}^2} + \sin 2\overset{ij}{\gamma} \left(\frac{\partial^2 \bar{f}}{\partial \bar{y}^2} + \bar{y} \frac{\partial^3 \bar{f}}{\partial \bar{y}^3} \right) \right] \\
\overset{ij}{E} &= 2G\bar{y} \left[\sin 2\overset{ij}{\gamma} \frac{\partial^3 \bar{f}}{\partial \bar{y}^3} + \left(\cos^2 \overset{ij}{\gamma} - \sin^2 \overset{ij}{\gamma} \right) \frac{\partial^3 \bar{f}}{\partial \bar{x} \partial \bar{y}^2} \right]
\end{aligned} \tag{2-10}$$

$$\overset{ij}{F} = 2G\left[\sin 2\overset{ij}{\gamma}\left(\frac{\partial^2 \bar{f}}{\partial \bar{x}\partial \bar{y}} + \bar{y}\frac{\partial^3 \bar{f}}{\partial \bar{x}\partial \bar{y}^2}\right) - \left(\cos^2 \overset{ij}{\gamma} - \sin^2 \overset{ij}{\gamma}\right)\left(\frac{\partial^2 \bar{f}}{\partial \bar{y}^2} + \bar{y}\frac{\partial^3 \bar{f}}{\partial \bar{y}^3}\right)\right]$$

The induced normal and shear stresses on the *ith* fracture segment by the normal and shear displacement discontinuities of all fracture segments are obtained by summing the solutions in Eq. (2-9).

$$\begin{aligned} \overset{i}{\sigma}_n &= \sum_{j=1}^{5} \overset{ij}{A}\,\overset{j}{D}_n + \sum_{j=1}^{5} \overset{ij}{B}\,\overset{j}{D}_s \\ \overset{i}{\sigma}_s &= \sum_{j=1}^{5} \overset{ij}{E}\,\overset{j}{D}_n + \sum_{j=1}^{5} \overset{ij}{F}\,\overset{j}{D}_s \end{aligned} \qquad (2\text{-}11)$$

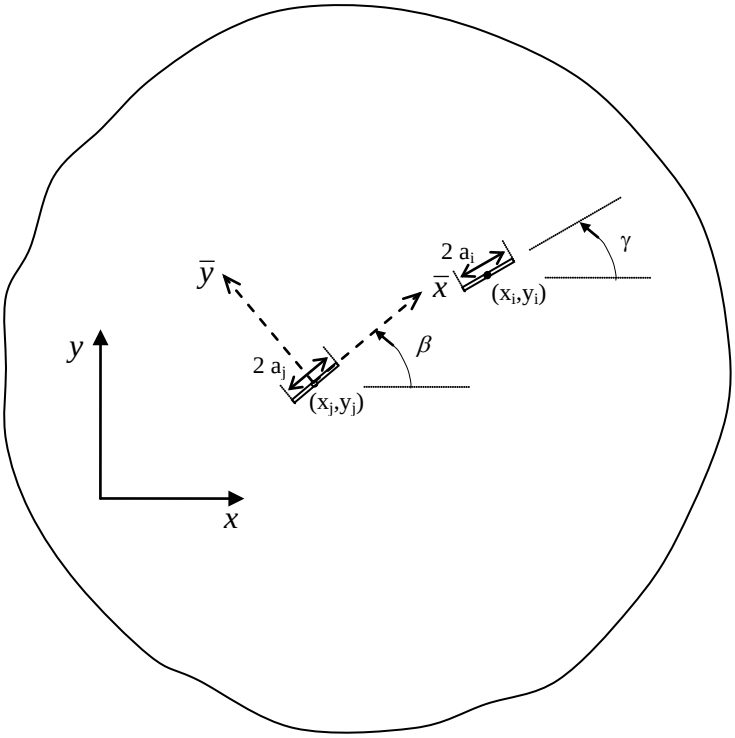

Figure II-4. Influence of *jth* fracture segment on the *ith* fracture segment in an elastic nonporous medium.

If the displacement discontinuities of the curvy fracture in the example shown in Figure II-2 are unknown variables, but the normal and shear stresses in the curvy fracture are known, the induced displacement discontinuities of the curvy fracture for the stresses on the fracture can be obtained by simultaneously solving the following 10 sets of linear equations (shown in matrix form) built from Eq. (2-11).

$$\begin{pmatrix} {}^{11}A & {}^{11}B & {}^{12}A & {}^{12}B & {}^{13}A & {}^{13}B & {}^{14}A & {}^{14}B & {}^{15}A & {}^{15}B \\ {}^{11}E & {}^{11}F & {}^{12}E & {}^{12}F & {}^{13}E & {}^{13}F & {}^{14}E & {}^{14}F & {}^{15}E & {}^{15}F \\ {}^{21}A & {}^{21}B & {}^{22}A & {}^{22}B & {}^{23}A & {}^{23}B & {}^{24}A & {}^{24}B & {}^{25}A & {}^{25}B \\ {}^{21}E & {}^{21}F & {}^{22}E & {}^{22}F & {}^{23}E & {}^{23}F & {}^{24}E & {}^{24}F & {}^{25}E & {}^{25}F \\ {}^{31}A & {}^{31}B & {}^{32}A & {}^{32}B & {}^{33}A & {}^{33}B & {}^{34}A & {}^{34}B & {}^{35}A & {}^{35}B \\ {}^{31}E & {}^{31}F & {}^{32}E & {}^{32}F & {}^{33}E & {}^{33}F & {}^{34}E & {}^{34}F & {}^{35}E & {}^{35}F \\ {}^{41}A & {}^{41}B & {}^{42}A & {}^{42}B & {}^{43}A & {}^{43}B & {}^{44}A & {}^{44}B & {}^{45}A & {}^{45}B \\ {}^{41}E & {}^{41}F & {}^{42}E & {}^{42}F & {}^{43}E & {}^{43}F & {}^{44}E & {}^{44}F & {}^{45}E & {}^{45}F \\ {}^{51}A & {}^{51}B & {}^{52}A & {}^{52}B & {}^{53}A & {}^{53}B & {}^{54}A & {}^{54}B & {}^{55}A & {}^{55}B \\ {}^{51}E & {}^{51}F & {}^{52}E & {}^{52}F & {}^{53}E & {}^{53}F & {}^{54}E & {}^{54}F & {}^{55}E & {}^{55}F \end{pmatrix} \begin{pmatrix} {}^{1}D_n \\ {}^{1}D_s \\ {}^{2}D_n \\ {}^{2}D_s \\ {}^{3}D_n \\ {}^{3}D_s \\ {}^{4}D_n \\ {}^{4}D_s \\ {}^{5}D_n \\ {}^{5}D_s \end{pmatrix} = \begin{pmatrix} {}^{1}\sigma_n \\ {}^{1}\sigma_s \\ {}^{2}\sigma_n \\ {}^{2}\sigma_s \\ {}^{3}\sigma_n \\ {}^{3}\sigma_s \\ {}^{4}\sigma_n \\ {}^{4}\sigma_s \\ {}^{5}\sigma_n \\ {}^{5}\sigma_s \end{pmatrix} \tag{2-12}$$

This method is for elastic nonporous media. Next section will give the DDM in porous media saturated with compressible single-phase fluid.

2.2 Fully coupled DDM for porous media saturated with a compressible single-phase fluid

The interaction of fluid and porous matrix plays a key role in the matrix deformation and fluid flow in the fluid-saturated porous media. The porous matrix

deformation causes pore pressure change, thereby causing pressure diffusion. A disturbance in the pore pressure also causes deformation of the solid matrix. Biot (1941) developed a theory of poroelasticity for a porous medium saturated with an incompressible fluid. The theory of poroelasticity was extended to the porous media saturated with compressible fluid by Rice and Cleary (1976). Based on the theory of poroelasticity, Carvalho (1990) gave the fundamental solutions of induced stress and pore pressure for a finite thin fracture segment with a fluid injection/production source in an infinite two-dimensional homogeneous and isotropic porous medium saturated with a compressible single-phase fluid. The induced stress and pore pressure by a single long fracture or many fractures with fluid injection/production can be obtained by discretizing the fracture or fractures into N fracture segments and summing the influences of all N fracture segments. If the induced stress and pore pressure in fractures are known, the normal and shear deformation of fractures and fluid injection/production rate (interface flow rate) in these fractures can be obtained by numerically solving a set of linear equations built from the fundamental solutions.

This section will start from the constitutive equations of a porous medium saturated with a compressible single-phase fluid in subsection 2.2.1. The constitutive equations give the relations of stress, pore pressure, strain and fluid volume changes. Then the pressure diffusion equation for flow in the porous medium will be given in subsection 2.2.2. Based on the coupled constitutive equations and the pressure diffusion equation, the fundamental solutions of induced stress and pore pressure for a single finite thin fracture segment under constant displacement discontinuities or constant rate fluid

injection/production in an infinite two-dimensional homogeneous and isotropic porous medium saturated with a compressible single-phase fluid will be given in subsection 2.2.3. Subsection 2.2.4 will describe how superposition of the fundamental solutions enables consideration of a long fracture or many fractures, and the subsection 2.2.5 will give a method for determining the normal and shear fracture deformation and fluid injection/production rate given the time dependent stress and pore pressure in fractures.

2.2.1 Constitutive equations of a porous medium saturated with a compressible single-phase fluid

The relation of stress to strain and pore pressure for a linear isotropic poroelastic medium is given by Biot's theory of poroelasticity (Biot, 1941):

$$\begin{aligned}
\sigma_{xx} &= 2G\left[e_{xx} + \frac{\upsilon}{1-2\upsilon}e_{kk}\right] - \alpha p \\
\sigma_{yy} &= 2G\left[e_{yy} + \frac{\upsilon}{1-2\upsilon}e_{kk}\right] - \alpha p \\
\sigma_{zz} &= 2G\left[e_{zz} + \frac{\upsilon}{1-2\upsilon}e_{kk}\right] - \alpha p \\
\sigma_{xy} &= 2Ge_{xy} \\
\sigma_{xz} &= 2Ge_{xz} \\
\sigma_{yz} &= 2Ge_{yz}
\end{aligned} \tag{2-13}$$

where σ_{xx}, σ_{yy}, σ_{zz}, σ_{xy}, σ_{xz}, and σ_{yz} are stress components and e_{xx}, e_{yy}, e_{zz}, e_{xy}, e_{xz}, and e_{yz} are strain components of the porous medium, e_{kk} is the volumetric strain ($e_{kk} = e_{xx} + e_{yy} + e_{zz}$), p is the pore pressure, α is Biot's poroelastic coefficient. *Tensile*

stress and strain are treated as positive in this dissertation. The strain is defined according to the displacement:

$$
\begin{aligned}
e_{xx} &= \frac{\partial u_x}{\partial x} \\
e_{yy} &= \frac{\partial u_y}{\partial y} \\
e_{zz} &= \frac{\partial u_z}{\partial z} \\
e_{xy} &= \frac{1}{2}\left(\frac{\partial u_x}{\partial y} + \frac{\partial u_y}{\partial x}\right) \\
e_{xz} &= \frac{1}{2}\left(\frac{\partial u_x}{\partial z} + \frac{\partial u_z}{\partial x}\right) \\
e_{yz} &= \frac{1}{2}\left(\frac{\partial u_y}{\partial z} + \frac{\partial u_z}{\partial y}\right)
\end{aligned}
\tag{2-14}
$$

where u_x, u_y and u_z are the components of displacement of the porous medium along x, y and z direction, respectively. The static solid is subject to the following force balance (Biot, 1941):

$$
\begin{aligned}
\frac{\partial \sigma_{xx}}{\partial x} + \frac{\partial \sigma_{xy}}{\partial y} + \frac{\partial \sigma_{xz}}{\partial z} &= 0 \\
\frac{\partial \sigma_{xy}}{\partial x} + \frac{\partial \sigma_{yy}}{\partial y} + \frac{\partial \sigma_{yz}}{\partial z} &= 0 \\
\frac{\partial \sigma_{xz}}{\partial x} + \frac{\partial \sigma_{yz}}{\partial y} + \frac{\partial \sigma_{zz}}{\partial z} &= 0
\end{aligned}
\tag{2-15}
$$

Combining Eqs. (2-13), (2-14) and (2-15) yields the Navier equation of poroelasticity:

$$
\begin{aligned}
&G\left(\frac{\partial^2 u_x}{\partial x^2}+\frac{\partial^2 u_x}{\partial y^2}+\frac{\partial^2 u_x}{\partial z^2}\right)+\frac{G}{1-2\nu}\left(\frac{\partial^2 u_x}{\partial x^2}+\frac{\partial^2 u_y}{\partial y\partial x}+\frac{\partial^2 u_z}{\partial z\partial x}\right)-\alpha\frac{\partial p}{\partial x}=0\\
&G\left(\frac{\partial^2 u_y}{\partial x^2}+\frac{\partial^2 u_y}{\partial y^2}+\frac{\partial^2 u_y}{\partial z^2}\right)+\frac{G}{1-2\nu}\left(\frac{\partial^2 u_x}{\partial x\partial y}+\frac{\partial^2 u_y}{\partial y^2}+\frac{\partial^2 u_z}{\partial z\partial y}\right)-\alpha\frac{\partial p}{\partial y}=0 \qquad (2\text{-}16)\\
&G\left(\frac{\partial^2 u_z}{\partial x^2}+\frac{\partial^2 u_z}{\partial y^2}+\frac{\partial^2 u_z}{\partial z^2}\right)+\frac{G}{1-2\nu}\left(\frac{\partial^2 u_x}{\partial x\partial z}+\frac{\partial^2 u_y}{\partial y\partial z}+\frac{\partial^2 u_z}{\partial z^2}\right)-\alpha\frac{\partial p}{\partial z}=0
\end{aligned}
$$

The total volumetric deformation (e_{kk}) of the porous medium consists of the pore space change (ς_p) and the deformation of the solid porous matrix (ς_s). The deformation of the solid porous matrix is due to the fluid pressure and effective stress loading:

(i) the effect of fluid pressure (the compression stress or strain is negative):

$$\varsigma_{s1}=-\frac{p}{K_s}(1-\phi) \qquad (2\text{-}17)$$

(ii) the effect of effective stress loading

$$\varsigma_{s2}=\frac{\sigma'_{kk}}{3K_s} \qquad (2\text{-}18)$$

where K_s is the bulk modulus of the solid and ϕ is the porosity. The average effective stress ($\sigma'_{kk}/3$) has the following relation with the volumetric strain and pore pressure (Carvalho, 1990):

$$\frac{\sigma'_{kk}}{3}=\frac{\sigma'_{xx}+\sigma'_{yy}+\sigma'_{zz}}{3}=K_m e_{kk}+\frac{K_m}{K_s}p \qquad (2\text{-}19)$$

where K_m ($K_m < K_s$) is the bulk modulus of the porous matrix. Combining Eqs. (2-17) and (2-18), and substituting Eq. (2-19) result in the deformation of the solid porous matrix:

$$\varsigma_s = \frac{K_m}{K_s} e_{kk} + \frac{p}{K_s}\left[\frac{K_m}{K_s} - (1-\phi)\right] \tag{2-20}$$

The pore space change is obtained by subtracting the deformation of the solid porous matrix from the total volumetric strain and using the definition of Biot's coefficient, α, ($\alpha = 1 - K_m / K_s$):

$$\varsigma_p = \alpha e_{kk} + (\alpha - \phi)\frac{p}{K_s} \tag{2-21}$$

2.2.2 Pressure diffusion in a porous medium

The fluid mass balance equation in a porous medium (matrix) gives that the fluid flowing into/out is equal to the sum of the increase of fluid mass in the pore space and injected/produced fluid:

$$-\frac{\partial(\rho_f q_x)}{\partial x} - \frac{\partial(\rho_f q_y)}{\partial y} - \frac{\partial(\rho_f q_z)}{\partial z} = \frac{\partial(\rho_f V_f)}{\partial t} - \rho_f q_s \tag{2-22}$$

where ρ_f is the fluid density, q_x, q_y, q_z are the fluid flow rate components in x, y, z direction, respectively, V_f is pore space, q_s is the injection/production rate and t is time. The fluid is compressible and the fluid density is pressure dependent:

$$\frac{\partial \rho_f}{\partial p} = c_o \rho_f \tag{2-23}$$

where c_o is the fluid (for example oil) compressibility.

In a unit volume porous media, the pore volume is ϕ, and the pore volume change is ς_p, and the RHS of Eq. (2-22) is rewritten as:

$$-\frac{\partial(\rho_f q_x)}{\partial x}-\frac{\partial(\rho_f q_y)}{\partial y}-\frac{\partial(\rho_f q_z)}{\partial z}=\phi\frac{\partial(\rho_f)}{\partial t}+\rho_f\frac{\partial(\varsigma_p)}{\partial t}-\rho_f q_s \tag{2-24}$$

Assuming Darcy's Law for fluid flow,

$$\begin{aligned} q_x &= -\frac{kA_x}{\mu}\frac{\partial p}{\partial x} \\ q_y &= -\frac{kA_y}{\mu}\frac{\partial p}{\partial y} \\ q_z &= -\frac{kA_z}{\mu}\frac{\partial p}{\partial z} \end{aligned} \tag{2-25}$$

where k is the matrix permeability and assumed as homogeneous and isotropic, A_x, A_y, A_z are the cross section areas in x, y, and z direction, respectively, and μ is the fluid viscosity.

Substituting Eqs.(2-21), (2-23) and (2-25) into Eq. (2-24), neglecting the term with $(\frac{\partial p}{\partial x_i})^2$ (Lee et al., 2003) and assuming small change in the pore volume (noting that the cross section area for a unit volume is 1) yield:

$$\frac{k}{\mu}\left(\frac{\partial^2 p}{\partial x^2}+\frac{\partial^2 p}{\partial y^2}+\frac{\partial^2 p}{\partial z^2}\right)=\frac{1}{M}\frac{\partial p}{\partial t}+\alpha\frac{\partial e_{kk}}{\partial t}-q_s \tag{2-26}$$

where $\frac{1}{M}=\phi c_o+\frac{\alpha-\phi}{K_s}$ and M is the Biot modulus. In Eq. (2-26), the left side is the net flow rate into the unit porous medium from the boundaries, the first right term $(\frac{1}{M}\frac{\partial p}{\partial t})$

is the fluid volume change due to the pore pressure change, the second right term ($\alpha \frac{\partial e_{kk}}{\partial t}$) is the fluid volume change due to the effective stress change, and the final term (q_s) is a source term.

2.2.3 Fundamental solutions for a single fracture segment in an infinite two-dimensional porous medium

The fundamental solutions of poroelastic DDM include induced stress, displacement and pore pressure from both the pressure/flow rate disturbance and the displacement discontinuities. For a plane strain condition (three-dimensions are simplified to two-dimensions), there is a constant discontinuity in the media and also constant flow (injection or production) along a thin fracture with a length of 2*a* from t=0 (Figure II-5). The initial conditions are defined in Eq. (2-27) and the inner and outer boundary conditions are defined in Eqs. (2-28) and (2-29). Since only the induced solutions for changes in stress, displacement and pore pressure are needed, the initial values of stress, displacement and pore pressure are set as zero.

(i) The initial conditions are given by

$$at \;\; t = 0, \forall x, y \qquad \begin{cases} p = 0 \\ u_x = u_y = 0 \\ \sigma_{xx} = \sigma_{yy} = \sigma_{xy} = 0 \end{cases} \tag{2-27}$$

(ii) Boundary conditions are given by

Inner boundary:

$$at\ y=0,\ |x|\le a\quad \begin{cases} u_x\left(x,0^-\right)-u_x\left(x,0^+\right)=D_s \\ u_y\left(x,0^-\right)-u_y\left(x,0^+\right)=D_n \\ q_s=-2a\,q_0 \end{cases} \tag{2-28}$$

where q_0 is a unit flow rate (q_0=1 m^3/sec).

Outer boundary:

$$at\ \sqrt{x^2+y^2}\to\infty\quad \begin{cases} u_x=u_y=0 \\ \sigma_{xx}=\sigma_{yy}=\sigma_{xy}=p=0 \end{cases} \tag{2-29}$$

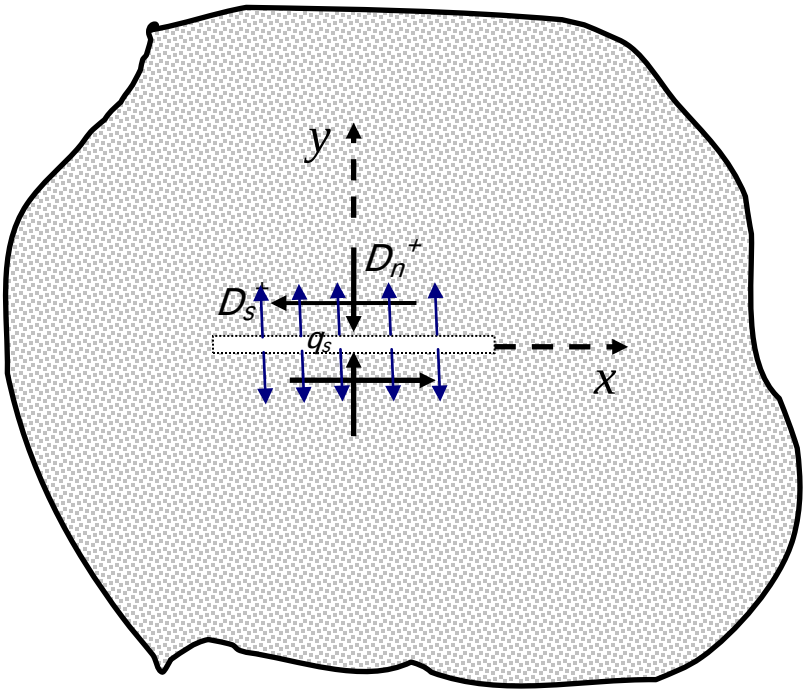

Figure II-5. A thin line fracture in an infinite two-dimensional elastic porous medium, and the line fracture starts from (-a,0) and ends at (a,0).

Using the initial and boundary conditions (Eqs. (2-27) – (2-29)), Eqs. (2-16) and (2-26) can be solved for separate inner boundary conditions – constant volume flow rate injection/production ($u_x(x, 0^-)- u_x(x, 0^+)=0$, $u_y(x, 0^-)- u_y(x, 0^+)=0$, $qs =-2aq_0$) at the inner boundary and constant displacement discontinuity (DD) ($u_x(x, 0^-)- u_x(x, 0^+)=D_s$, $u_y(x, 0^-)- u_y(x, 0^+)= D_n$, $qs =0$) at the inner boundary (Carvalho, 1990). The induced displacement, pore pressure and stress at any point (x, y) and time t by the constant volume injection/production rate and by the displacement discontinuities including normal and shear displacement discontinuities through the fracture segment are given in the Appendix A and Appendix B, respectively (Carvalho, 1990). The final fundamental solutions for poroelastic DDM are obtained by combining the solutions of the constant volume rate fluid injection/production and the constant displacement discontinuities in the fracture segment.

Induced pore pressure:

$$p(x,y,t) = p^{dn}(x,y,t)\,D_n + p^{ds}(x,y,t)\,D_s + p^{q}(x,y,t)\,q_{\text{int}} \tag{2-30}$$

Induced displacement:

$$\begin{aligned} u_x(x,y,t) &= u_x^{dn}(x,y,t)\,D_n + u_x^{ds}(x,y,t)\,D_s + u_x^{q}(x,y,t)\,q_{\text{int}} \\ u_y(x,y,t) &= u_y^{dn}(x,y,t)\,D_n + u_y^{ds}(x,y,t)\,D_s + u_y^{q}(x,y,t)\,q_{\text{int}} \end{aligned} \tag{2-31}$$

Induced stress:

$$\sigma_{xx}(x,y,t) = \sigma_{xx}^{dn}(x,y,t)\,D_n + \sigma_{xx}^{ds}(x,y,t)\,D_s + \sigma_{xx}^{q}(x,y,t)\,q_{\text{int}}$$

$$\sigma_{yy}(x,y,t) = \sigma_{yy}^{dn}(x,y,t)\,D_n + \sigma_{yy}^{ds}(x,y,t)\,D_s + \sigma_{yy}^{q}(x,y,t)\,q_{\text{int}} \qquad (2\text{-}32)$$

$$\sigma_{xy}(x,y,t) = \sigma_{xy}^{dn}(x,y,t)\,D_n + \sigma_{xy}^{ds}(x,y,t)\,D_s + \sigma_{xy}^{q}(x,y,t)\,q_{\text{int}}$$

where D_n and D_s are the normal and shear displacement discontinuity sources, and q_{int} is the fluid source term in a fracture (interface flow rate between fracture and matrix), and the superscripts *dn*, *ds* and *q* denote normal displacement discontinuity source, shear displacement discontinuity source and fluid source, respectively. The induced pore pressure, p^q, displacement in *x* direction, u_x^q and in *y* direction, u_y^q, stress components, σ_{xx}^q, σ_{yy}^q and σ_{xy}^q by the constant rate fluid injection/production from a fracture segment are listed in Appendix A. The induced pore pressure, p^{dn} and p^{ds}, displacement in *x* direction, u_x^{dn} and u_x^{ds}, and in *y* direction, u_y^{dn} and u_y^{ds}, stress components, σ_{xx}^{dn}, σ_{yy}^{dn}, σ_{xy}^{dn}, σ_{xx}^{ds}, σ_{yy}^{ds} and σ_{xy}^{ds} by the constant normal and shear discontinuous displacement of a fracture segment are listed in Appendix B.

2.2.4 Solutions for multiple fracture segments in an infinite two-dimensional porous medium

For a long fracture or many fractures in a porous medium saturated with a compressible single-phase fluid, the induced stresses and pore pressure can be approximated by summing the fundamental solutions for a system of fracture segments. Figure II-6 shows a *porous* medium containing a curvy fracture like the one in section

2.1 that was in a *nonporous* medium. The curvy fracture is discretized into 5 fracture segments shown in Figure II-6. To apply the fundamental solutions to the *jth* fracture segment, it is necessary to transform the *x*, *y* co-ordinates of the segment into the local $\bar{x}$, $\bar{y}$ co-ordinate system using the transformation formula in Eq. (2-3). The pore pressure and stresses induced by the normal and shear displacement discontinuities and the fluid injection/production of the *jth* fracture segment in the local $\bar{x}$, $\bar{y}$ co-ordinate system (Figure II-7) are given in Eqs. (2-33) and (2-34), respectively.

Induced pore pressure:

$$\overset{j}{p}(\bar{x},\bar{y},t) = \overset{j}{p^{dn}}(\bar{x},\bar{y},t)\overset{j}{D}_n + \overset{j}{p^{ds}}(\bar{x},\bar{y},t)\overset{j}{D}_s + \overset{j}{p^{q}}(\bar{x},\bar{y},t)\overset{j}{q}_{\text{int}} \tag{2-33}$$

Induced stress:

$$\overset{j}{\sigma}_{\bar{x}\bar{x}}(\bar{x},\bar{y},t) = \overset{j}{\sigma^{dn}_{\bar{x}\bar{x}}}(\bar{x},\bar{y},t)\overset{j}{D}_n + \overset{j}{\sigma^{ds}_{\bar{x}\bar{x}}}(\bar{x},\bar{y},t)\overset{j}{D}_s + \overset{j}{\sigma^{q}_{\bar{x}\bar{x}}}(\bar{x},\bar{y},t)\overset{j}{q}_{\text{int}}$$

$$\overset{j}{\sigma}_{\bar{y}\bar{y}}(\bar{x},\bar{y},t) = \overset{j}{\sigma^{dn}_{\bar{y}\bar{y}}}(\bar{x},\bar{y},t)\overset{j}{D}_n + \overset{j}{\sigma^{ds}_{\bar{y}\bar{y}}}(\bar{x},\bar{y},t)\overset{j}{D}_s + \overset{j}{\sigma^{q}_{\bar{y}\bar{y}}}(\bar{x},\bar{y},t)\overset{j}{q}_{\text{int}} \tag{2-34}$$

$$\overset{j}{\sigma}_{\bar{x}\bar{y}}(\bar{x},\bar{y},t) = \overset{j}{\sigma^{dn}_{\bar{x}\bar{y}}}(\bar{x},\bar{y},t)\overset{j}{D}_n + \overset{j}{\sigma^{ds}_{\bar{x}\bar{y}}}(\bar{x},\bar{y},t)\overset{j}{D}_s + \overset{j}{\sigma^{q}_{\bar{x}\bar{y}}}(\bar{x},\bar{y},t)\overset{j}{q}_{\text{int}}$$

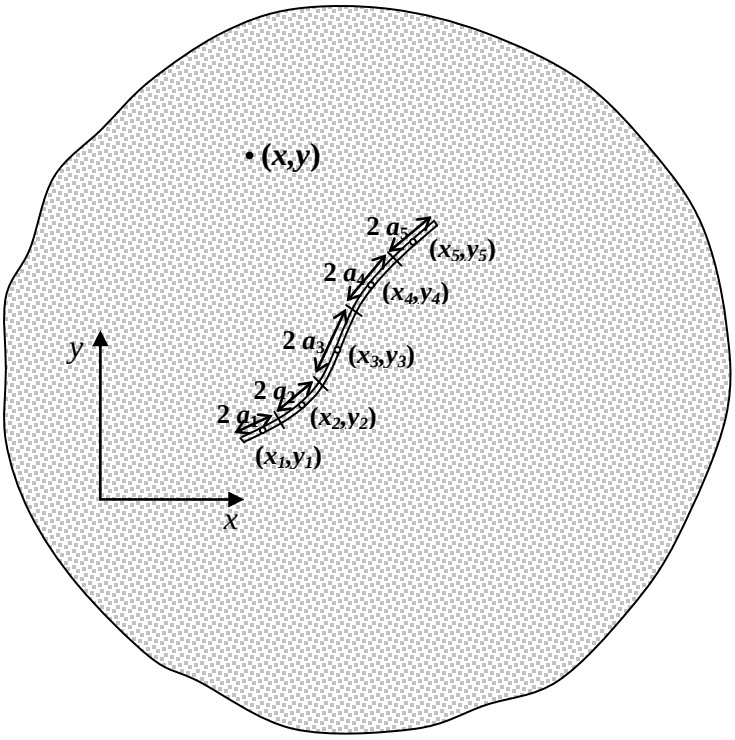

Figure II-6. A curvy fracture discretized into 5 segments in an infinite two-dimensional porous medium saturated with a single-phase fluid.

The stresses induced by the *jth* fracture segment in the local $\bar{x}$, $\bar{y}$ co-ordinate system can be transformed to the *x, y* co-ordinate system using the transformation formula in Eq. (2-6). Now the induced stresses from all 5 fracture segments can be obtained by superposition. (Eq. (2-7)). As the pore pressure is a scalar, it is independent of the orientation of the co-ordinate system. The induced pore pressure by the *jth* fracture in the *x, y* co-ordinate system is the same as that in the local $\bar{x}$, $\bar{y}$ co-ordinate system.

$$\overset{j}{p}(x, y, t) = \overset{j}{p}(\bar{x}, \bar{y}, t), \tag{2-35}$$

And the induced pore pressure by the curvy fracture can be obtained by summing the induced pore pressure from all 5 fracture segments.

$$p(x,y,t)=\sum_{j=1}^{5} {}^{j}p(x,y,t) \tag{2-36}$$

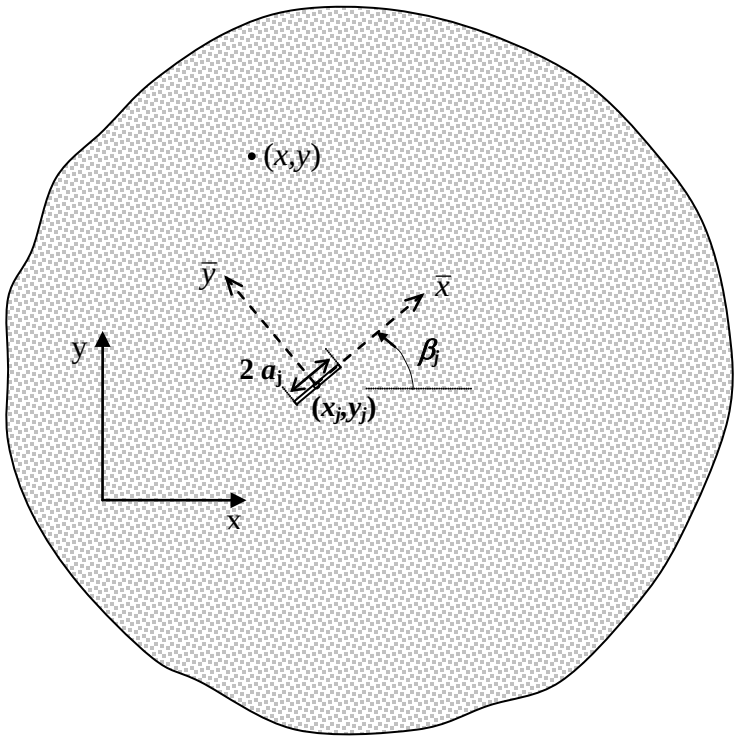

Figure II-7. Local co-ordinate for the *jth* fracture segment in a porous medium.

The normal and shear stresses induced on the *ith* fracture segment by the *jth* fracture segment shown in Figure II-8 are obtained by projecting the stresses in Eq. (2-34) to the plane of the *ith* fracture using the formula in Eq. (2-8). The normal and shear stresses and pore pressure induced on the *ith* fracture segment by the constant rate fluid injection/production and the constant normal and shear displacement discontinuities of the *jth* fracture are:

$$\overset{ij}{\sigma}_n = \overset{ij}{A}\,\overset{j}{D}_n + \overset{ij}{B}\,\overset{j}{D}_s + \overset{ij}{C}\,\overset{j}{q}_{\text{int}}$$

$$\overset{ij}{\sigma}_s = \overset{ij}{E}\,\overset{j}{D}_n + \overset{ij}{F}\,\overset{j}{D}_s + \overset{ij}{K}\,\overset{j}{q}_{\text{int}} \qquad (2\text{-}37)$$

$$\overset{ij}{p} = \overset{ij}{L}\,\overset{j}{D}_n + \overset{ij}{H}\,\overset{j}{D}_s + \overset{ij}{N}\,\overset{j}{q}_{\text{int}}$$

where

$$\overset{ij}{A}\left(\overset{ij}{x},\overset{ij}{y},t\right) = \cos^2\overset{ij}{\gamma}\,\overset{j}{\sigma}^{dn}_{\overline{xx}}\left(\overset{ij}{x},\overset{ij}{y},t\right) + \sin 2\overset{ij}{\gamma}\,\overset{j}{\sigma}^{dn}_{\overline{xy}}\left(\overset{ij}{x},\overset{ij}{y},t\right) + \sin^2\overset{ij}{\gamma}\,\overset{j}{\sigma}^{dn}_{\overline{yy}}\left(\overset{ij}{x},\overset{ij}{y},t\right)$$

$$\overset{ij}{B}\left(\overset{ij}{x},\overset{ij}{y},t\right) = \cos^2\overset{ij}{\gamma}\,\overset{j}{\sigma}^{ds}_{\overline{xx}}\left(\overset{ij}{x},\overset{ij}{y},t\right) + \sin 2\overset{ij}{\gamma}\,\overset{j}{\sigma}^{ds}_{\overline{xy}}\left(\overset{ij}{x},\overset{ij}{y},t\right) + \sin^2\overset{ij}{\gamma}\,\overset{j}{\sigma}^{ds}_{\overline{yy}}\left(\overset{ij}{x},\overset{ij}{y},t\right)$$

$$\overset{ij}{C}\left(\overset{ij}{x},\overset{ij}{y},t\right) = \cos^2\overset{ij}{\gamma}\,\overset{j}{\sigma}^{q}_{\overline{xx}}\left(\overset{ij}{x},\overset{ij}{y},t\right) + \sin 2\overset{ij}{\gamma}\,\overset{j}{\sigma}^{q}_{\overline{xy}}\left(\overset{ij}{x},\overset{ij}{y},t\right) + \sin^2\overset{ij}{\gamma}\,\overset{j}{\sigma}^{q}_{\overline{yy}}\left(\overset{ij}{x},\overset{ij}{y},t\right)$$

$$\overset{ij}{E}\left(\overset{ij}{x},\overset{ij}{y},t\right) = \sin\overset{ij}{\gamma}\cos\overset{ij}{\gamma}\left(\overset{j}{\sigma}^{dn}_{\overline{xx}}\left(\overset{ij}{x},\overset{ij}{y},t\right) - \overset{j}{\sigma}^{dn}_{\overline{yy}}\left(\overset{ij}{x},\overset{ij}{y},t\right)\right) - \left(\cos^2\overset{ij}{\gamma} - \sin^2\overset{ij}{\gamma}\right)\overset{j}{\sigma}^{dn}_{\overline{xy}}\left(\overset{ij}{x},\overset{ij}{y},t\right)$$

$$\overset{ij}{F}\left(\overset{ij}{x},\overset{ij}{y},t\right) = \sin\overset{ij}{\gamma}\cos\overset{ij}{\gamma}\left(\overset{j}{\sigma}^{ds}_{\overline{xx}}\left(\overset{ij}{x},\overset{ij}{y},t\right) - \overset{j}{\sigma}^{ds}_{\overline{yy}}\left(\overset{ij}{x},\overset{ij}{y},t\right)\right) - \left(\cos^2\overset{ij}{\gamma} - \sin^2\overset{ij}{\gamma}\right)\overset{j}{\sigma}^{ds}_{\overline{xy}}\left(\overset{ij}{x},\overset{ij}{y},t\right) \qquad (2\text{-}38)$$

$$\overset{ij}{K}\left(\overset{ij}{x},\overset{ij}{y},t\right) = \sin\overset{ij}{\gamma}\cos\overset{ij}{\gamma}\left(\overset{j}{\sigma}^{q}_{\overline{xx}}\left(\overset{ij}{x},\overset{ij}{y},t\right) - \overset{j}{\sigma}^{q}_{\overline{yy}}\left(\overset{ij}{x},\overset{ij}{y},t\right)\right) - \left(\cos^2\overset{ij}{\gamma} - \sin^2\overset{ij}{\gamma}\right)\overset{j}{\sigma}^{q}_{\overline{xy}}\left(\overset{ij}{x},\overset{ij}{y},t\right)$$

$$\overset{ij}{L}\left(\overset{ij}{x},\overset{ij}{y},t\right) = \overset{j}{p}^{dn}\left(\overset{ij}{x},\overset{ij}{y},t\right)$$

$$\overset{ij}{H}\left(\overset{ij}{x},\overset{ij}{y},t\right) = \overset{j}{p}^{ds}\left(\overset{ij}{x},\overset{ij}{y},t\right)$$

$$\overset{ij}{N}\left(\overset{ij}{x},\overset{ij}{y},t\right) = \overset{j}{p}^{q}\left(\overset{ij}{x},\overset{ij}{y},t\right)$$

where

$$\overset{ij}{x} = \left(x_i - x_j\right)\cos\beta_j + \left(y_i - y_j\right)\sin\beta_j$$

$$\overset{ij}{y} = -\left(x_i - x_j\right)\sin\beta_j + \left(y_i - y_j\right)\cos\beta_j \qquad (2\text{-}39)$$

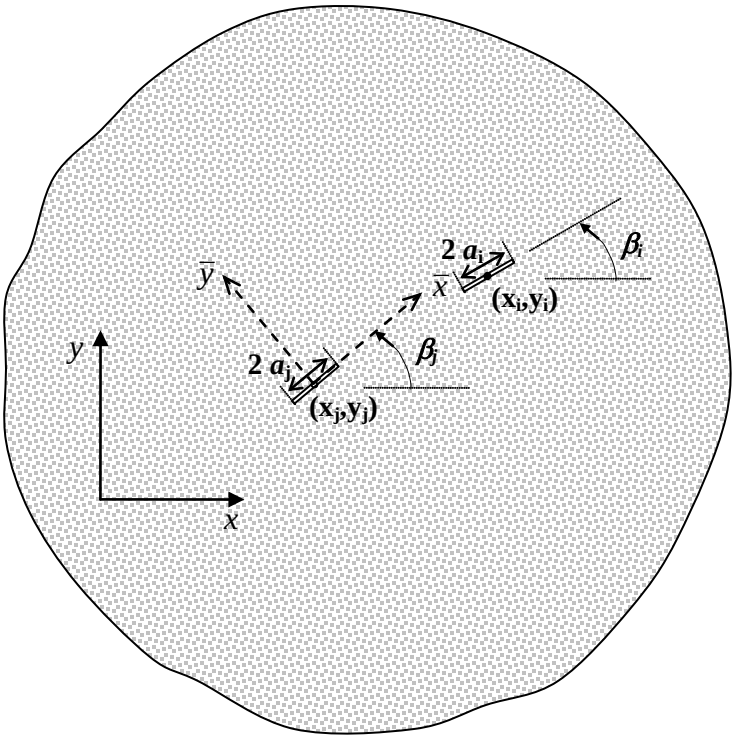

Figure II-8. Influence of the *jth* fracture segment on the *ith* fracture segment in an elastic porous medium.

The normal and shear stresses and pore pressure induced on the *ith* fracture segment by the constant rate fluid injection/production and constant normal and shear displacement discontinuities of all fracture segments are obtained by summing the solutions in Eq. (2-37).

$$\overset{i}{\sigma}_n = \sum_{j=1}^{5} \overset{ij}{A}\,\overset{j}{D}_n + \sum_{j=1}^{5} \overset{ij}{B}\,\overset{j}{D}_s + \sum_{j=1}^{5} \overset{ij}{C}\,\overset{j}{q}_{\text{int}}$$

$$\overset{i}{\sigma}_s = \sum_{j=1}^{5} \overset{ij}{E}\,\overset{j}{D}_n + \sum_{j=1}^{5} \overset{ij}{F}\,\overset{j}{D}_s + \sum_{j=1}^{5} \overset{ij}{K}\,\overset{j}{q}_{\text{int}} \qquad \text{(2-40)}$$

$$\overset{i}{p} = \sum_{j=1}^{5} \overset{ij}{L}\,\overset{j}{D}_n + \sum_{j=1}^{5} \overset{ij}{H}\,\overset{j}{D}_s + \sum_{j=1}^{5} \overset{ij}{N}\,\overset{j}{q}_{\text{int}}$$

2.2.5 Determination of the fracture discontinuous displacement

Up to now we have determined normal and shear stresses and pressure given discontinuous displacements in the fractures and fluid injection/production sources. However, the practical application may require determination of the fracture discontinuous displacement given stress and fluid pressure in fractures. Because the stress and pore pressure changes induced by the constant rate fluid injection/production and displacement discontinuities of fractures are a function of time, it is necessary to account for the time dependent changes. For time dependent normal displacement discontinuity, D_n, shear displacement discontinuity, D_s, or injection/production flow rate (interface flow rate between fracture and matrix), q_{int}, a time marching scheme like that shown in Figure II-9 is used to discretize the time dependent quantity into N constant steps and use superposition to account for each step change at the time it occurs. The constant step source except for the first one does not start at the time zero (t=0). Thus a time shift is needed to apply the fundamental solution and the influence coefficients. For example, at time τ_ξ, if constant $\Delta D_n(x_j,y_j,\tau_\xi)$, $\Delta D_s(x_j,y_j,\tau_\xi)$ and $\Delta q_{int}(x_j,y_j,\tau_\xi)$ of the *jth* fracture segment are added, the induced stresses and pore pressure on the *ith* fracture segment at time t by the added sources will be :

$$\overset{i}{\sigma}_n = \sum_{j=1}^{5} \overset{ij}{A}\left(t-\tau_\xi\right)\Delta \overset{j\xi}{D}_n + \sum_{j=1}^{5} \overset{ij}{B}\left(t-\tau_\xi\right)\Delta \overset{j\xi}{D}_s + \sum_{j=1}^{5} \overset{ij}{C}\left(t-\tau_\xi\right)\Delta \overset{j\xi}{q}_{\text{int}}$$

$$\overset{i}{\sigma}_s = \sum_{j=1}^{5} \overset{ij}{E}\left(t-\tau_\xi\right)\Delta \overset{j\xi}{D}_n + \sum_{j=1}^{5} \overset{ij}{F}\left(t-\tau_\xi\right)\Delta \overset{j\xi}{D}_s + \sum_{j=1}^{5} \overset{ij}{K}\left(t-\tau_\xi\right)\Delta \overset{j\xi}{q}_{\text{int}} \qquad (2\text{-}41)$$

$$\overset{i}{p} = \sum_{j=1}^{5} \overset{ij}{L}\left(t-\tau_\xi\right)\Delta \overset{j\xi}{D}_n + \sum_{j=1}^{5} \overset{ij}{H}\left(t-\tau_\xi\right)\Delta \overset{j\xi}{D}_s + \sum_{j=1}^{5} \overset{ij}{N}\left(t-\tau_\xi\right)\Delta \overset{j\xi}{q}_{\text{int}}$$

where $\Delta \overset{j\xi}{D}_n$, $\Delta \overset{j\xi}{D}_s$ and $\Delta \overset{j\xi}{q}_{\text{int}}$ denote the increments of normal displacement discontinuity, shear displacement discontinuity and injection/production flow rate (interface flow rate) of the *jth* fracture segment at time τ_ξ. $\overset{ij}{A}\left(t-\tau_\xi\right)$, $\overset{ij}{B}\left(t-\tau_\xi\right)$, $\overset{ij}{C}\left(t-\tau_\xi\right)$, $\overset{ij}{E}\left(t-\tau_\xi\right)$, $\overset{ij}{F}\left(t-\tau_\xi\right)$, $\overset{ij}{K}\left(t-\tau_\xi\right)$, $\overset{ij}{L}\left(t-\tau_\xi\right)$, $\overset{ij}{H}\left(t-\tau_\xi\right)$, and $\overset{ij}{N}\left(t-\tau_\xi\right)$ are the influence coefficients of *jth* fracture segment on the *ith* fracture element at time step ξ and defined in the Eq. (2-38). The total induced stresses and pore pressure on the *ith* fracture segment at time *t* are obtained by summing the influences from all time steps.

$$\overset{i}{\sigma}_n(t) = \sum_{h=0}^{\xi}\sum_{j=1}^{5} \overset{ij}{A}\left(t-\tau_h\right)\Delta \overset{jh}{D}_n + \sum_{h=0}^{\xi}\sum_{j=1}^{5} \overset{ij}{B}\left(t-\tau_h\right)\Delta \overset{jh}{D}_s + \sum_{h=0}^{\xi}\sum_{j=1}^{5} \overset{ij}{C}\left(t-\tau_h\right)\Delta \overset{jh}{q}_{\text{int}}$$

$$\overset{i}{\sigma}_s(t) = \sum_{h=0}^{\xi}\sum_{j=1}^{5} \overset{ij}{E}\left(t-\tau_h\right)\Delta \overset{jh}{D}_n + \sum_{h=0}^{\xi}\sum_{j=1}^{5} \overset{ij}{F}\left(t-\tau_h\right)\Delta \overset{jh}{D}_s + \sum_{h=0}^{\xi}\sum_{j=1}^{5} \overset{ij}{K}\left(t-\tau_h\right)\Delta \overset{jh}{q}_{\text{int}} \qquad (2\text{-}42)$$

$$\overset{i}{p}(t) = \sum_{h=0}^{\xi}\sum_{j=1}^{5} \overset{ij}{L}\left(t-\tau_h\right)\Delta \overset{jh}{D}_n + \sum_{h=0}^{\xi}\sum_{j=1}^{5} \overset{ij}{H}\left(t-\tau_h\right)\Delta \overset{jh}{D}_s + \sum_{h=0}^{\xi}\sum_{j=1}^{5} \overset{ij}{N}\left(t-\tau_h\right)\Delta \overset{jh}{q}_{\text{int}}$$

where *h* is the time step index.

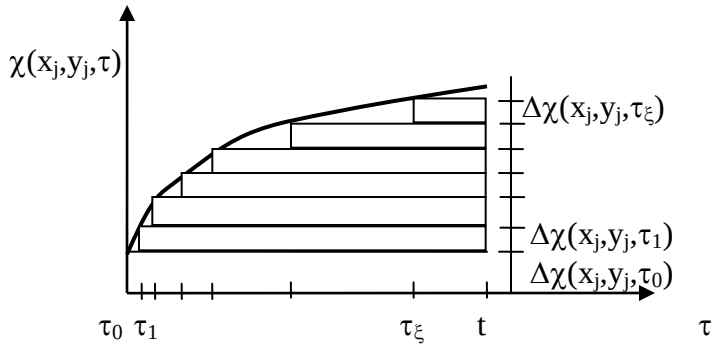

Figure II-9. Time marching scheme, χ represents D_n, D_s or q_{int}.

If the induced stresses and pore pressure at all fracture segments shown in Figure II-6 are known, the step change of normal and shear displacement discontinuities and injection/production flow rate can be solved from τ_0 to τ_ξ. Firstly, at time τ_0 (τ_0=0), the induced stresses and pore pressure on the *ith* fracture segment from τ_0 to τ_1 are known, Eq. (2-42) is rewritten as Eq. (2-43) (note that there is only one time step).

$$\begin{aligned}
\overset{i}{\sigma}_n(\tau_1) &= \sum_{j=1}^{5} \overset{ij}{A}(\tau_1-\tau_0)\,\Delta \overset{j0}{D}_n + \sum_{j=1}^{5} \overset{ij}{B}(\tau_1-\tau_0)\,\Delta \overset{j0}{D}_s + \sum_{j=1}^{5} \overset{ij}{C}(\tau_1-\tau_0)\,\Delta \overset{j0}{q}_{\text{int}} \\
\overset{i}{\sigma}_s(\tau_1) &= \sum_{j=1}^{5} \overset{ij}{E}(\tau_1-\tau_0)\,\Delta \overset{j0}{D}_n + \sum_{j=1}^{5} \overset{ij}{F}(\tau_1-\tau_0)\,\Delta \overset{j0}{D}_s + \sum_{j=1}^{5} \overset{ij}{K}(\tau_1-\tau_0)\,\Delta \overset{j0}{q}_{\text{int}} \qquad (2\text{-}43) \\
\overset{i}{p}(\tau_1) &= \sum_{j=1}^{5} \overset{ij}{L}(\tau_1-\tau_0)\,\Delta \overset{j0}{D}_n + \sum_{j=1}^{5} \overset{ij}{H}(\tau_1-\tau_0)\,\Delta \overset{j0}{D}_s + \sum_{j=1}^{5} \overset{ij}{N}(\tau_1-\tau_0)\,\Delta \overset{j0}{q}_{\text{int}}
\end{aligned}$$

One set of linear equations can be built from Eq. (2-43), and the increment of normal displacement discontinuity, shear displacement discontinuity and injection/production flow rate (interface flow rate) for all fracture segments at time τ_0 can be solved from the set of linear equations. By the similar way, the step sources at other time steps can be

solved. For the last time step, the induced stresses and pore pressure at time *t* are known and the step sources before the step τ_ξ are already solved, and only the last step sources are not known and need to be solved (2-44).

$$\begin{aligned}
&\sum_{j=1}^{5} {}^{ij}A\left(t-\tau_\xi\right)\Delta {}^{j\xi}D_n+\sum_{j=1}^{5} {}^{ij}B\left(t-\tau_\xi\right)\Delta {}^{j\xi}D_s+\sum_{j=1}^{5} {}^{ij}C\left(t-\tau_\xi\right)\Delta {}^{j\xi}q_{\text{int}}= \\
&{}^{i}\sigma_n(t)-\sum_{h=0}^{\xi-1}\sum_{j=1}^{5} {}^{ij}A\left(t-\tau_h\right)\Delta {}^{jh}D_n-\sum_{h=0}^{\xi-1}\sum_{j=1}^{5} {}^{ij}B\left(t-\tau_h\right)\Delta {}^{jh}D_s-\sum_{h=0}^{\xi-1}\sum_{j=1}^{5} {}^{ij}C\left(t-\tau_h\right)\Delta {}^{jh}q_{\text{int}} \\
&\sum_{j=1}^{5} {}^{ij}E\left(t-\tau_\xi\right)\Delta {}^{j\xi}D_n+\sum_{j=1}^{5} {}^{ij}F\left(t-\tau_\xi\right)\Delta {}^{j\xi}D_s+\sum_{j=1}^{5} {}^{ij}K\left(t-\tau_\xi\right)\Delta {}^{j\xi}q_{\text{int}}= \\
&{}^{i}\sigma_s(t)-\sum_{h=0}^{\xi-1}\sum_{j=1}^{5} {}^{ij}E\left(t-\tau_h\right)\Delta {}^{jh}D_n-\sum_{h=0}^{\xi-1}\sum_{j=1}^{5} {}^{ij}F\left(t-\tau_h\right)\Delta {}^{jh}D_s-\sum_{h=0}^{\xi-1}\sum_{j=1}^{5} {}^{ij}K\left(t-\tau_h\right)\Delta {}^{jh}q_{\text{int}} \\
&\sum_{j=1}^{5} {}^{ij}L\left(t-\tau_\xi\right)\Delta {}^{j\xi}D_n+\sum_{j=1}^{5} {}^{ij}H\left(t-\tau_\xi\right)\Delta {}^{j\xi}D_s+\sum_{j=1}^{5} {}^{ij}N\left(t-\tau_\xi\right)\Delta {}^{j\xi}q_{\text{int}}= \\
&{}^{i}p(t)-\sum_{h=0}^{\xi-1}\sum_{j=1}^{5} {}^{ij}L\left(t-\tau_h\right)\Delta {}^{jh}D_n-\sum_{h=0}^{\xi-1}\sum_{j=1}^{5} {}^{ij}H\left(t-\tau_h\right)\Delta {}^{jh}D_s-\sum_{h=0}^{\xi-1}\sum_{j=1}^{5} {}^{ij}N\left(t-\tau_h\right)\Delta {}^{jh}q_{\text{int}}
\end{aligned} \tag{2-44}$$

Another set of linear equations can be built from Eq. (2-44) and the increment of normal displacement discontinuity, shear displacement discontinuity and injection/production flow rate /interface flow rate for all fracture segments at time τ_ξ can be solved from the set of linear equations. The final normal and shear displacement discontinuities and injection/production flow rate (interface flow rate) of every fracture segment at time *t* can be obtained by summing all of these step increments.

$$\overset{j}{D}_n = \sum_{h=0}^{\xi} \Delta \overset{jh}{D}_n$$

$$\overset{j}{D}_s = \sum_{h=0}^{\xi} \Delta \overset{jh}{D}_s \qquad (2\text{-}45)$$

$$\overset{j}{q}_{\text{int}} = \sum_{h=0}^{\xi} \Delta \overset{jh}{q}_{\text{int}}$$

2.3 Model verification

It is difficult to find analytical solutions for most real problems. Numerical methods have the advantage to solve the real problems sometimes with very complicated boundary conditions. A few special problems with simple boundary conditions can be solved analytically, and these analytical solutions are very helpful to check and verify the numerical solution by the DDM. Here, the DDM is applied to a line crack in an infinite medium.

An infinitely thin line crack with a length of ΔL in an infinite elastic medium is subject to a constant pressure (tensile stress) p along the crack surfaces (Figure II-10). The normal relative displacement of the two crack surfaces (opening), w_f, was solved by Sneddon (1951).

$$w_f = \frac{(1-\nu) p \Delta L}{G} \sqrt{1 - \frac{x^2}{(\Delta L/2)^2}} \qquad (2\text{-}46)$$

where $-\Delta L/2 \le x \le \Delta L/2$.

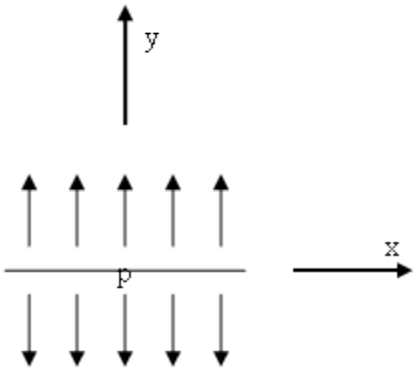

Figure II-10. A line crack with constant pressure loading.

This problem can be solved using the DDM. The line crack is separated into *N* segments, each of which represents an elemental displacement discontinuity. And the displacement of every segment can be solved by applying the boundary conditions (constant pressure along the crack surfaces). For a elastic nonporous medium with a shear modulus of 9.06×10^5 psi and a Poisson's ratio of 0.2, there is an infinite thin line crack with a length of 39.37 in, and a constant injection pressure of 145 psi above the reservoir pressure ($\Delta p = p_{inj} - p_0 =$ 145 psi) applied to the crack surfaces. The original crack aperture is assumed as zero and the effective stress is zero. Figure II-11 shows that the crack width modeled using the DDM is consistent with the analytical solution.

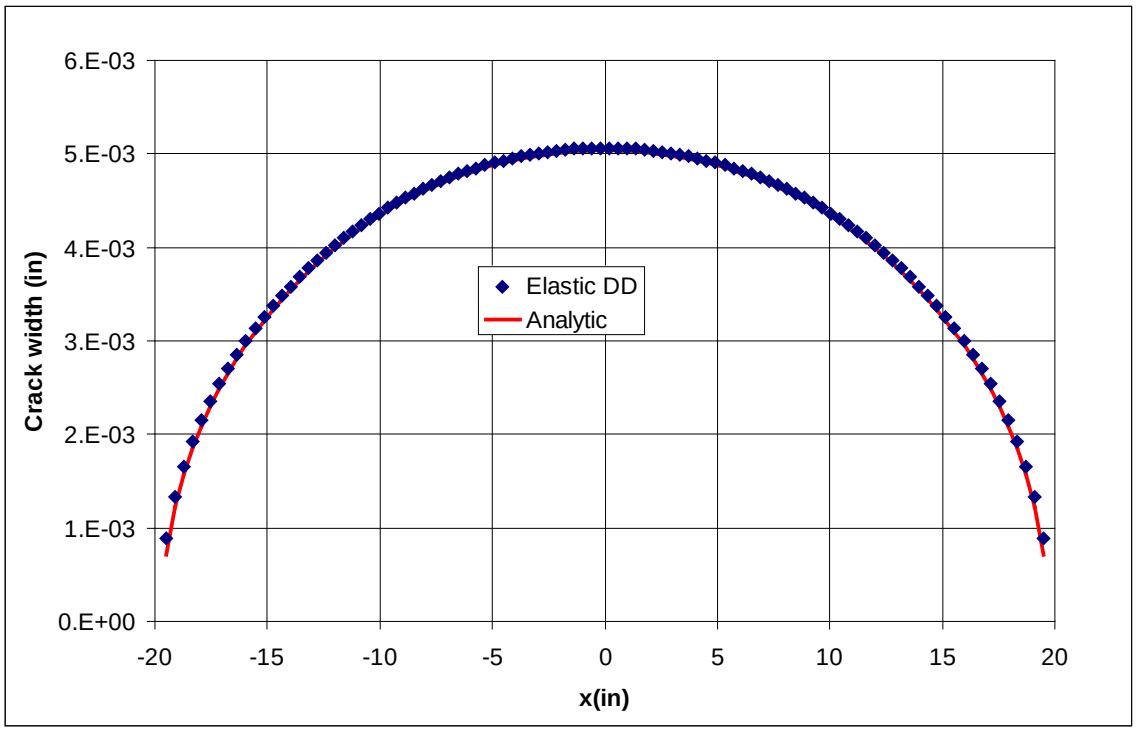

Figure II-11. Comparison of the modeled crack width using elastic DD with the analytical solution.

If the elastic porous medium is saturated with fluid, a constant fluid pressure applied to the crack surfaces will cause a transient crack opening. In addition to the stress applied to the crack surfaces, there is also a fluid pressure applied to the pore pressure field in the porous medium. It is common to separate the pressure application into two loading processes (Detournay and Cheng, 1988): (i) Mode I loading – normal stress loading; (ii) Mode II loading – pore pressure loading. Mode I loading tends to open the crack. But the opening of crack will cause a compression on the porous material around the crack. At very early time stage, the fluid in the pores cannot move out and the porous material shows undrained behavior, and the pore pressure around the crack has an instant increase. The induced pore pressure dissipates and decreases with

time until it reaches a drained stage with no pore pressure gradient. The crack width increases when the poroelastic material changes from undrained stage at early time to the drained stage at long time as the pore pressure dissipates and the material around the crack becomes more "soft". Mode II loading tends to reduce the crack opening as the fluid flows into the porous material around the crack and increase the pore pressure which tends to cause an expansion of the porous material around the crack.

Considering the Mode I and Mode II loading processes for the same crack and loading as before and poroelastic and fluid parameters listed in **Table II-1**, the crack shows a transient opening. If only Mode I loading, the crack width increases with time and reaches a stable state at long time as in Figure II-12. At short time, the crack opens as the crack in an elastic material with a Poisson's ratio the same value as the undrained Poisson's ratio in Figure II-13. At long time, it evolves to the drained stage with the opening as the crack in an elastic material with a Poisson's ration the same value as the drained Poisson's ratio in Figure II-13. If only Mode II loading, the crack closes with time (Figure II-14) as the fluid flows from the crack into the adjacent formation. The crack closure approaches its maximum values at infinite time when the pore pressure around the crack approaches the fluid pressure in the crack. Figure II-15 shows the fracture closing at 1.91×10^5 hours, which is smaller than the opening induced by Mode I loading. The crack still opens with the fluid injection with a constant pressure modeled by combining Mode I and Mode II loading. The crack has an instant opening, and then the width reduces with time. But the crack is still open at long time (Figure II-16). The crack shows the same opening as the analytical solution for the undrained case (Figure

II-17). But crack width reduces with time due to Mode II loading, and approaches a smaller opening at long time instead of approaching the analytical solution for drained stage (Figure II-17).

Table II-1. Parameters in the modeling of pressurized crack.

Shear modulus G (psi)	8.6×10^{5}
Possoin's ratio υ	0.16
Undrained Possoin's ratio υ_u	0.31
Matrix permeability (md)	0.8
Matrix porosity ϕ	0.2
Biot's coefficient α	0.83
Fluid viscosity μ (cp)	1
Fluid compressibility (/psi)	2.9×10^{-6}

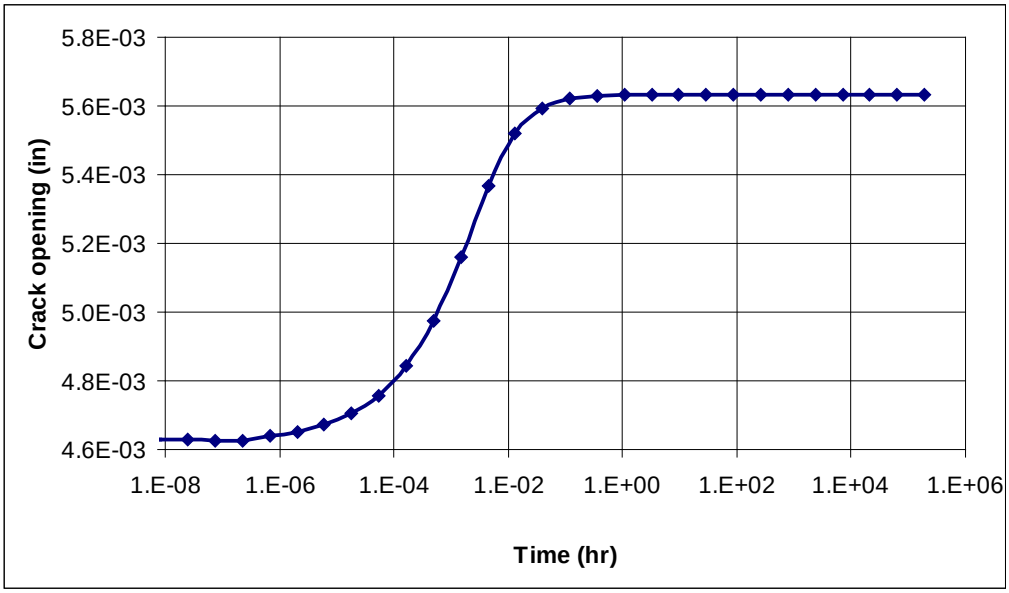

Figure II-12. Mode I loading: the crack opens as a function of time at x=0.2 in.

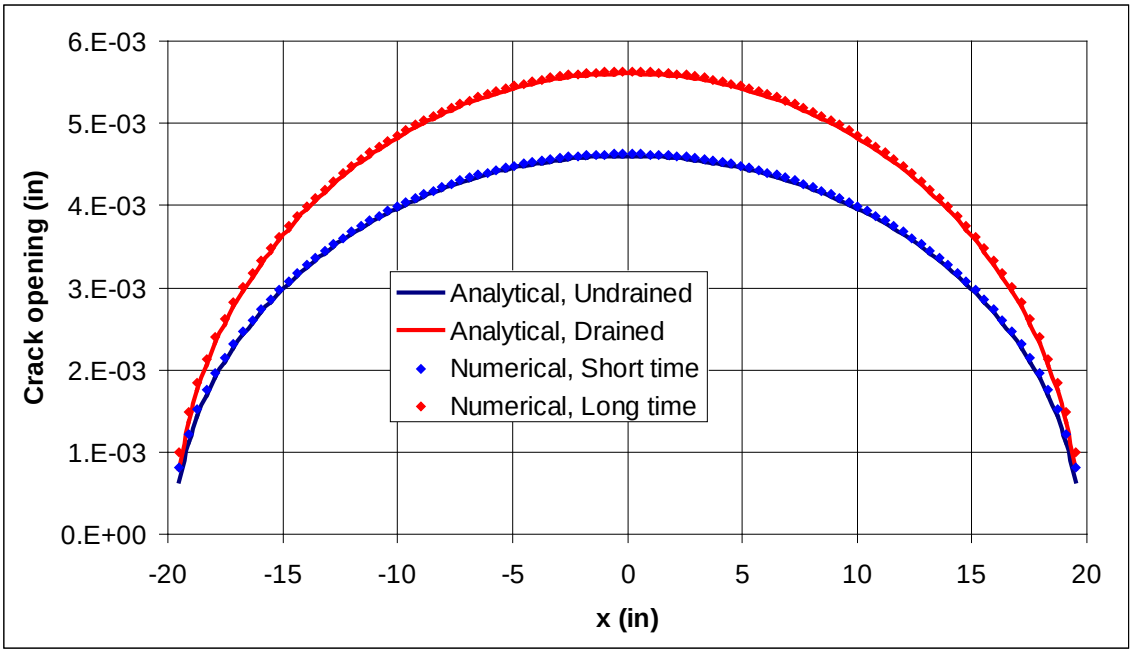

Figure II-13. Comparison of the modeled crack openings at short time and long time with the analytical solutions for Mode I loading.

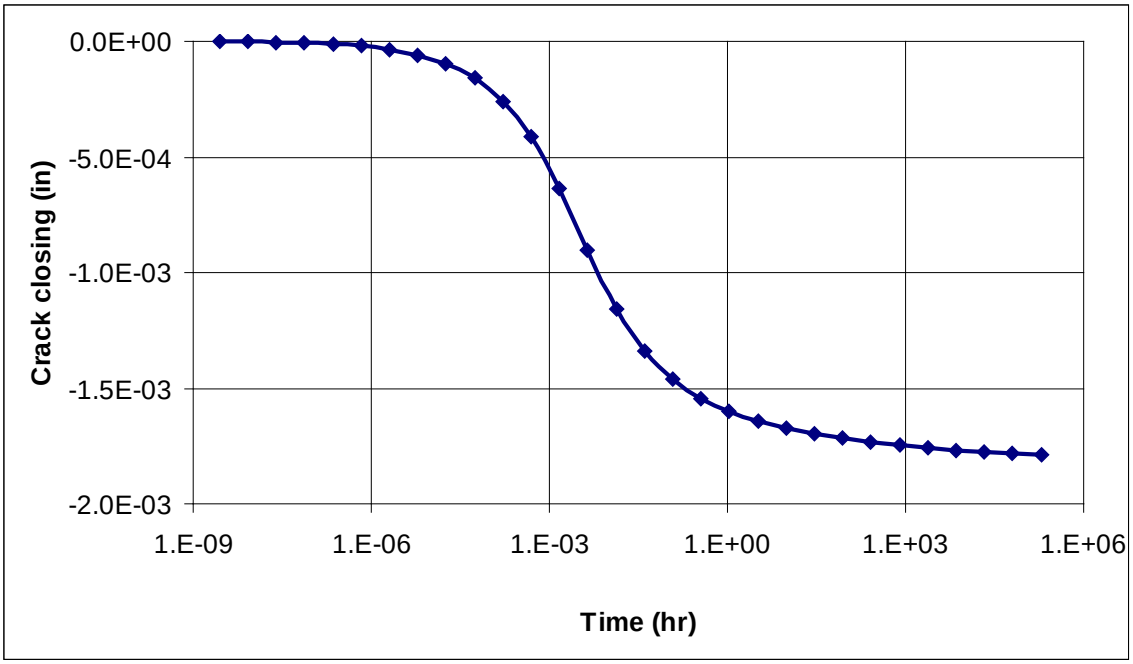

Figure II-14. Mode II loading: the crack closes as a function of time at x=0.2 in.

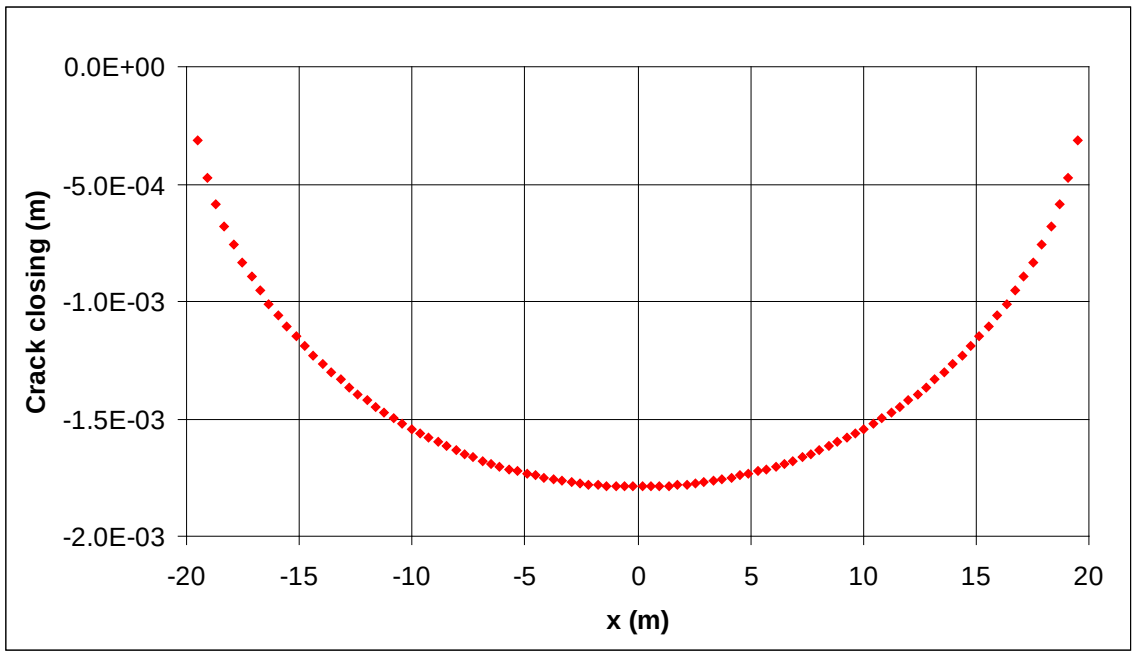

Figure II-15. The crack closing at t=1.91×105 hrs for Mode II loading.

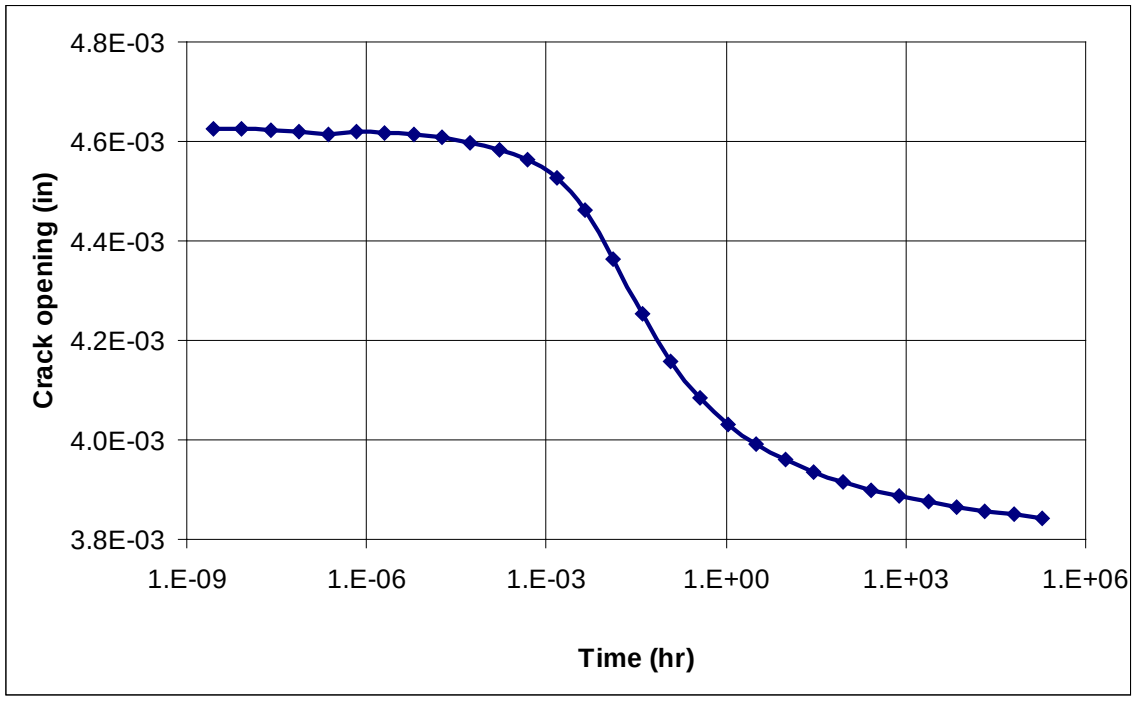

Figure II-16. The crack width for Mode I +II loading at x=0.2 in.

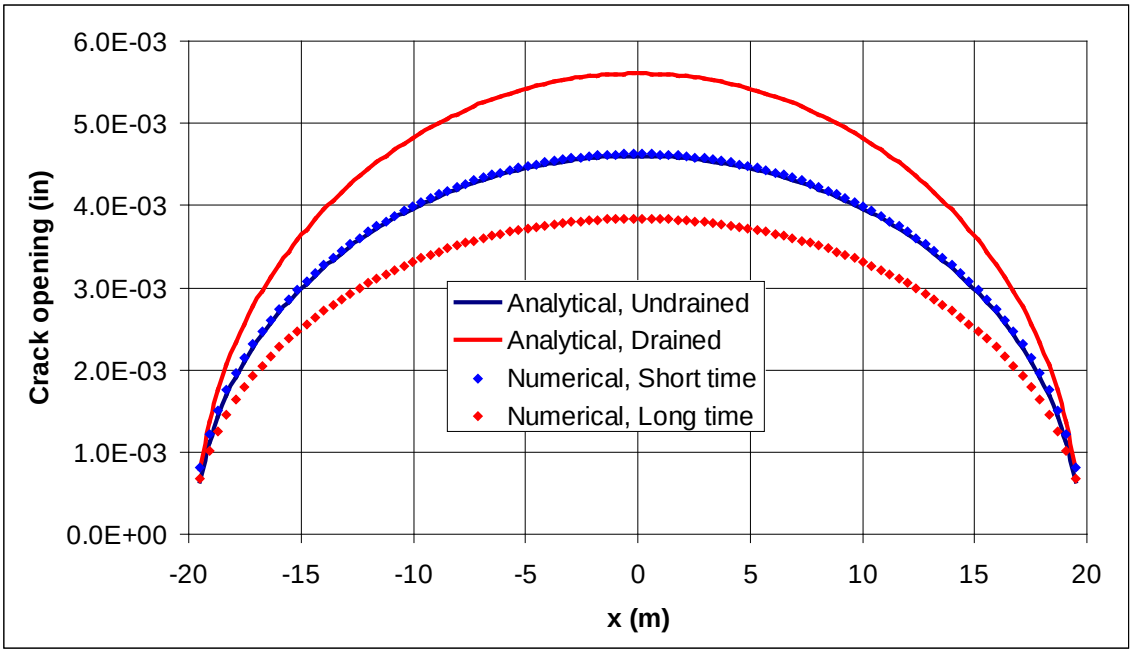

Figure II-17. Comparison of the modeled crack openings at short time and long time with the analytical solutions for Mode I+II loading.

2.4 Chapter conclusions

This chapter described the DDM including elastic DDM for nonporous media and fully coupled poroelastic DDM for porous media saturated with a compressible single-phase fluid. The fully coupled DDM is based on Biot's theory of poroelasticity. For an infinite elastic porous medium containing fractures, if the change of stress and pore pressure in these fractures are known, the fracture aperture change can be determined by using the fully coupled DDM. In real situations, neither the change of stress in fracture nor fracture aperture change is known in the reservoir. But many investigations have shown that there is a relation between the stress change and the fracture aperture change in fractures. Chapter III will give the surface characteristics of fractures with rough surfaces and the relation of stress and fracture deformation. The pore pressure change in the fractures is not known directly either. Usually only the flow rate or fluid pressure in the well is known while producing from a fractured reservoir, the required fluid pressure change in fractures is determined using a numerical finite difference method (FDM) described in Chapter IV. Finally the fracture aperture change due to production can be determined by combining the DDM, the constitutive model of fracture deformation and an FDM to determine the fluid pressure change in fractures.

CHAPTER III

NONLINEAR DEFORMATION OF A SINGLE ROUGH FRACTURE UNDER STRESS

The fracture is also termed a joint in geology publications. In this dissertation both fracture and joint describe two contacting rough surfaces with voids that are completely connected in three-dimensional space. The rough fracture under stress will deform with the change of stress. There are three types of deformation – normal deformation, shear deformation and dilation. The deformation for a single rough fracture has been studied by testing the stress–displacement relationship of natural or artificially fractures in laboratories (Goodman, 1976, Bandis et al., 1981, Bandis et al., 1983, Sun et al., 1985, Boulon et al., 1993, Huang et al., 2002, Lee and Cho, 2002). The constitutive model (Barton-Bandis model) for fracture deformation was presented based on the experimental results by Bandis et al. (1983) and Barton et al. (1985). The empirical model only needs some basic fracture characteristic parameters, e.g. the joint roughness coefficient (JRC), the joint compressive strength (JCS) etc., which can be measured in laboratory. The fracture deformation usually causes the fracture opening or closure, and changes the fracture aperture. The “cubic law” which is derived from the fluid flow between two smooth plates is also applicable to calculate the hydraulic conductivity or permeability for closed rough fractures with a correction coefficient (Witherspoon et al., 1980). Barton et al. (1985) presented a method to correlate the effective hydraulic aperture to the average mechanical aperture and the “cubic law” is

applicable using the correlated effective hydraulic aperture. Consequently, the fracture permeability change caused by stress change also can be derived and analyzed.

The chapter will start with the fracture surface characteristics in Section 3.1. Then Section 3.2 will give the relation between normal stress and normal deformation. Section 3.3 will show the mechanism of shear deformation and dilation, and also the relation between shear stress and shear displacement. Section 3.4 will give the definitions for the effective hydraulic aperture and the average mechanical aperture, and how they are related to permeability. Finally, the conclusions of this chapter will be given in section 3.5.

3.1 Surface characteristics of a fracture

The fracture deformation depends on the fracture surface characteristics. The constitutive models need values for surface characteristics, such as JRC, JCS, unconfined compression strength (rock adjacent to the wall) (σ_c), residual friction angle (ϕ_r), etc. JRC, JCS and ϕ_r are three key parameters in the Barton-Bandis joint model. Barton and Choubey (1977), and Barton (1982) developed methods to quantify these parameters for fractures.

3.1.1 Joint compressive strength (JCS)

The measurement of JCS is fundamentally important because it is largely the thin layers of rock adjacent to joint walls that control the strength and deformation properties of the rock mass as a whole (Barton and Choubey, 1977). Usually for natural fractures,

JCS is much smaller than the strength of intact rock as the fracture surface is weakened by weathering (e.g. mechanical disintegration, chemical decomposition). JCS can be measured by Schmidt Hammer Index test (Barton and Choubey, 1977). Typical JCS values are listed in Table III-1.

Table III-1. Typical JCS values (ISRM, 1978).

Grade	Description	Field identification	JCS (MPa)
S1	Very soft clay	Easily penetrated several inches by fist	<0.025
S2	Soft clay	Easily penetrated several inches by thumb	0.025-0.05
S3	Firm clay	Can be penetrated several inches by thumb with moderate effort	0.05-0.10
S4	Stiff clay	Readily indented by thumb but penetrated only with great effort	0.10-0.25
S5	Very stiff clay	Readily indented by thumbnail	0.25-0.50
S6	Hard clay	Indented with difficulty by thumbnail	>0.50
R0	Extremely weak rock	Indented by thumbnail	0.25-1.0
R1	Very weak rock	Crumbles under firm blows with point of geological hammer, can be peeled by a pocket knife	1.0-5.0
R2	Weak rock	Can be peeled by a pocket knife with difficulty, shallow indentations made by firm blow with point of Geological hammer	5.0-25
R3	Medium strong	Cannot be scraped or peeled rock with a pocket knife, specimen can be fractured with single firm blow of geological hammer	25-50
R4	Strong rock	Specimen requires more than one blow of geological hammer to fracture it	50-100
R5	Very strong rock	Specimen requires many blows of geological hammer to fracture	100-250
R6	Extremely strong rock	Specimen can only be chipped with geological hammer	>250

Note: Grades S1 to S6 apply to cohesive soils, for example clays, silty clays, and combinations of silts and clays with sand, generally slow draining. Discontinuity wall strength will generally be characterized by grades R0-R6 (rock) while S1-S6 (day) will generally apply to filled discontinuities.

3.1.2 Basic friction angle (ϕ_b) and residual friction angle (ϕ_r)

ϕ_b is the friction angle for unweathered fracture and ϕ_r is for weathered fracture angle. The friction angle is defined as arctan (τ_{peak}/σ_n), where τ_{peak} is the shear stress required to initiate the fracture to slide under a normal stress σ_n. The friction angle between two rough surfaces (unweathered or weathered) can be measured by the tilt test shown in Figure III-1. The sample is tilted till the upper surface starts to slide. The angle between the initial sliding surface and the horizontal surface is the friction angle. The friction angle is an important parameter to predict the shear strength, thereby predicting the shear displacement, shear dilation, etc. Friction angle values for most unweathered rocks lie between 25° to 35° and are listed in Table III-2 (Barton and Choubey, 1977). Under a high level of normal stress the rock beneath the weathered surface comes into effect and the residual friction angle ϕ_r approaches the basic friction angle ϕ_b. However, under a low level of normal stress the residual friction angle ϕ_r is much lower than the basic friction angle ϕ_b.

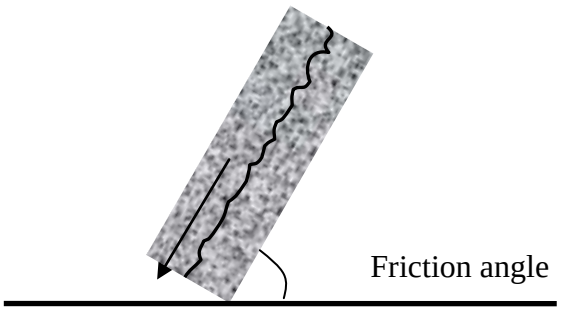

Figure III-1. Tilt test on fractured sample.

Table III-2. Basic friction angles of various unweathered rocks obtained from flat and residual surfaces (Barton and Choubey, 1977).

	Rock type	Moisture condition	Basic friction angle	Reference*
Sedimentary Rocks	Sandstone	Dry	26--35	Patton, 1966
	Sandstone	Wet	25--33	Patton, 1966
	Sandstone	Wet	29	Ripley & Lee, 1962
	Sandstone	Dry	31--33	Krsmanovid, 1967
	Sandstone	Dry	32--34	Coulson, 1972
	Sandstone	Wet	31--34	Coulson, 1972
	Sandstone	Wet	33	Richards, 1975
	Shale	Wet	27	Ripley & Lee, 1962
	Siltstone	Wet	31	Ripley & Lee, 1962
	Siltstone	Dry	31--33	Coulson, 1972
	Siltstone	Wet	27--31	Coulson, 1972
	Conglomerate	Dry	35	Krsmanovid, 1967
	Chalk	Wet	30	Hutchinson, 1972
	Limestone	Dry	31--37	Coulson, 1972
	Limestone	Wet	27--35	Coulson, 1972
Igneous Rocks	Basalt	Dry	35--38	Coulson, 1972
	Basalt	Wet	31--36	Coulson, 1972
	Fine-grained granite	Dry	31--35	Coulson, 1972
	Fine-grained granite	Wet	29--31	Coulson, 1972
	Coarse-grained granite	Dry	31--35	Coulson, 1972
	Coarse-grained granite	Wet	31--33	Coulson, 1972
	Porphyry	Dry	31	Barton, 1971b
	Porphyry	Wet	31	Barton, 1971b
	Dolerite	Dry	36	Richards, 1975
	Dolerite	Wet	32	Richards, 1975
Metamorphic Rocks	Amphibolite	Dry	32	Wallace et al., 1970
	Gneiss	Dry	26--29	Coulson, 1972
	Gneiss	Wet	23--26	Coulson, 1972
	Slate	Dry	25--30	Barton, 1971b
	Slate	Dry	30	Richards, 1975
	Slate	Wet	21	Richards, 1975

* Refer to Barton and Choubey (1977) for specific references.

3.1.3 Joint roughness coefficient (JRC)

In general the joint surface roughness can be characterized by waviness (large scale undulations which, if interlocked and in contact, cause dilation during shear displacement since they are too large to be sheared off) and by unevenness (small scale roughness that tends to be damaged during shear displacement unless the discontinuity wails are of high strength or the stress levels are low, so that dilation can also occur on these small scale features) (IRSM, 1978). Barton and Choubey presented a method to describe the JRC and also presented a formula (Eq.3-1) to calculate the peak shear strength τ_{peak} according to the JRC index.

$$\tau_{peak} = \sigma_n^{'} \tan\left[JRC \log_{10}\left(\frac{JCS}{\sigma_n^{'}} \right) + \phi_r \right] \qquad (3\text{-}1)$$

where σ_n' is the effective normal stress and ϕ_r is the friction angle for weathered fracture. The JRC index can be measured by a tilt test or estimated by comparing with the profiles measured on other joints shown in Figure III-2 (Barton and Choubey, 1977).

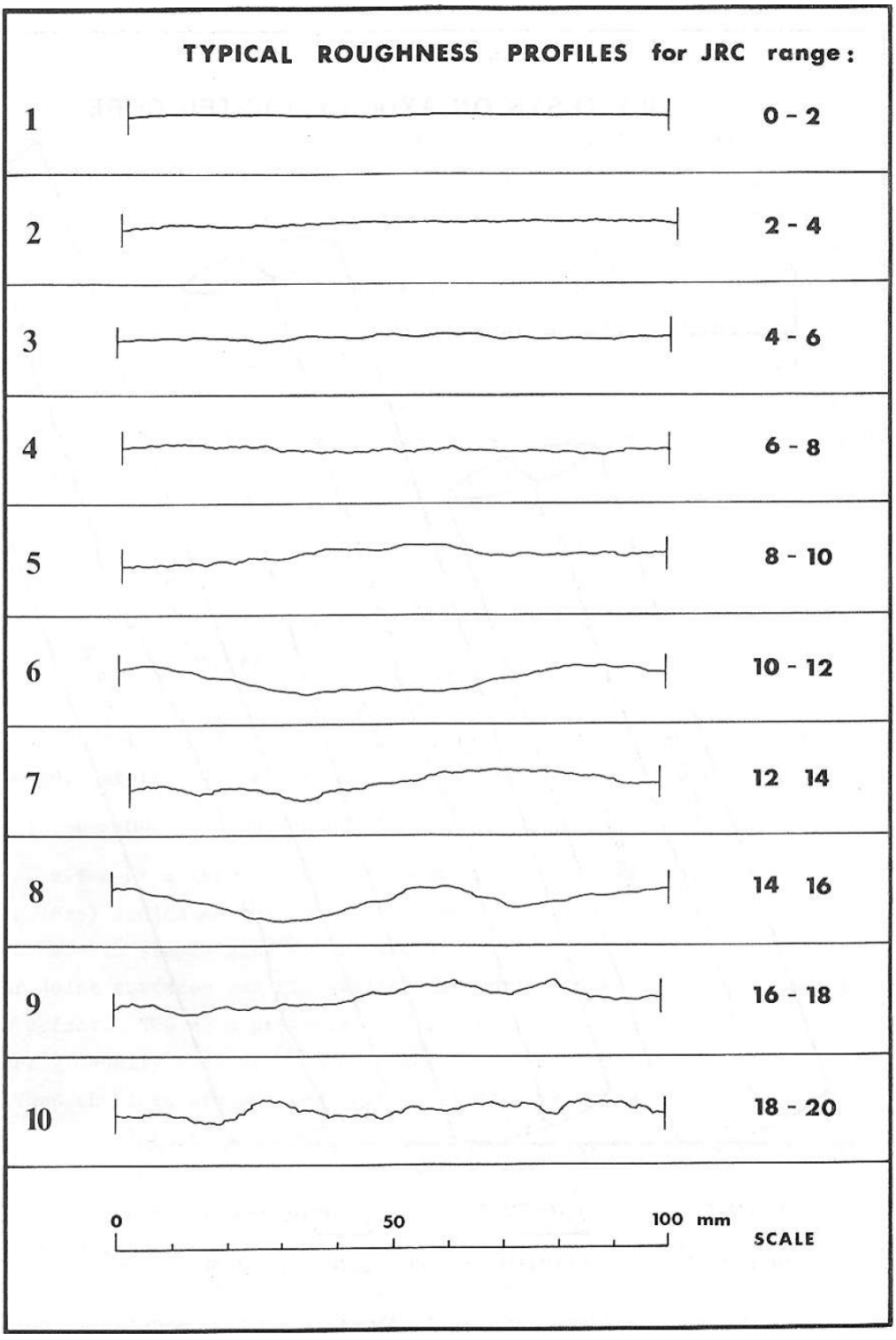

Figure III-2. Typical JRC values for joint samples of different roughness (Barton and Choubey, 1977).

3.2 Normal deformation

The two rough surfaces of a fracture are weaker and more deformable than intact rock. The normal deformation of the two rough surfaces in response to the normal stress change across the fracture or fluid pressure change in the void space of the fracture has a direct important influence on the fracture aperture and fracture permeability. The normal deformation of a fracture can be characterized by the relationship between the effective stress across the fracture and the fracture closure (the change of the average aperture of the fracture).

Goodman (1976) measured the fracture closure as a function of normal stress on artificially induced tensile fractures in rock cores. He measured the axial displacement of an intact rock core under axial stress and axial displacement of a rock core of the same size and an artificially induced tensile fracture perpendicular to the axis under the same axial stress. The difference of the two displacements is the fracture closure. Fracture closure measurements were made for both mated fractures, for which the two surfaces of fracture were placed the same relative positions that they occupied before fracturing the core, and non-mated fractures, for which the two surfaces of fracture were rotated from their original positions relative to one another (Figure III-3). The stress-closure curves show high non-linearity, and the non-mated fracture has greater closure.

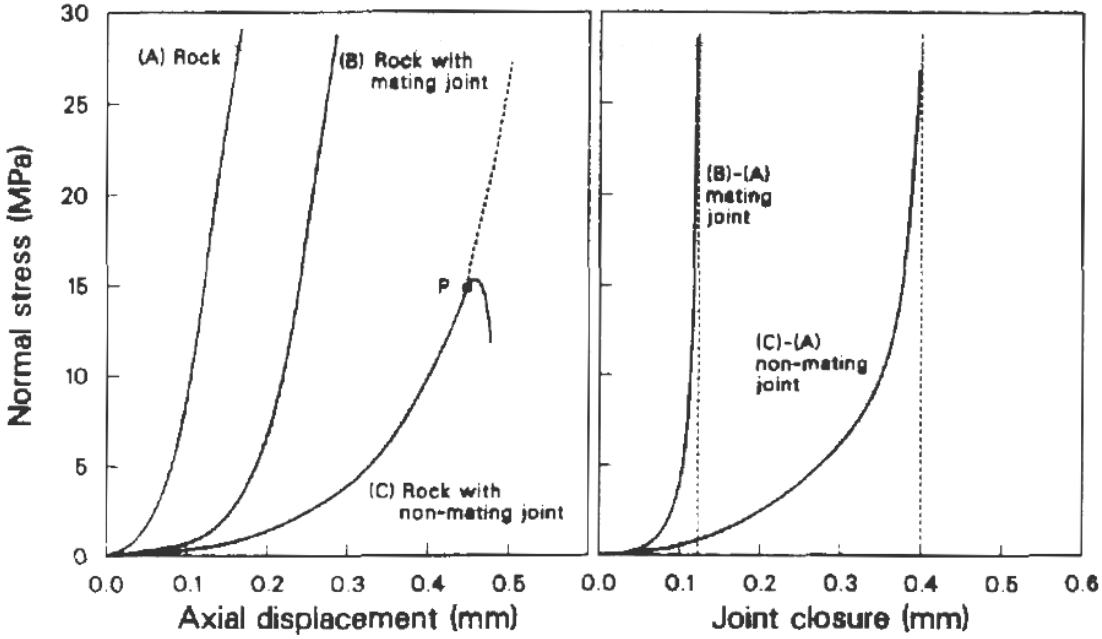

Figure III-3. Measurements of the closure under normal stress of an artificially-induced tensile fracture in a rock core (Goodman, 1976).

Bandis et al. (1983) have measured closure curves for a fracture under normal stress for a variety of natural and unfilled fractures with different degrees of weathering and roughness in slate, dolerite, limestone, siltstone and sandstone (Figure III-4 and Figure III-5). They used the same method as Goodman used to determine fracture closure for natural fractures. As expected, the fracture closures for weathered fractures (Figure III-5) were much greater than for fresh fractures (Figure III-4) under the same stress condition. With the increase of normal stress (σ_n), the stress–closure curves became gradually steeper and developed into virtually straight lines where the fractures have reached their fully closed state. There was permanent deformation observed during the loading–unloading cycle. Therefore the deformation characteristics of fractures also depend on the stress history of the fractures.

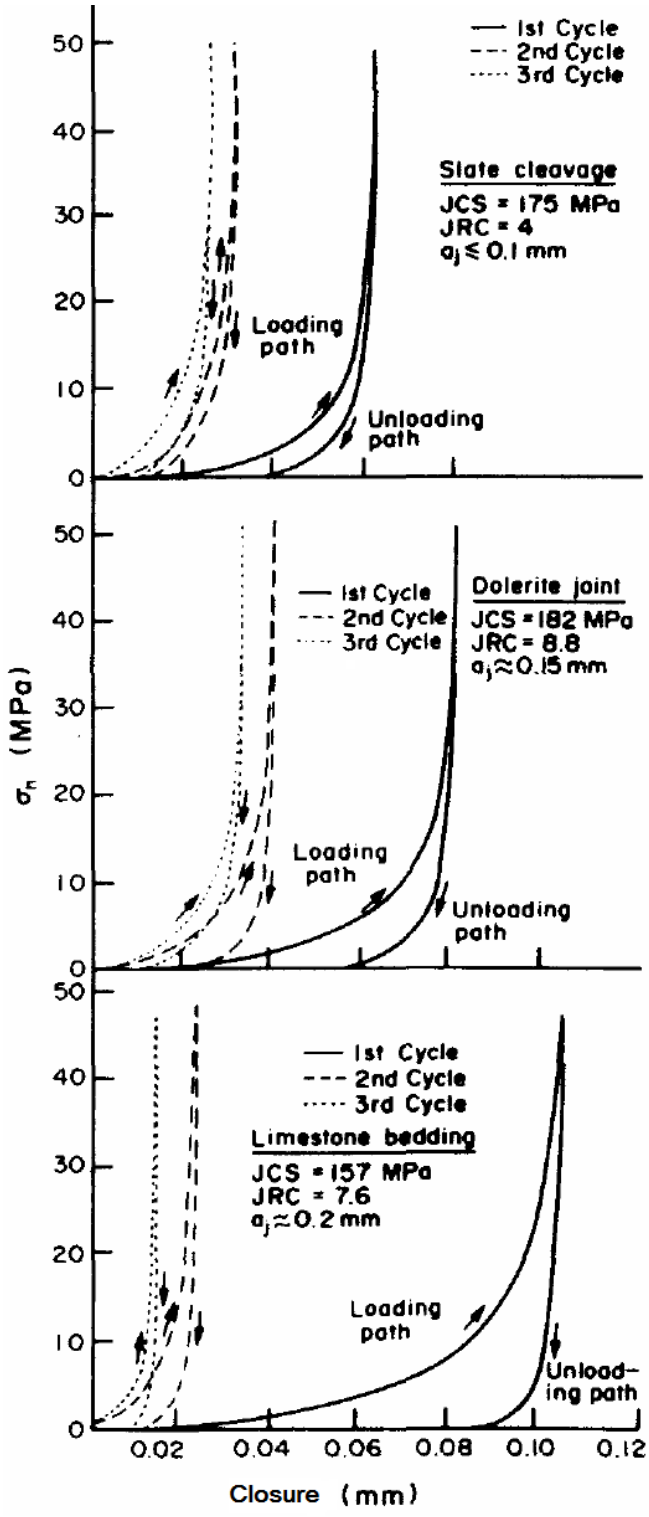

Figure III-4. Normal stress (σ_n) vs closure curves for a range of fresh fractures in different rock types, under repeated loading cycles (Bandis et al., 1983).

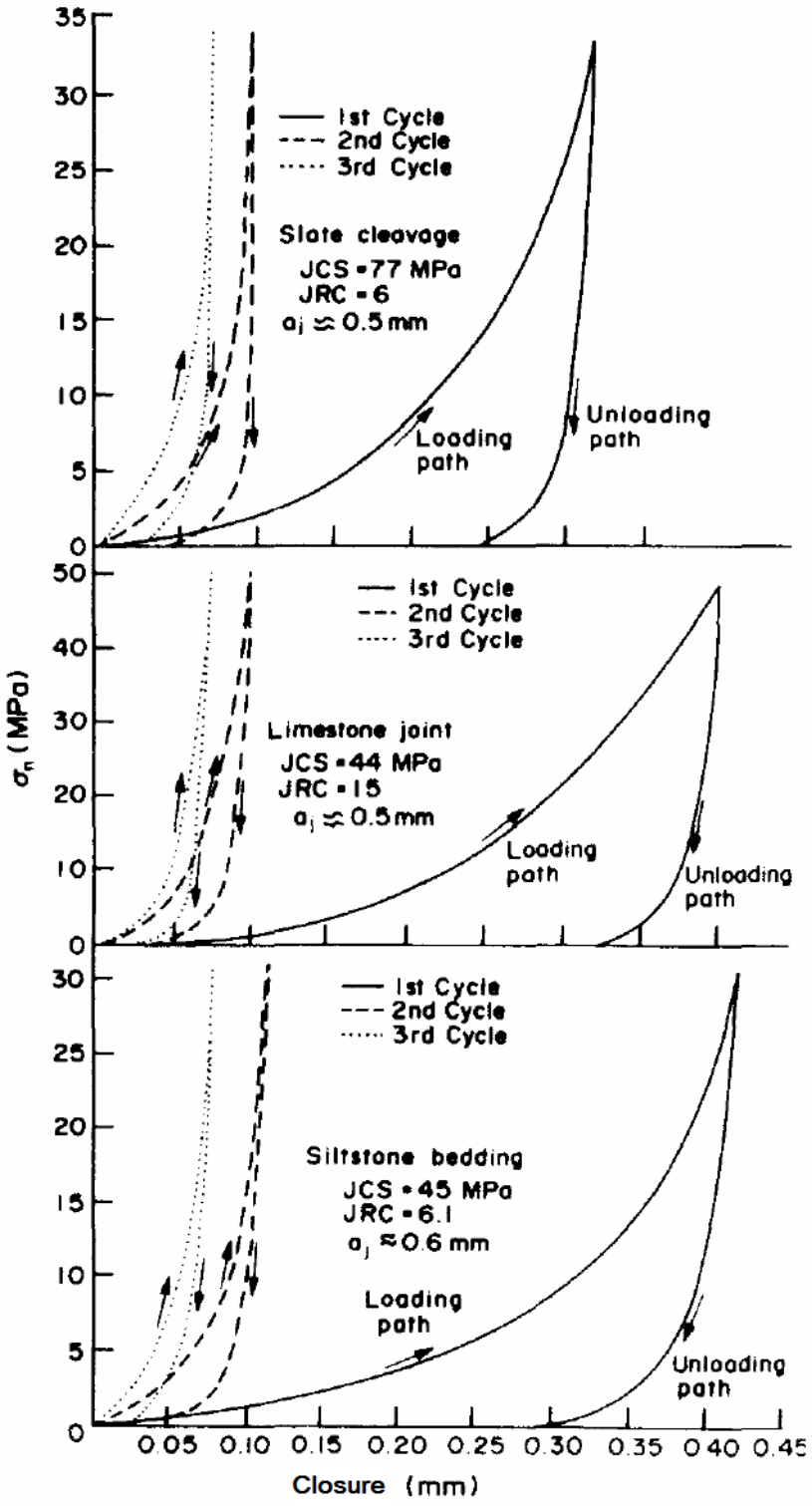

Figure III-5. Normal stress (σ_n) vs closure curves for a range of weathered fractures in different rock types under repeated loading cycles (Bandis et al., 1983).

Based on the experimental results Bandis et al. (1983) presented a hyperbolic function (Eq. (3-2)) to represent the normal stress–closure relationship.

$$\sigma_n = \frac{D_n}{aa - b D_n} \tag{3-2}$$

where D_n is the fracture closure, *aa* and *b* are constants. Eq. (3-2) was rearranged into a linear form:

$$\frac{D_n}{\sigma_n} = aa - bD_n \tag{3-3}$$

aa and *b* can be obtained by using Eq. (3-3) to fit the measured normal stress–closure data, and Figure III-6) shows that Eq.(3-3) fits well with measured data. When σ_n approaches infinity, the fracture closure approaches the maximum fracture closure D_{nmax} and D_{nmax} is equal to *aa/b* according to Eq. (3-3). For extremely small normal stress ($\sigma_n \rightarrow 0$), the fracture closure will be small ($D_n \rightarrow 0$), and hence the initial normal fracture stiffness for $\sigma_n \rightarrow 0$ is defined:

$$K_{ni} = \frac{\sigma_n}{D_n}\Big|_{\sigma_n \rightarrow 0} = \frac{1}{aa} \tag{3-4}$$

Therefore Eq. (3-2) can be rewritten by substituting the two parameters initial normal fracture stiffness (K_{ni}) and maximum fracture closure (D_{nmax}) for *aa* and *b*:

$$\sigma_n = \frac{K_{ni} D_n}{1 - D_n / D_{n\max}} \tag{3-5}$$

The normal stiffness (K_n) is then derived from Eq. (3-5) as a function of D_n or σ_n:

$$K_n = \frac{\partial \sigma_n}{\partial D_n} = \frac{K_{ni}}{\left(1 - D_n / D_{n\max}\right)^2} \tag{3-6}$$

or

$$K_n = \frac{\partial \sigma_n}{\partial D_n} = \frac{K_{ni}}{\left[1 - \sigma_n / \left(K_{ni} D_{n\max} + \sigma_n\right)\right]^2} \tag{3-7}$$

Bandis et al. (1983) also derived the empirical formulae for D_{nmax} (Eq. (3-8)) and K_{ni} (Eq. (3-9)) in terms of JCS, JRC index and average fracture aperture (w_f):

$$D_{n\max} = A1 + B1(JRC) + C1\left(\frac{JCS}{w_f}\right)^D \tag{3-8}$$

$$K_{ni} = A2 + B2(JRC) + C2\ \frac{JCS}{w_f} \tag{3-9}$$

where A1, A2, B1, B2, C1, C2 and D are coefficients determined by fitting experimental data.

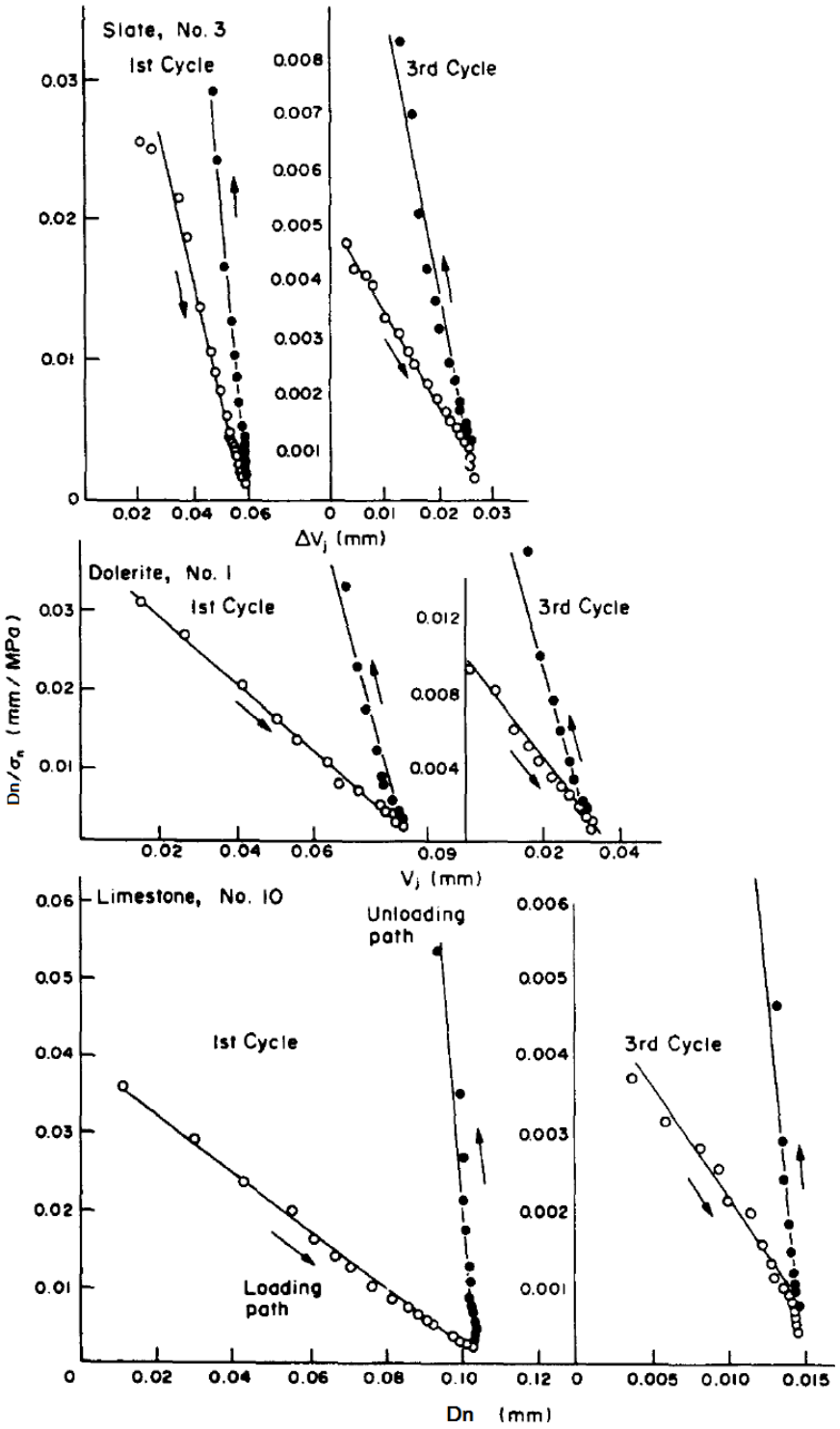

Figure III-6. Linear plots of D_n/σ_n vs D_n for different fracture types, indicating good hyperbolic fit irrespective of the stress history and the loading mode (Bandis et al. 1983).

3.3 Shear deformation and dilation

For a fracture under normal stress loading, the fracture will have a shear deformation if the shear stress (τ) is less than the peak shear strength (τ_{peak}) and become instable and have a fast movement if τ exceeds τ_{peak}. However, for rough surfaces, the shear dilation caused by shear displacement may prevent the instability. The typical shear stress–shear displacement curves have three stages, pre-peak, peak, and post-peak (Figure III-7).

The peak shear strength is a critical parameter to predict the stability of fractures, faults or the initiation of nonlinear movement under anisotropic stress condition. Barton (1976) presented a formula (Eq. (3-1)) to predict the peak shear strength τ_{peak} according to the effective normal stress, the fracture surface roughness JRC, compression wall strength JCS and residual friction angle ϕ_r based on large body of laboratory measured results under low effective normal stress (σ_n'<10MPa). But the peak shear strength at high effective normal stress is independent of JRC, JCS, ϕ_r and even the rock type, and is only dependent on the effective normal stress. Byerlee (1978) developed empirical formulae (Eqs. (3-10) and (3-11)) based on large body of experimental data on rocks including sandstone, limestone, granite, gabbro, etc.

$$\tau_{peak} = 0.85\sigma_n^{'} \qquad \sigma_n^{'} < 200MPa \tag{3-10}$$

$$\tau_{peak} = 50 + 0.6\sigma_n^{'} \qquad 200MPa < \sigma_n^{'} < 2000MPa \tag{3-11}$$

According to the shear stress–shear displacement curves (Figure III-7), the pre-peak curve can be approximated as a line. The slope of the line is the pre-peak shear stiffness K_s:

$$K_s = \frac{\tau_{peak}}{D_{s-peak}} \tag{3-12}$$

where $D_{s\text{-}peak}$ is the shear displacement when the shear stress reaches the peak value. The post-peak curve is very complicated and is often treated as a zero slope line, and the shear stiffness K_s is assumed as zero.

When shearing of two rough surfaces occurs, the opposed asperities slide over each other and cause an increase in aperture. The increase of fracture aperture induced by shear deformation was well investigated in laboratory by Bandis et al. (1981). Figure III-8a shows the shear stress–displacement curves for different block size and Figure III-8b shows the corresponding aperture increase induced by the shear displacement at constant normal stresses. The dashed lines show the dilation angle, which is defined as:

$$\phi_d = \tan^{-1}\left(\frac{D_n}{D_s}\right) \tag{3-13}$$

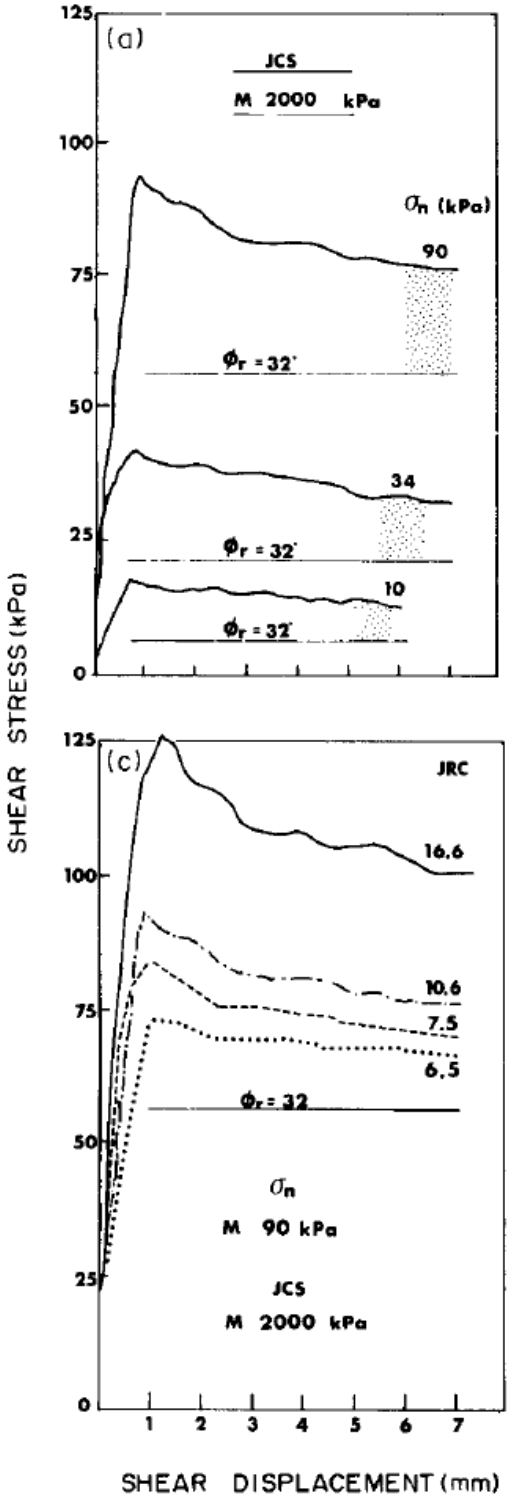

Figure III-7. Shear stress – shear displacement for joints with different normal stress and JRC (Barton et al., 1985).

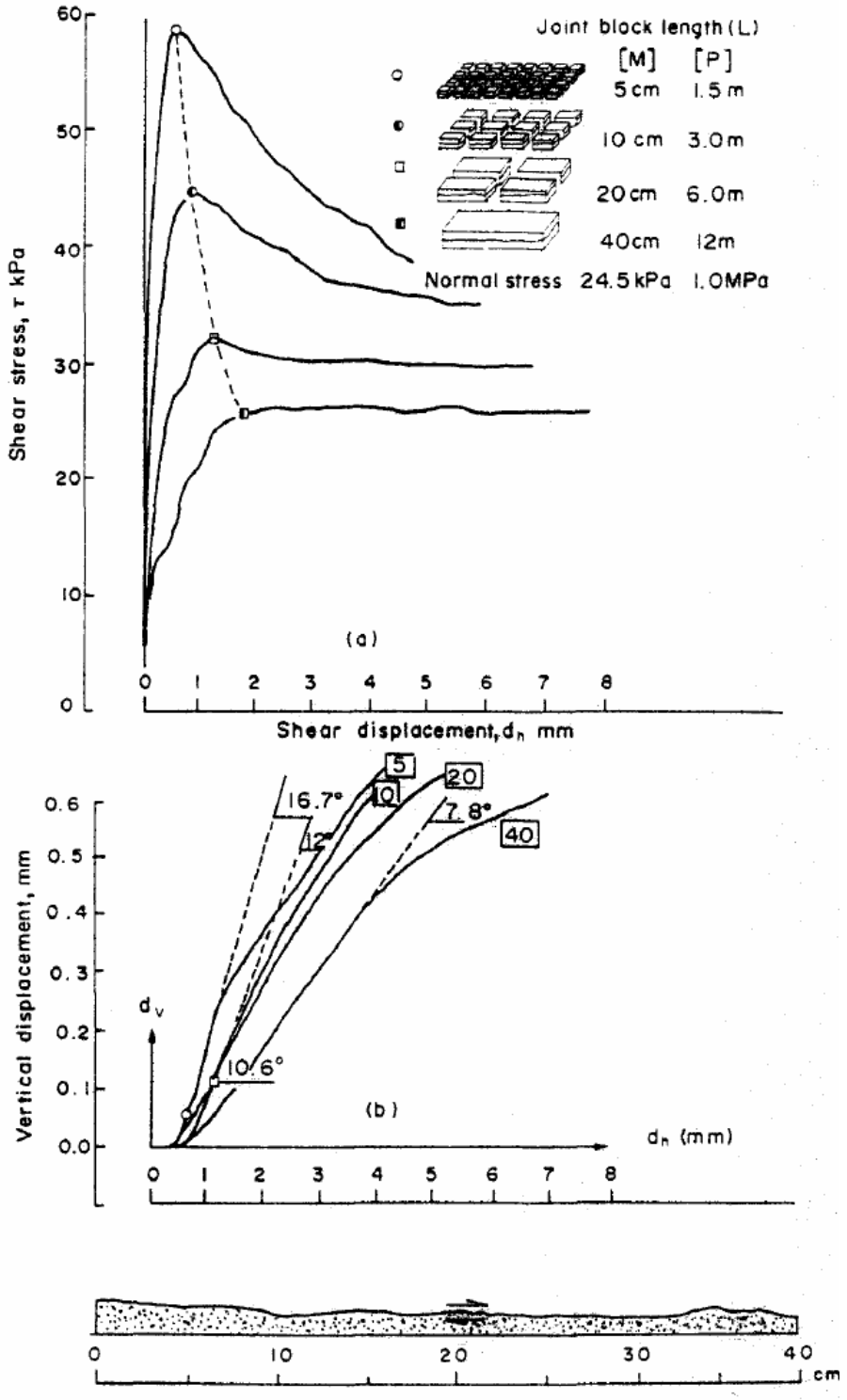

Figure III-8. Cumulative mean shear stress---shear displacement (a) and dilation (b) curves (Bandis et al., 1981).

3.4 Fracture aperture and permeability

Fracture aperture is the perpendicular distance between adjacent rock walls of a fracture. The fracture deformation will change the fracture aperture, thereby changing the fracture permeability. The relation of permeability and aperture for laminar flow through a pair of smooth parallel plates has been investigated and the cubic law was derived (Snow, 1965; Iwai, 1976). The flow rate through the fracture (Figure III-9) is:

$$q = -\frac{w_f^3}{12\mu}\frac{dp}{dx} \tag{3-14}$$

Compared with Darcy's law, the fracture permeability is:

$$k_f = \frac{w_f^2}{12} \tag{3-15}$$

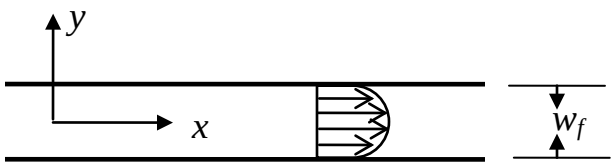

Figure III-9. Laminar flow through a pair of smooth parallel plates.

The natural fracture is not completely open, and the surfaces are not smooth. Therefore, Eq. (3-15) cannot be applied to the natural fracture directly. However, Witherspoon et al. (1980) found that the cubic law was still valid for partially closed fractures by laboratory investigations. The investigated fracture aperture ranges from 4μm to 250μm and the rock types include basalt, granite and marble. The fracture

conductivity still has a cubic relation with the average fracture aperture. But Eq. (3-15) requires a correction coefficient *f* to be valid for partially closed fracture.

$$k_f = \frac{w_f^2}{12\, f} \tag{3-16}$$

The correction coefficient in their investigation varied from 1.04 to 1.65.

Barton et al. (1985) argued that Witherspoon et al. (1980) did not measure the real mechanical aperture, and that the aperture they used was an approximate hydraulic aperture. Barton et al. (1985) still used Eq. (3-15) to relate fracture permeability to aperture, but substituted effective hydraulic fracture aperture for mechanical aperture. Based on published experimental data (Figure III-10), they developed an empirical formula to relate the hydraulic fracture aperture to mechanical aperture:

$$w_{ef} = \frac{JRC^{2.5}}{\left(w_f / w_{ef}\right)^2} \tag{3-17}$$

The unit of w_{ef} and w_f is μm.

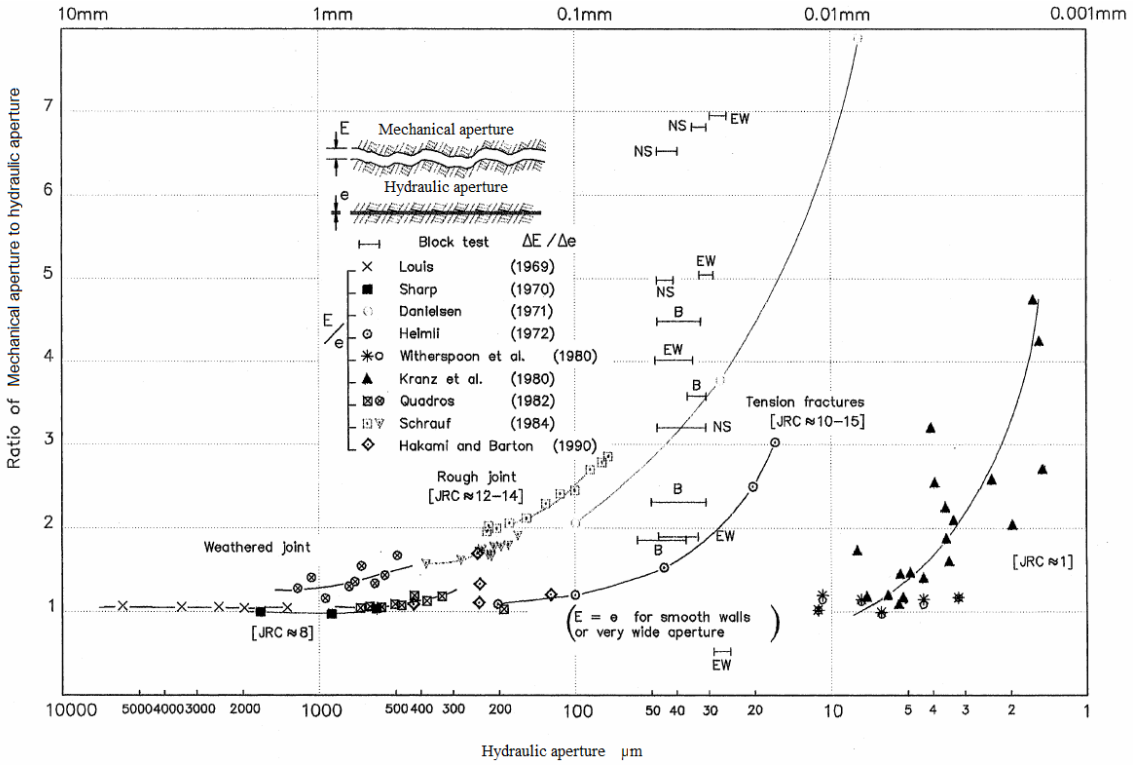

Figure III-10. Comparison of mechanical aperture and hydraulic aperture (Barton et al., 1985; Olson and Barton, 2001).

3.5 Chapter conclusions

This chapter described the characteristics of fracture surfaces, nonlinear Barton-Bandis model of fracture deformation, and the relation of fracture permeability to fracture aperture in rough fractures. In the nonlinear Barton-Bandis model of fracture deformation, the relation of normal stress and fracture closure is represented by a hyperbolic formula. The relation of shear stress and shear displacement is linear before yielding and too complicated to represent using simple functions after yielding. The model also includes shear dilation which is the fracture opening caused by shear

displacement. The peak shear strength can be determined from the effective normal stress, JRC, JCS and friction angle. The fracture permeability has a cubic relation to the effective hydraulic aperture but not the average mechanical aperture. The effective hydraulic aperture is related with the average mechanical aperture using JRC. The next chapter will combine the DDM, the nonlinear Barton-Bandis model of fracture deformation, and an FDM to determine the pore pressure change in fractures and in turn to determine the change of fracture aperture and permeability due to production from a fractured reservoir.

CHAPTER IV

MODELING OF THE FRACTURE APERTURE AND PERMEABILITY CHANGE IN FRACTURED RESERVOIRS

Throughout this study, the fractured reservoir is treated as a fracture network in a porous medium saturated with a compressible single-phase fluid. As in dual porosity models, the fracture network provides the main flow channels and the porous media provides the main storage media. On production, the fluid flows from matrix to fractures, then in fractures to the well. The fluid pressure change induces effective stress change and fracture aperture change, which in turn causes permeability changes in the fractures, the nature of which was addressed in the Chapter III. The fracture permeability change in turn influences fluid flow. Fluid flow in the fracture network is solved using a finite difference method (FDM). The change of effective stress on the fractures induces fracture deformation including normal and shear deformation. The fracture deformation also disturbs the stress distribution in the fracture network. A new numerical method is developed in this chapter to determine the fluid pressure, fracture aperture change and stress change implicitly using an FDM to solve the diffusion equation for fluid flow in fractures, a fully coupled displacement discontinuity method (DDM) to determine the global fracture deformation relation, and the nonlinear Barton-Bandis fracture deformation model to determine the local fracture deformation relation.

This chapter will start with building and discretizing the equation for fluid flow in fracture network in Section 4.1. And then Section 4.2 will describe a method for

combining the global and local relations between stress and displacement to fracture deformation. Section 4.3 will present a new numerical method combining an FDM for the diffusivity equation governing fluid flow in fractures, a fully coupled DDM for determining the global fracture deformations, and a nonlinear fracture deformation model for determining the local fracture deformations. In addition to the fully coupled method, an uncoupled method will be presented that saves computation time in cases where the effect of solid deformation on fluid flow is small. Finally, Section 4.4 will give conclusions of this chapter.

4.1 Fluid flow in the fracture network

The apertures of real fractures vary in space (Figure IV-1) and the fluid flow inside is very complicated due to the rough surfaces. But Witherspoon et al. (1980) verified that Darcy's law is still valid and the rough fracture can be represented by a fracture with an average fracture aperture, as in Figure IV-2. The one dimensional fluid material balance equation in the fracture including flow from the connected fractures and the interface flow from the connected matrices is given by

$$\frac{\partial(\rho_f q_f)}{\partial x} = -\frac{\partial(\rho_f n\, w_f \Delta L)}{\partial t} - \Delta L \rho_f q_{\text{int}} - \rho_f q_s \qquad (4\text{-}1)$$

where ρ_f is the fluid density; q_f is the flow rate in the fracture per unit formation thickness; q_{int} is the interface flow rate per fracture length per unit formation thickness; ΔL (given previously as $2a$ for the well fracture) is the length of fracture segment; q_s is the production rate per unit formation thickness; n is the ratio of actual fracture void

volume (V_f) to the effective fracture void volume for fluid flow (V_{ef}). In Eq. (4-1), the left term, $\frac{\partial(\rho_f q_f)}{\partial x}$, is the net mass flow rate out of the fracture, the first right term, $\frac{\partial(\rho_f n w_f \Delta L)}{\partial t}$, is rate of fluid mass change in the fracture, the second right term, $\Delta L \rho_f q_{\text{int}}$, is the mass flow rate between fracture and the connected matrix, and the third right term, $\rho_f q_s$, is a production term, for example for a producing well. The flow rate in the fracture can be obtained by using Darcy's law:

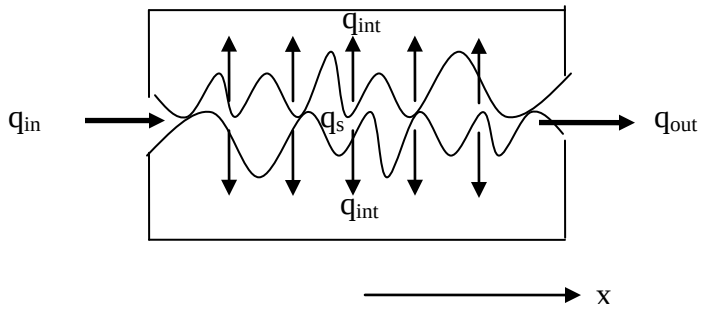

Figure IV-1. Fluid flow through a rough fracture.

$$q_f = -\frac{k_f w_f}{\mu}\frac{\partial p}{\partial x} \tag{4-2}$$

where k_f is the fracture permeability determined from the fracture aperture (3-15). Combining Eqs. (2-23) and (4-2), the net fracture flow rate term becomes:

$$\frac{\partial(\rho_f q_f)}{\partial x} = -\frac{\rho_f k_f w_f}{\mu}\frac{\partial^2 p}{\partial x^2} - \frac{c_o \rho_f k_f w_f}{\mu}\left(\frac{\partial p}{\partial x}\right)^2 \tag{4-3}$$

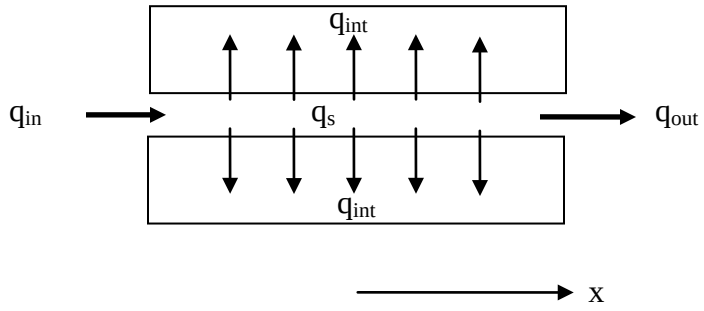

Figure IV-2. Fluid flow through an artificial fracture represented using average fracture aperture.

The second term with squared pressure gradient multiplied by the small compressibility can be neglected (Lee et al., 2003), and the net fracture flow rate is approximated as:

$$\frac{\partial(\rho_f q_f)}{\partial x} = -\frac{\rho_f k_f w_f}{\mu}\frac{\partial^2 p}{\partial x^2} \tag{4-4}$$

The fluid mass change in the fracture includes two parts, one is due to fracture volume change and another one is due to fluid density change. The fracture volume change is mainly from the fracture aperture change:

$$\frac{\partial V_f}{\partial t} = n\,\Delta L\frac{\partial w_f}{\partial t} \tag{4-5}$$

The fracture aperture change can be related with the fracture closure D_n:

$$\frac{\partial w_f}{\partial t} = -\frac{\partial D_n}{\partial t} \tag{4-6}$$

Eq. (4-5) can be rewritten by substituting D_n for w_f:

$$\frac{\partial V_f}{\partial t} = -n\,\Delta L\frac{\partial D_n}{\partial t} \tag{4-7}$$

The fluid mass change due to fluid density change is:

$$\frac{\partial m}{\partial t} = -n\, w_f \Delta L \frac{\partial \rho_f}{\partial t} \tag{4-8}$$

Substituting Eq. (2-23) into Eq. (4-8) yields:

$$\frac{\partial m}{\partial t} = -n\, c_o \rho_f w_f \Delta L \frac{\partial p}{\partial t} \tag{4-9}$$

Combining Eqs. (4-1) – (4-9) yields the pressure diffusion equation:

$$\frac{k_f w_f}{\mu} \frac{\partial^2 p}{\partial x^2} = n\, w_f \Delta L c_o \frac{\partial p}{\partial t} - n\Delta L \frac{\partial D_n}{\partial t} + \Delta L q_{\text{int}} + q_s \tag{4-10}$$

In Eq. (4-10), the left term, $\frac{k_f w_f}{\mu} \frac{\partial^2 p}{\partial x^2}$, is the net flow rate in the fracture, the first right term, $n\, w_f \Delta L c_o \frac{\partial p}{\partial t}$, is the fluid volume change due to fluid compression or expansion (fluid density change), the second right term, $n\Delta L \frac{\partial D_n}{\partial t}$, is the fluid volume change due to fracture deformation, the third right term, $\Delta L q_{\text{int}}$, is the interface flow rate per formation thickness between fracture and the matrix, and the last term, q_s , is the production rate per unit formation thickness.

4.2. Mechanical coupling of fracture deformation

In a fracture network, the change of stress and fracture deformation for any fracture obeys the constitutive relations for fracture deformation. There is a local relation for each fracture or fracture segment between its stress and deformation, and there are global relations for stress and fracture deformation among fractures in the fracture network.

4.2.1 Local relation between stress and displacement to fracture deformation

For any fracture in the fracture network (Figure IV-3), the deformation must comply with the fracture deformation model. The relation between effective normal stress change $\Delta\sigma_n'$ and normal displacement ΔD_n of the *ith* fracture segment is:

$$\Delta \overset{i}{\sigma_n'} = -\overset{i}{K_n}\,\Delta \overset{i}{D_n} \tag{4-11}$$

The normal stiffness K_n is a coefficient which is dependent on the fracture closure (Eq. (3-6)) or stress (Eq. (3-7)). The effective stress (tension is treated as positive) is defined as:

$$\sigma_n' = \sigma_n + \alpha\ p \tag{4-12}$$

where $\alpha = 1 - K_m / K_s$ as before in Chapter II. For a fracture, when the bulk modulus of system K_m is much less than the solid bulk modulus K_s, the Biot coefficient becomes unity, and the effective stress is given by:

$$\sigma_n' = \sigma_n + p \tag{4-13}$$

Substituting Eq. (4-13) for effective stress in Eq. (4-11) yields (for each fracture segment):

$$\Delta \overset{i}{\sigma_n} + \Delta \overset{i}{p} = -K_n\,\Delta \overset{i}{D_n} \tag{4-14}$$

The relation of shear stress change $\Delta\sigma_s$ and shear displacement ΔD_s is:

$$\Delta \overset{i}{\sigma_s} = \overset{i}{K_s}\,\Delta \overset{i}{D_s} \tag{4-15}$$

The shear stiffness is a constant before yielding and reduces to zero after yielding. The normal deformation $\Delta D_{n\text{-}dilation}$ due to shear dilation is:

$$\Delta \overset{i}{D}_{n-dilation} = -\Delta \overset{i}{D}_s \tan \phi_d \tag{4-16}$$

The dilation angle is defined in Eq. (3-13). Eq. (4-14) must be rewritten when the normal deformation induced by shear dilation is considered:

$$\Delta \overset{i}{\sigma}_n + \Delta \overset{i}{p} = -\overset{i}{K}_n \left(\Delta \overset{i}{D}_n + \Delta \overset{i}{D}_s \tan \phi_d \right) \tag{4-17}$$

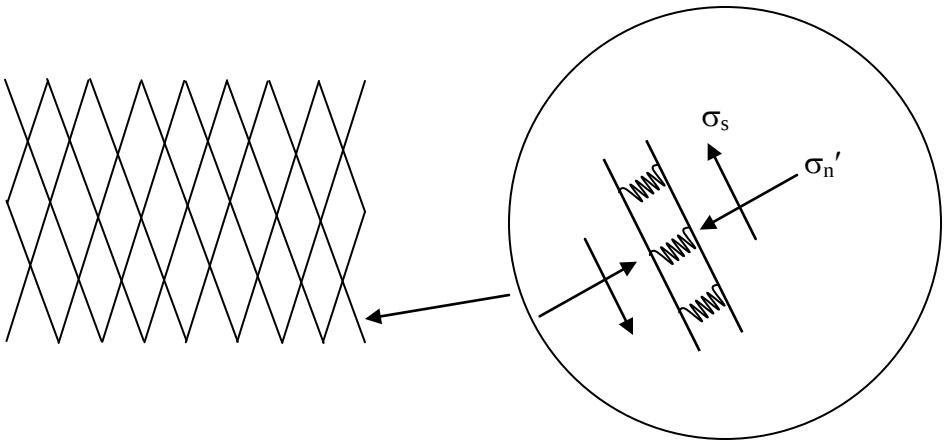

Figure IV-3. Local relation of fracture deformation.

4.2.2 Global relation between stress and displacement to fracture deformation

In the fracture network with *m* fracture segments, there are interactions among fractures. The stress change of the *ith* fracture segment is influenced by the deformation of all the fracture segments in the system. For the elastic DDM (Eq. (2-11)), the change of normal and shear stresses of the *ith* fracture segment is related with the normal and shear deformation of all the fracture segments as:

$$\Delta \overset{i}{\sigma}_n = \sum_{j=1}^{m} \overset{ij}{A} \Delta \overset{j}{D}_n + \sum_{j=1}^{m} \overset{ij}{B} \Delta \overset{j}{D}_s$$
$$\Delta \overset{i}{\sigma}_s = \sum_{j=1}^{m} \overset{ij}{E} \Delta \overset{j}{D}_n + \sum_{j=1}^{m} \overset{ij}{F} \Delta \overset{j}{D}_s \tag{4-18}$$

For the poroelastic DDM, the interface flow rate between fracture and matrix also has an impact on the stress change. Therefore, the change of normal and shear stresses of *ith* fracture segment depends on the interface flow rate in addition to the normal and shear deformation of all fracture segments according to Eq. (2-40).

$$\Delta \overset{i}{\sigma}_n = \sum_{j=1}^{m} \overset{ij}{A} \Delta \overset{j}{D}_n + \sum_{j=1}^{m} \overset{ij}{B} \Delta \overset{j}{D}_s + \sum_{j=1}^{m} \overset{ij}{C} \overset{j}{q}_{\text{int}}$$
$$\Delta \overset{i}{\sigma}_s = \sum_{j=1}^{m} \overset{ij}{E} \Delta \overset{j}{D}_n + \sum_{j=1}^{m} \overset{ij}{F} \Delta \overset{j}{D}_s + \sum_{j=1}^{m} \overset{ij}{K} \overset{j}{q}_{\text{int}} \tag{4-19}$$

The change of fluid pressure of *ith* fracture also depends on the interface flow rate, normal and shear deformation of all fracture segments according to Eq. (2-40).

$$\Delta \overset{i}{p} = \sum_{j=1}^{m} \overset{ij}{L} \Delta \overset{j}{D}_n + \sum_{j=1}^{m} \overset{ij}{H} \Delta \overset{j}{D}_s + \sum_{j=1}^{m} \overset{ij}{N} \overset{j}{q}_{\text{int}} \tag{4-20}$$

4.3 Uncoupled and coupled solution methods

The changes in fracture apertures due to production can be determined by solving the pressure diffusion equation in fracture network, the fracture deformation model for local stress—displacement relations and the DDM for global stress–displacement relations. The result can be determined using an uncoupled method or a coupled solution method. The uncoupled method saves computation time and provides a suitable

approximation when the effect of solid deformation on fluid flow is small. The uncoupled method first solves for the fluid pressure change from the diffusivity equation, and then uses the resulted fluid pressure change as a boundary condition to determine the fracture deformation by combining the constitutive equations for fracture deformation (Eqs.(4-15) and (4-17)) and stress–displacement relations from the elastic DDM (Eq. (4-18)). The coupled method simultaneously obtains the fluid pressure change, interface flow rate, fracture deformation by solving together the diffusivity equation (Eq. (4-10)), constitutive equations for fracture deformation (Eqs. (4-15) and (4-17)), and stress–displacement relations from the poroelastic DDM (Eqs. (4-19) and (4-20)).

4.3.1 Uncoupled method

The change of normal fracture closure is related with the pore pressure change according to Eq. (4-14) by defining a fracture compressibility parameter c_{fr}.

$$\frac{\partial D_n}{\partial t} = -w_f c_{fr} \frac{\partial p}{\partial t} \tag{4-21}$$

Substituting Eq. (4-21) into Eq. (4-10) yields:

$$\frac{k_f w_f}{\mu} \frac{\partial^2 p}{\partial x^2} = c_t n\, w_f \Delta L \frac{\partial p}{\partial t} + \Delta L q_{\text{int}} + q_s \tag{4-22}$$

where $c_t=c_o+c_{fr}$ is the total compressibility. Eq. (4-22) can be discretized for a given fracture network using an implicit finite difference method.

$$\sum_{j=1}^{m} \overset{ij}{C_p}\, \overset{j}{p}^{l+1} = \overset{c}{C_p}\, \overset{i}{p}^{l} - \Delta L\, \overset{i}{q}_{\text{int}} - \overset{i}{q}_s \tag{4-23}$$

where m is total fracture elements, C_p is coefficient matrix, the subscript $l+1$ indicates new time level and the subscript l indicates the old time level, and q_s^i is the production from the *ith* fracture element. The interface flow rate q_{int} is an unknown and can be determined using an iterative method. For every time step, the interface flow rate q_{int} is assumed as zero for the first iteration step. Then Eq. (4-23) can be solved to obtain the fluid pressure distribution in the fracture network. The new fluid pressure in fractures can be taken as the boundary conditions for every matrix element (Figure IV-4) and the fluid flow between the matrix and fractures around it can be obtained by finite difference solution of the uncoupled diffusivity equation (Eq. (4-24)) in the matrix. After the pressure distribution in the matrix is determined, the flow rate at the boundary between the matrix element and surrounding fractures can be obtained from Darcy's law

$$\left(\frac{\partial^2 p}{\partial x^2}+\frac{\partial^2 p}{\partial y^2}\right)=\frac{\phi\mu c_{mt}}{k}\frac{\partial p}{\partial t} \tag{4-24}$$

where c_{mt} is the total compressibility of fluid and matrix. Then interface flow rate q_{int}^{i1} is used to solve Eq. (4-23) in the second iteration. A new interface flow rate q_{int}^{i2} can be obtained as for the second iteration, and this process is repeated until the difference between successive interface flow rate values is smaller than the accuracy needed to the problem. At that point, the iteration terminates and the calculation begins for the next time step. The pressure distribution at the last iteration is taken as the result for that time step.

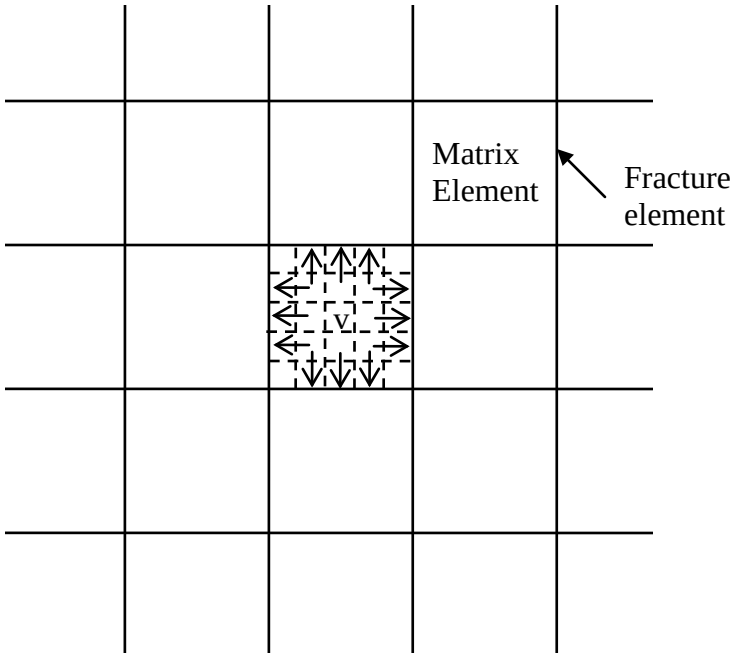

Figure IV-4. Interface flow rate between fracture and matrix.

The effective stress change in a fracture resulting from changes in pore pressure and the total stress is illustrated in Figure IV-5. The effect is that of a set of springs between two plates, and the stress acting on the springs represents the effective stress. The compression effective stress ($-\Delta\sigma_n'$) increases with the decrease of pore pressure (Δp) and the increase of compression total stress ($-\Delta\sigma_n$). After the pressure change, Δp, is solved for every time step, a set of linear equations for effective stress change is obtained by combining Eqs. (4-15), (4-17) and (4-18).

$$\sum_{j=1}^{m} \overset{ij}{A}\Delta \overset{j}{D}_n + \sum_{j=1}^{m} \overset{ij}{B}\Delta \overset{j}{D}_s + \overset{i}{K}_n \Delta \overset{i}{D}_n + \overset{i}{K}_n \tan\phi_d \Delta \overset{i}{D}_s = -\Delta \overset{i}{p}$$

$$\sum_{j=1}^{m} \overset{ij}{E}\Delta \overset{j}{D}_n + \sum_{j=1}^{m} \overset{ij}{F}\Delta \overset{j}{D}_s - \overset{i}{K}_s \Delta \overset{i}{D}_s = 0 \qquad (4\text{-}25)$$

The normal and shear displacement for every time step can be obtained by solving the linear equation (4-25).

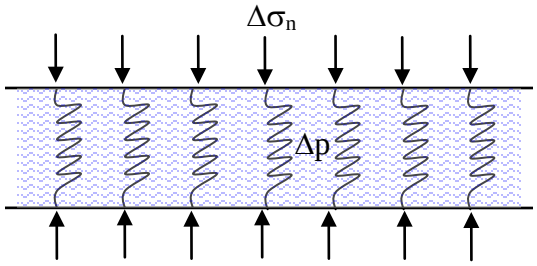

Figure IV-5. Illustration of effective stress change on fracture.

After solving the fracture displacement, the fracture aperture and permeability are updated.

$$\overset{i}{w}_f^{l+1} = \overset{i}{w}_f^{l} - \Delta \overset{i}{D}_n \qquad (4\text{-}26)$$

The fracture aperture at the new time step is determined by subtracting the fracture closure determined from the previous time step. Then the fracture permeability is updated according to Eq. (3-15). If the difference between mechanical hydraulic aperture is to be considered, Eq. (3-17) is used to convert the mechanical aperture into the hydraulic aperture to update the fracture permeability and diffusivity equation is modified to use the hydraulic aperture, w_{ef}, instead of the mechanical aperture, w_f, used in Eq. (4-10).

$$\frac{k_f w_{ef}}{\mu}\frac{\partial^2 p}{\partial x^2} = n\, w_f \Delta L c_f \frac{\partial p}{\partial t} - n\Delta L \frac{\partial D_n}{\partial t} + \Delta L q_{\text{int}} + q_s \qquad (4\text{-}27)$$

4.3.2 Coupled method

The fluid pressure change induces fracture deformation and the fracture deformation also influences the fluid pressure distribution. In the coupled method, the equations for fluid pressure, interface flow rate, and normal and shear fracture displacement are solved simultaneously.

The poroelastic DDM solutions are both space and time dependent, and the fundamental solutions are based on constant displacement discontinuities and constant interface or source flow rates. However, for practical applications, the displacement discontinuities and interface flow rates in Eqs. (4-19) and (4-20) are time dependent. The time marching scheme shown in Figure II-9 is used to allow source strengths (the displacement discontinuities and interface flow rate) to change with time. Starting each boundary integration from an initial homogeneous status avoids the need for volumetric integration (Carvalho, 1990). Therefore, all the previous increments of source strengths must be included while numerically integrating the effect of source strengths at each time step. According to Eq. (2-44), the induced stress and pore pressure on the *ith* fracture segment by the increments of source strengths are:

$$\Delta \overset{i}{\sigma}_n(t) = \sum_{j=1}^{m} \overset{ij}{A}(t-\tau_\xi)\Delta \overset{j\xi}{D}_n + \sum_{j=1}^{m} \overset{ij}{B}(t-\tau_\xi)\Delta \overset{j\xi}{D}_s + \sum_{j=1}^{m} \overset{ij}{C}(t-\tau_\xi)\Delta \overset{j\xi}{q}_{\text{int}}$$
$$+ \sum_{h=0}^{\xi-1}\sum_{j=1}^{m} \overset{ij}{A}(t-\tau_h)\Delta \overset{jh}{D}_n + \sum_{h=0}^{\xi-1}\sum_{j=1}^{m} \overset{ij}{B}(t-\tau_h)\Delta \overset{jh}{D}_s + \sum_{h=0}^{\xi-1}\sum_{j=1}^{m} \overset{ij}{C}(t-\tau_h)\Delta \overset{jh}{q}_{\text{int}}$$

$$\Delta \overset{i}{\sigma}_s(t) = \sum_{j=1}^{m} \overset{ij}{E}(t-\tau_\xi)\Delta \overset{j\xi}{D}_n + \sum_{j=1}^{m} \overset{ij}{F}(t-\tau_\xi)\Delta \overset{j\xi}{D}_s + \sum_{j=1}^{m} \overset{ij}{K}(t-\tau_\xi)\Delta \overset{j\xi}{q}_{\text{int}}$$
$$+ \sum_{h=0}^{\xi-1}\sum_{j=1}^{m} \overset{ij}{E}(t-\tau_h)\Delta \overset{jh}{D}_n + \sum_{h=0}^{\xi-1}\sum_{j=1}^{m} \overset{ij}{F}(t-\tau_h)\Delta \overset{jh}{D}_s + \sum_{h=0}^{\xi-1}\sum_{j=1}^{m} \overset{ij}{K}(t-\tau_h)\Delta \overset{jh}{q}_{\text{int}} \qquad (4\text{-}28)$$

$$\Delta \overset{i}{p}(t) = \sum_{j=1}^{m} \overset{ij}{L}(t-\tau_\xi)\Delta \overset{j\xi}{D}_n + \sum_{j=1}^{m} \overset{ij}{H}(t-\tau_\xi)\Delta \overset{j\xi}{D}_s + \sum_{j=1}^{m} \overset{ij}{N}(t-\tau_\xi)\Delta \overset{j\xi}{q}_{\text{int}}$$
$$+ \sum_{h=0}^{\xi-1}\sum_{j=1}^{m} \overset{ij}{L}(t-\tau_h)\Delta \overset{jh}{D}_n + \sum_{h=0}^{\xi-1}\sum_{j=1}^{m} \overset{ij}{H}(t-\tau_h)\Delta \overset{jh}{D}_s + \sum_{h=0}^{\xi-1}\sum_{j=1}^{m} \overset{ij}{N}(t-\tau_h)\Delta \overset{jh}{q}_{\text{int}}$$

where $\Delta \overset{j\xi}{D}_n$, $\Delta \overset{j\xi}{D}_s$ and $\Delta \overset{j\xi}{q}_{\text{int}}$ are the source strength increments for the *jth* fracture segment at the current time step, ξ; $\Delta \overset{jh}{D}_n$, $\Delta \overset{jh}{D}_s$ and $\Delta \overset{jh}{q}_{\text{int}}$ are the previous source strength increments of for the *jth* fracture segment at time step *h*, which indexed from 1 to ξ-1. $\overset{ij}{A}(t-\tau_h)$, $\overset{ij}{B}(t-\tau_h)$, $\overset{ij}{C}(t-\tau_h)$, $\overset{ij}{E}(t-\tau_h)$, $\overset{ij}{F}(t-\tau_h)$, $\overset{ij}{K}(t-\tau_h)$, $\overset{ij}{L}(t-\tau_h)$, $\overset{ij}{H}(t-\tau_h)$, and $\overset{ij}{N}(t-\tau_h)$ are the influence coefficients of *jth* fracture element on the *ith* fracture element at time step *h* as defined in Eq. (2-38).

Using the same time discretization, the effective normal stress change (Eq. (4-17)) and shear stress change (Eq. (4-15)) in the *ith* fracture segment can be rewritten as:

$$\Delta \overset{i}{\sigma}_n(t) + \overset{i}{p}(t) - \overset{i}{p}_0 = -\overset{i}{K}_n\left(\Delta \overset{i\xi}{D}_n + \Delta \overset{i\xi}{D}_s \tan\phi_d\right) - \overset{i}{K}_n\left(\sum_{h=0}^{\xi-1}\Delta \overset{ih}{D}_n + \tan\phi_d \sum_{h=0}^{\xi-1}\Delta \overset{ih}{D}_s\right)$$

$$\Delta \overset{i}{\sigma}_s(t) = \overset{i}{K}_s\,\Delta \overset{i\xi}{D}_s + \overset{i}{K}_s \sum_{h=0}^{\xi-1}\Delta \overset{ih}{D}_s \tag{4-29}$$

where $\overset{i}{p}(t)$ is the fluid pressure in the *ith* fracture segment at time *t* and $\overset{i}{p}_0$ is the initial fluid pressure in the *ith* fracture segment. Substituting Eq. (4-29) into Eq. (4-28), and substituting $\overset{i}{p}(t) - \overset{i}{p}_0$ for $\Delta \overset{i}{p}(t)$ in Eq. (4-28) yield:

$$\begin{aligned}
&\overset{i}{p}(t) + \sum_{j=1}^{m} \overset{ij}{A}(t-\tau_\xi)\Delta \overset{j\xi}{D}_n + \overset{i}{K}_n\,\Delta \overset{i\xi}{D}_n + \sum_{j=1}^{m} \overset{ij}{B}(t-\tau_\xi)\Delta \overset{j\xi}{D}_s + \overset{i}{K}_n \tan\phi_d \Delta \overset{i\xi}{D}_s \\
&+ \sum_{j=1}^{m} \overset{ij}{C}(t-\tau_\xi)\overset{j\xi}{q}_{\text{int}} = -\sum_{h=0}^{\xi-1}\sum_{j=1}^{m} \overset{ij}{A}(t-\tau_h)\Delta \overset{jh}{D}_n - \sum_{h=0}^{\xi-1}\sum_{j=1}^{m} \overset{ij}{B}(t-\tau_h)\Delta \overset{jh}{D}_s \\
&- \sum_{h=0}^{\xi-1}\sum_{j=1}^{m} \overset{ij}{C}(t-\tau_h)\overset{jh}{q}_{\text{int}} - \overset{i}{K}_n\left(\sum_{h=0}^{\xi-1}\Delta \overset{ih}{D}_n + \tan\phi_d \sum_{h=0}^{\xi-1}\Delta \overset{ih}{D}_s\right) + \overset{i}{p}_0
\end{aligned}$$

$$\begin{aligned}
&\sum_{j=1}^{m} \overset{ij}{E}(t-\tau_\xi)\Delta \overset{j\xi}{D}_n + \sum_{j=1}^{m} \overset{ij}{F}(t-\tau_\xi)\Delta \overset{j\xi}{D}_s - \overset{i}{K}_s\,\Delta \overset{i\xi}{D}_s + \sum_{j=1}^{m} \overset{ij}{K}(t-\tau_\xi)\overset{j\xi}{q}_{\text{int}} = \\
&-\sum_{h=0}^{\xi-1}\sum_{j=1}^{m} \overset{ij}{E}(t-\tau_h)\Delta \overset{jh}{D}_n - \sum_{h=0}^{\xi-1}\sum_{j=1}^{m} \overset{ij}{F}(t-\tau_h)\Delta \overset{jh}{D}_s - \sum_{h=0}^{\xi-1}\sum_{j=1}^{m} \overset{ij}{K}(t-\tau_h)\overset{jh}{q}_{\text{int}} \\
&+ \overset{i}{K}_s \sum_{h=0}^{\xi-1}\Delta \overset{ih}{D}_s
\end{aligned} \tag{4-30}$$

$$\begin{aligned}
&-\overset{i}{p}(t) + \sum_{j=1}^{m} \overset{ij}{L}(t-\tau_\xi)\Delta \overset{j\xi}{D}_n + \sum_{j=1}^{m} \overset{ij}{H}(t-\tau_\xi)\Delta \overset{j\xi}{D}_s + \sum_{j=1}^{m} \overset{ij}{N}(t-\tau_\xi)\overset{j\xi}{q}_{\text{int}} = \\
&-\overset{i}{p}_0 - \sum_{h=0}^{\xi-1}\sum_{j=1}^{m} \overset{ij}{L}(t-\tau_h)\Delta \overset{jh}{D}_n - \sum_{h=0}^{\xi-1}\sum_{j=1}^{m} \overset{ij}{H}(t-\tau_h)\Delta \overset{jh}{D}_s - \sum_{h=0}^{\xi-1}\sum_{j=1}^{m} \overset{ij}{N}(t-\tau_h)\overset{jh}{q}_{\text{int}}
\end{aligned}$$

The diffusivity equation (4-10) is discretized in space and time for a given fracture network using an implicit finite difference method like that given in Appendix C for a regular fracture network. For the *ith* fracture segment at the time step, ξ,

$$\sum_{j=1}^{m} \overset{ij}{C}_p \overset{j}{p}(t) - n\Delta L\Delta \overset{i\xi}{D}_n + \Delta L\Delta \overset{i\xi}{q}_{\text{int}} = n\, w_f \Delta L c_f \overset{i}{p}(\tau_\xi) - \Delta L \sum_{h=0}^{\xi-1} \Delta \overset{ih}{q}_{\text{int}} - \sum_{h=0}^{\xi} \overset{ih}{q}_s \quad (4\text{-}31)$$

where $\overset{ij}{C}_p$ is the fluid coefficient matrix. The production rate from *ith* fracture segment $\overset{ih}{q}_s$ is also discretized in time in Eq. (4-31). All left terms in Eqs. (4-30) and (4-31) are unknown and all right terms are known. Appendix D gives an example matrix for the set of linear equations built from Eqs. (4-30) and (4-31) for a given fracture network. When the production rate and initial reservoir pressure are given, the normal and shear fracture displacement, interface flow rate, and fluid pressure can be obtained by solving the linear equation Eqs. (4-30) and (4-31). Unlike for the uncoupled method, the interface

flow rate is solved implicitly, and there is no need for the FDM determination of the interface flow rate. The treatment for fracture permeability is the same as that for the uncoupled method.

4.4 Chapter conclusions

This chapter presented a new numerical method to solve the fluid pressure, fracture aperture change and stress change simultaneously by combining a finite difference method (FDM) solution for the diffusivity equation for fluid flow in fractures, a fully coupled displacement discontinuity method (DDM) for the global relation of fracture deformation, and the Barton-Bandis fracture deformation model for the local relation of fracture deformation. The fracture permeability changes with the fracture aperture change. Applications of this method are shown in the next chapter.

CHAPTER V

MODEL APPLICATIONS

The coupled method described in Chapter IV applies when a single phase fluid is produced from a naturally fractured reservoir. Pressure decrease causes effective stress change, thereby inducing fracture aperture and permeability change in the natural fractures. The coupled method is applied to quantitatively predict the fracture aperture and permeability change during production under different in situ stress conditions for rock and fracture parameters that can be measured in laboratories and/or from production data.

This chapter will illustrate that under isotropic stress conditions the effective stress increases with reservoir pressure drop, and fracture aperture and permeability decrease with time. Further we will show that under highly anisotropic stress conditions, fracture aperture and permeability in some fractures may not decrease, or may even increase.

This chapter will start with applications under isotropic in situ stress conditions in Section 5.1. Next will be applications under high anisotropic in situ stress conditions in Section 5.2. Finally chapter conclusions are in Section 5.3.

5.1 Fracture aperture and permeability change under isotropic conditions

In this section the coupled solution method is applied to a case under isotropic stress conditions. The results of reservoir pressure change, stress change, fracture

aperture and permeability change are shown, and the interactions of these changes are discussed. The influences of input rock and fracture properties on the results are also investigated.

5.1.1 Parameters and assumptions

In this section the fracture permeability change during production and its effect on transient wellbore pressure are investigated for a well with constant production rate (12.6 Res bbl/day) from a unit reservoir thickness of 3.28 ft (1 m) in a formation with a fracture network consisting of two sets of orthogonal vertical fractures surrounded by an effectively infinite porous medium as in Figure V-1. The fracture permeability is calculated from the mechanical aperture using the cubic law for the ratio of hydraulic aperture to the mechanical aperture (w_{ef}/w_f) assumed to be 1. (Cases for other ratios will be discussed later). Only two-dimensional flow and deformation are considered, and change in the vertical direction is ignored. The in situ stress field before production is assumed to be isotropic with compression set to 3045 psi. To better illustrate the geomechanic effects during production, the reservoir pressure is set very close to the in situ stress at 2900 psi. The two joint parameters, initial normal stiffness and maximum closure, characterizing the normal deformation of fracture are 2.21×10^4 psi/ft and 0.0315 in, respectively. The nonlinear relationship between effective normal stress under compression and fracture closure is shown in Figure V-2. The fracture aperture at the initial condition (zero effective normal stress) is assumed as 0.0315 in. The fracture aperture under the initial in situ stress before production is assumed as 0.009 in for all

fractures. Other parameters are listed in Table V-1. Because the fracture permeability dominates the reservoir permeability, changes in matrix permeability are neglected and assumed as constant during production.

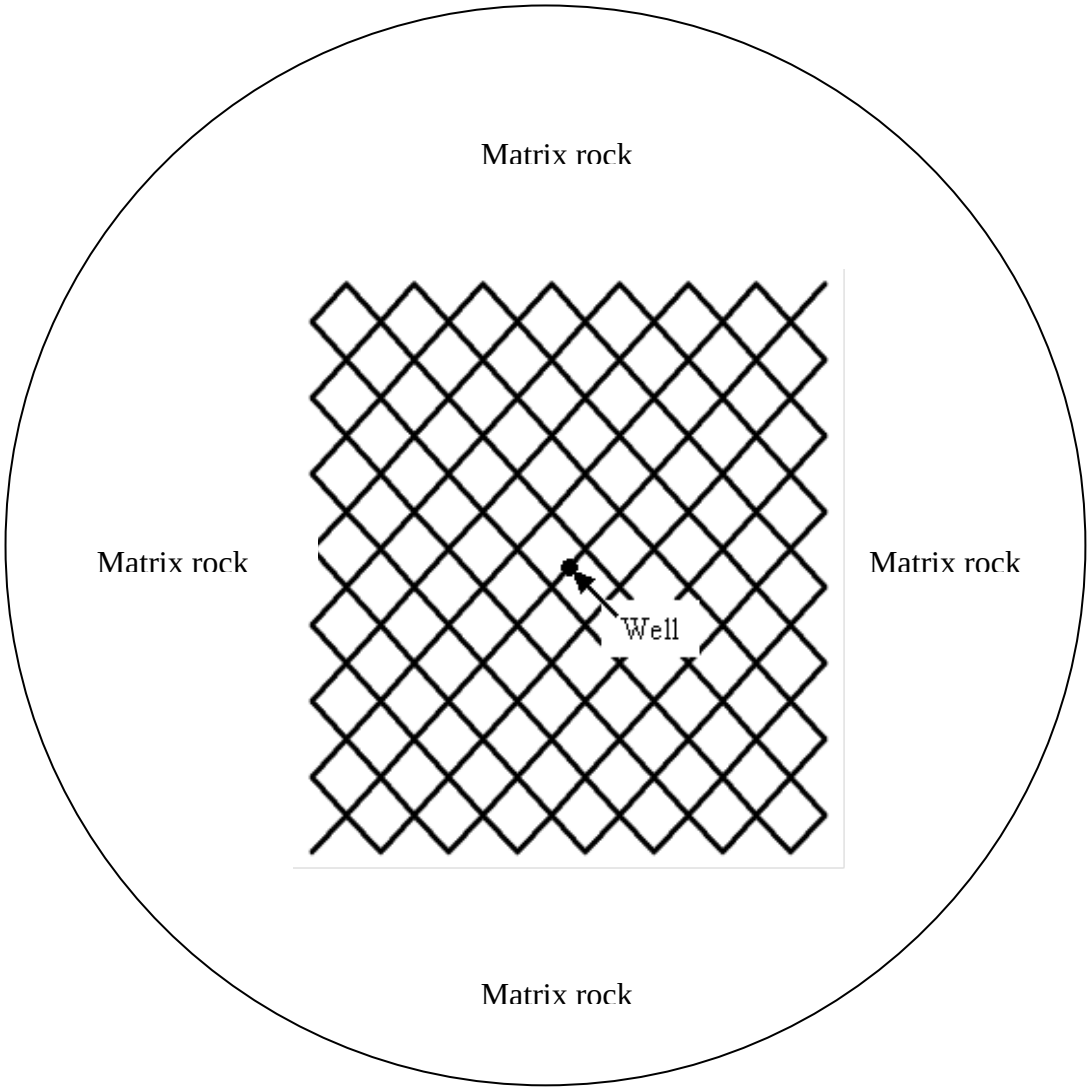

Figure V-1. Well located at the center of a fractured field, which is surrounded by matrix rock of effectively infinite extent.

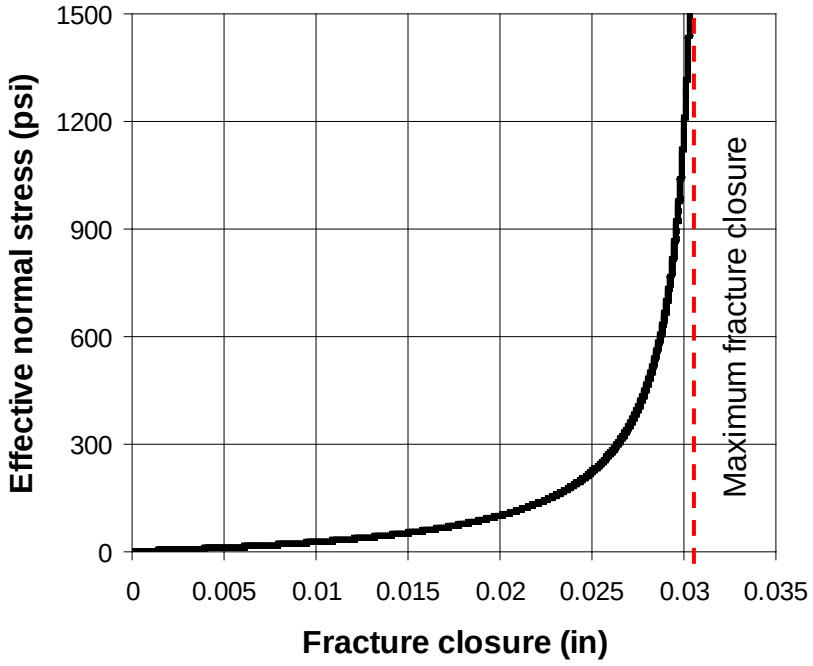

Figure V-2. Nonlinear fracture normal deformation.

Table V-1. Rock and fracture parameters in the modeling.

Area (ft^2)	3281×3281
Shear modulus G (psi)	8.555×10^5
Possoin's ratio υ	0.16
Undrained Possoin's ratio υ_u	0.31
Matrix permeability (md)	0.8
Matrix porosity ϕ	0.2
Biot's coefficient α	0.83
Fluid viscosity μ (cp)	1
Fluid compressibility (psi^{-1})	4.69×10^{-6}
Ratio of actual fracture volume to the effective fracture volume n	10
Fracture spacing S (ft)	310

5.1.2 Results for isotropic stress conditions

Figure V-3 shows the reservoir pressure distribution after 360 days on production. In this case, the lowest pressure is 2635 psi, and the highest pressure is 2672 psi. The fracture aperture declines with production as in Figure V-4. The fracture intersected with the well has the maximum fracture closure with the aperture changing from 9.02×10^{-3} in to 4.82×10^{-3} in. The aperture of a fracture on the boundary shows the minimum fracture closure change from 9.02×10^{-3} in to 5.5×10^{-3} in. The effective normal stress increases with time. The change of effective normal stress and fracture aperture for the facture intersected with well and for a boundary fracture with minimum change are shown in Figure V-5. Figure V-6 shows that the fracture permeability calculated from the fracture aperture using the cubic law has the same trend as the aperture change, and changes from 4428 darcy to 1266 darcy at the well and from 4428 darcy to 1645 darcy at the boundary. The pressure in the fracture intersected with the well is assumed as the bottomhole pressure. Figure V-7 compares the bottomhole pressure versus time behavior for the stress-dependent fracture permeability to that for the fixed fracture permeability case. At early time stage while most of the fluid production from the fracture network is mainly driven by the contraction of fracture volume and fluid expansion, both the pressure drop and pressure derivative show a unit slope trend. At the medium stage, the pressure derivative for the fixed fracture permeability case shows infinite-acting radial flow behavior, and the stress-dependent fracture permeability case shows a higher derivative level indicating lower reservoir permeability. At the late stage,

both pressure drop and derivative behavior show the boundary of the fracture system. The late stage behavior is actually a transition to the infinite-acting radial flow trend for flow in the surrounding porous medium, as seen in Figure V-8. But the pressure derivative for the stress dependent fracture permeability case still increases at very late stage showed in Figure V-8 because the fracture permeability decreases with production.

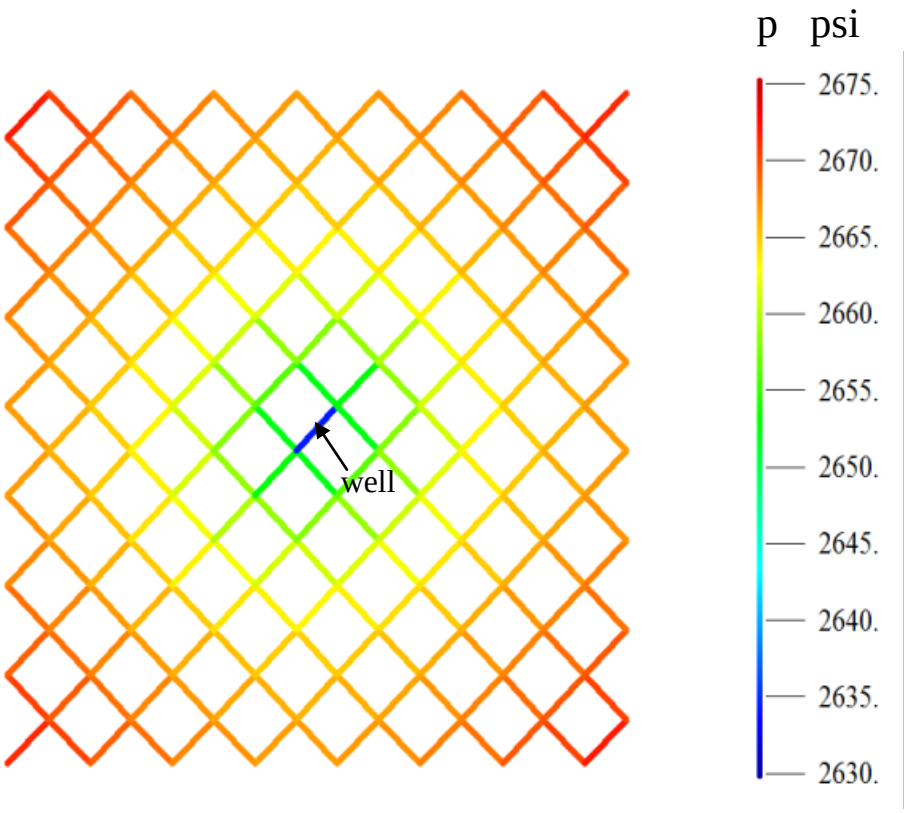

Figure V-3. Pore pressure distribution after 360 days production.

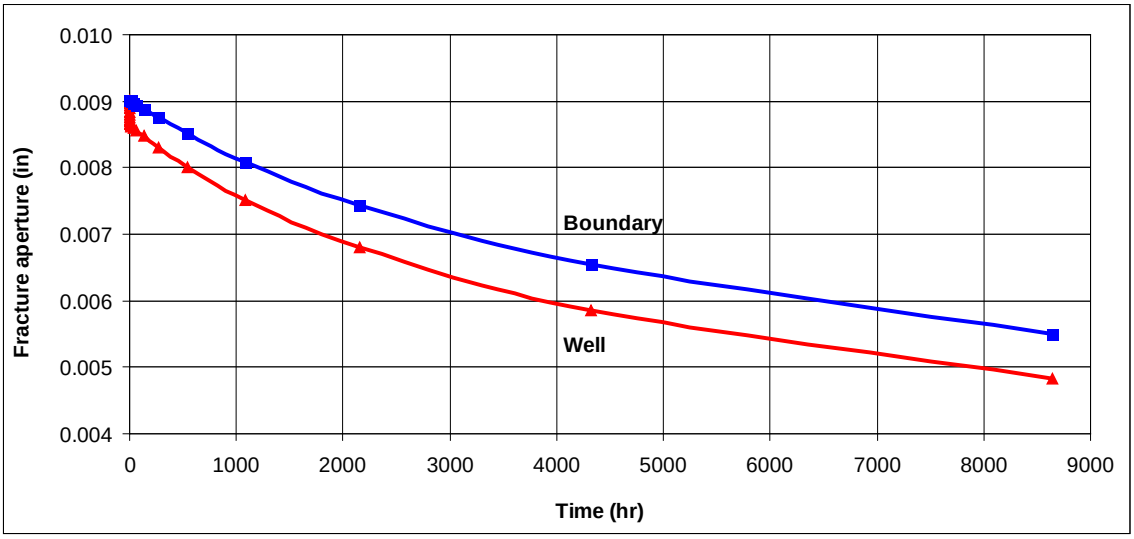

Figure V-4. Fracture aperture declines with time.

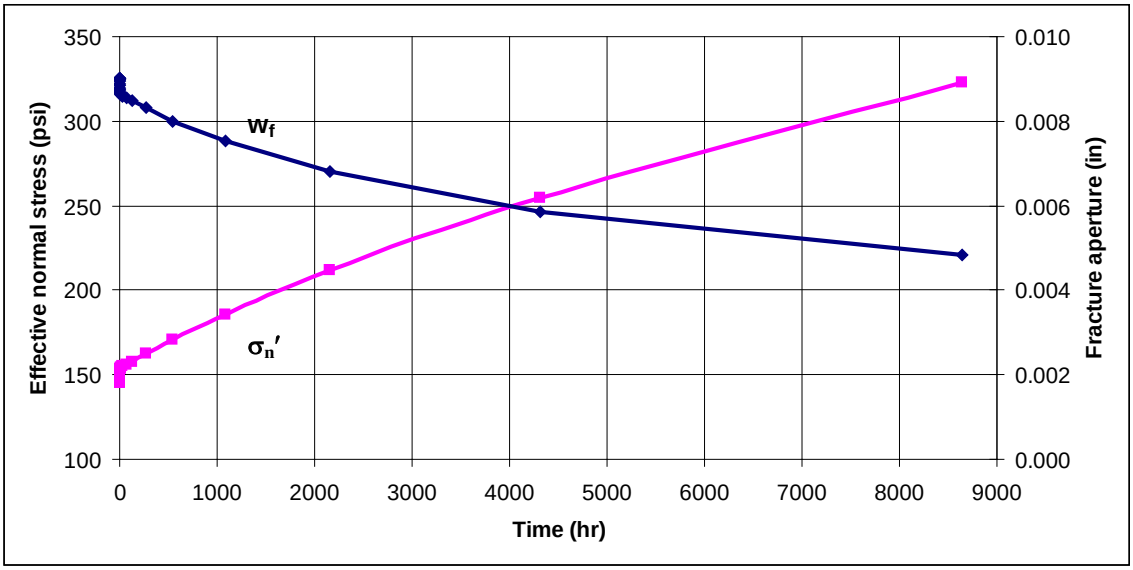

Figure V-5. Effective normal stress and fracture aperture change with time for the fracture intersected with well.

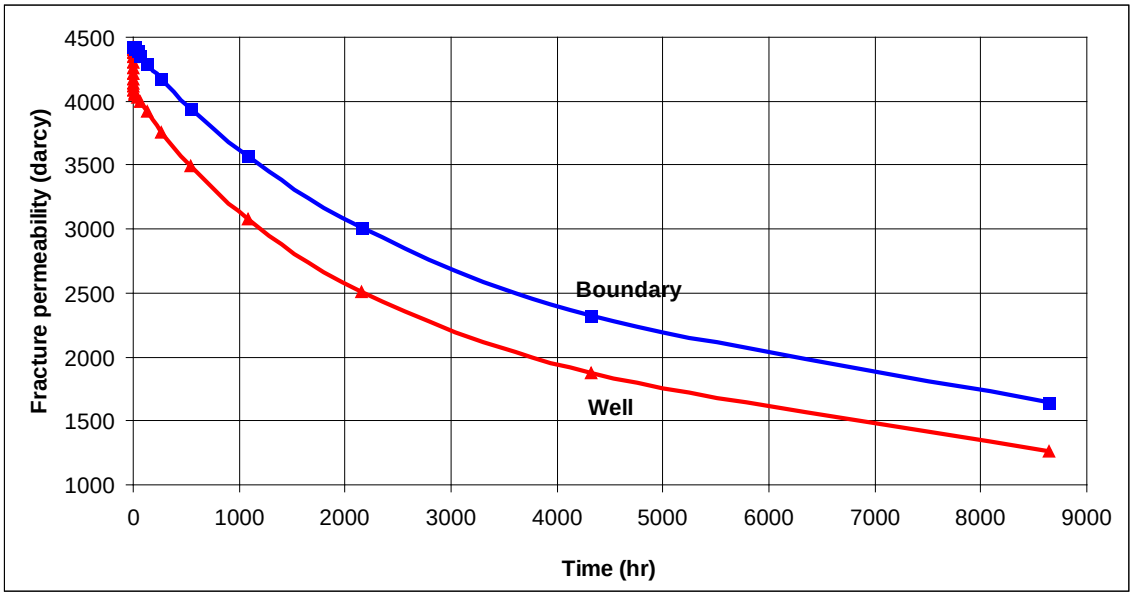

Figure V-6. Fracture permeability declines with time.

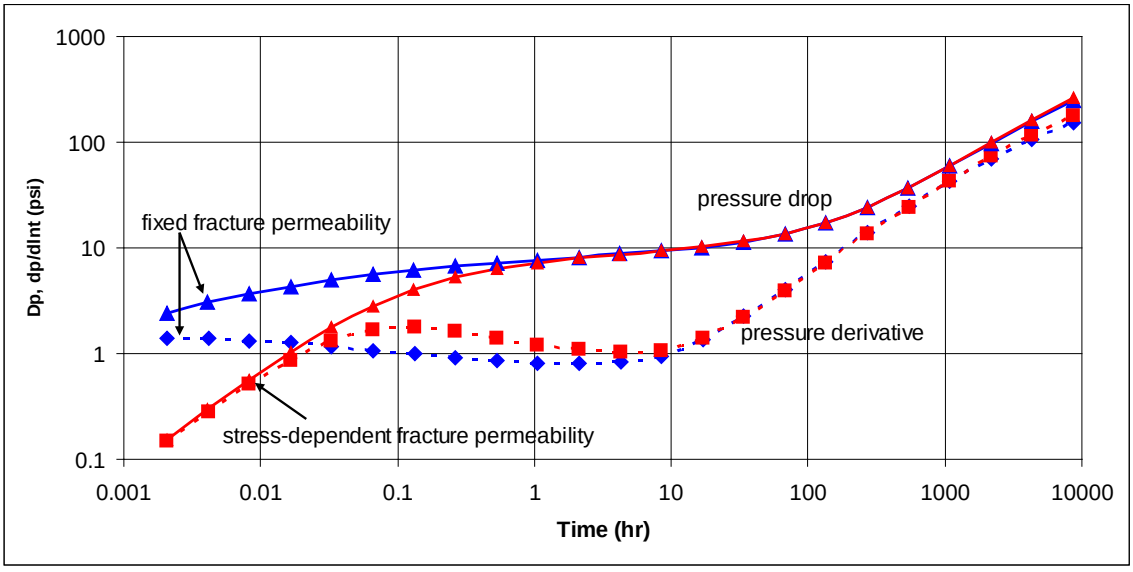

Figure V-7. Comparison of transient pressure behavior at bottom hole with constant production rate between fixed fracture permeability and stress-dependent fracture permeability case.

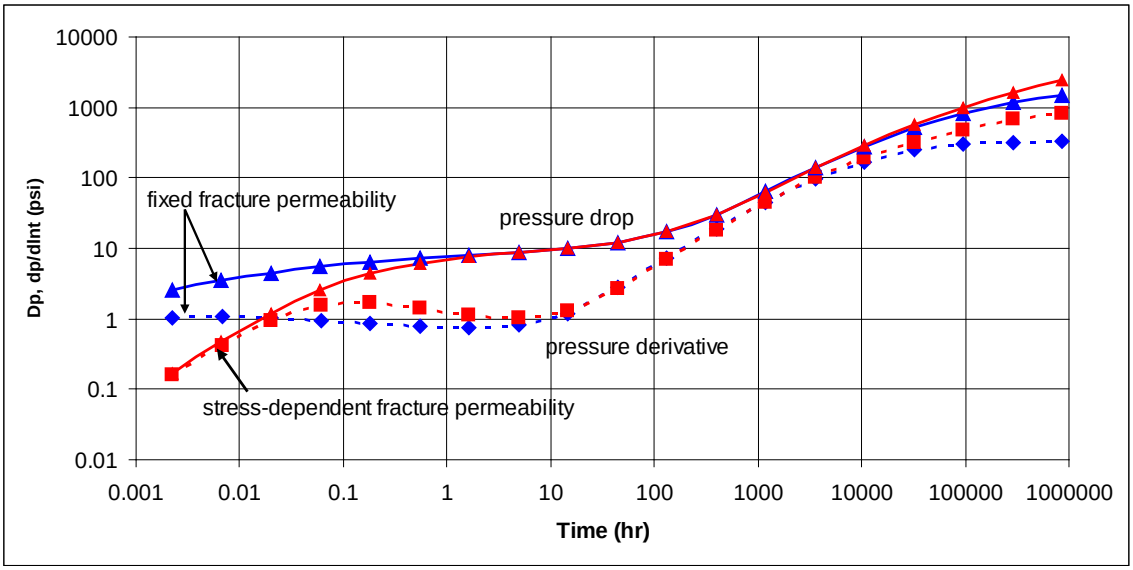

Figure V-8. Comparison of transient pressure behavior at bottom hole with constant production rate between fixed fracture permeability and stress-dependent fracture permeability case for a long time production to show the flow behavior in the surrounded matrix rock.

The next example shown in Figure V-9 compares the previous stress dependent fracture network case to that of a well producing from the unfractured porous medium. In this comparison the pressure of the fracture intersected by the well is assumed as the bottomhole pressure, and the pressure in a small square fracture element with cross section area equal to that of the well is used for bottomhole pressure for the well in the unfractured reservoir. (For example, if the well radius is 0.328 ft, both the length and aperture of the fracture element is 0.581 ft.) Because the fracture element is meant to represent the well, the fracture aperture and length are fixed during the production. The comparison shows that the bottomhole pressure drops much less for the case with a fracture network. The early time pressure derivative trends indicate that the effective permeability of the fracture system is much larger than that of the matrix for the case without any fracture. In late time the infinite-acting radial flow is the same for both cases.

Figure V-10 compares the previous stress dependent fracture network case to a well intersecting the only fracture in the reservoir. The fractures and matrix properties are the same for the two cases, and the fracture length for the fracture intersected by the well is the fracture spacing (310 ft) in the fractured reservoir case. Again, the bottomhole pressure drops much less for the fractured network case (Figure V-11). The infinite-acting radial flow behavior for both cases is the same in late time.

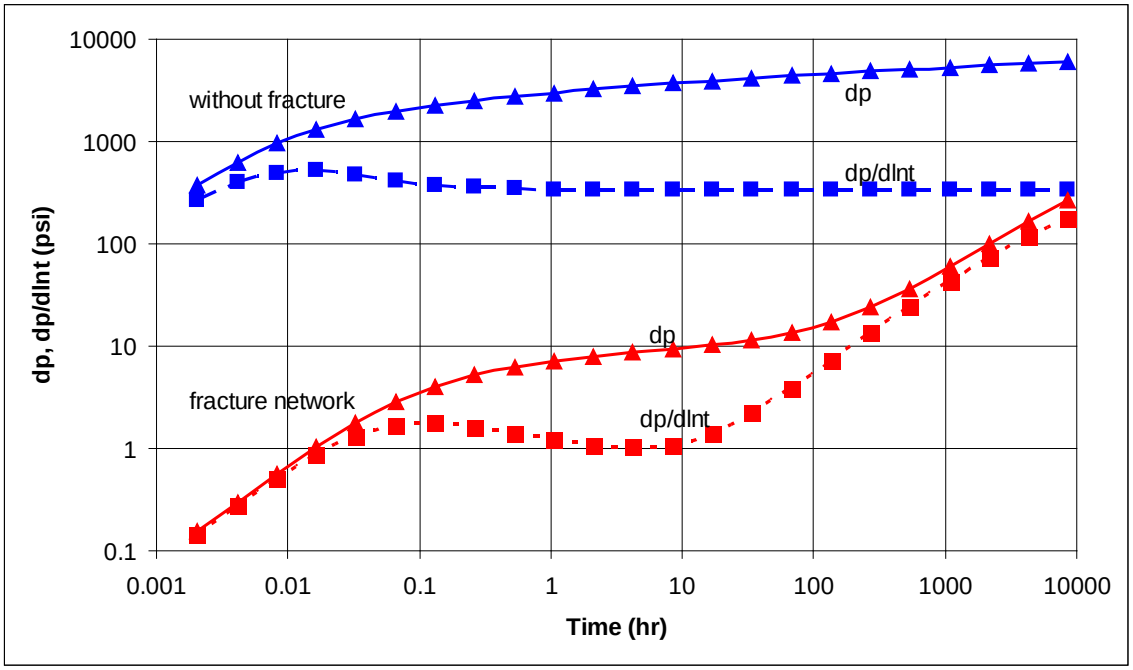

Figure V-9. Comparison of transient pressure behavior at bottom hole with constant production rate between the case with a well connected with a fracture network and the case without any fracture.

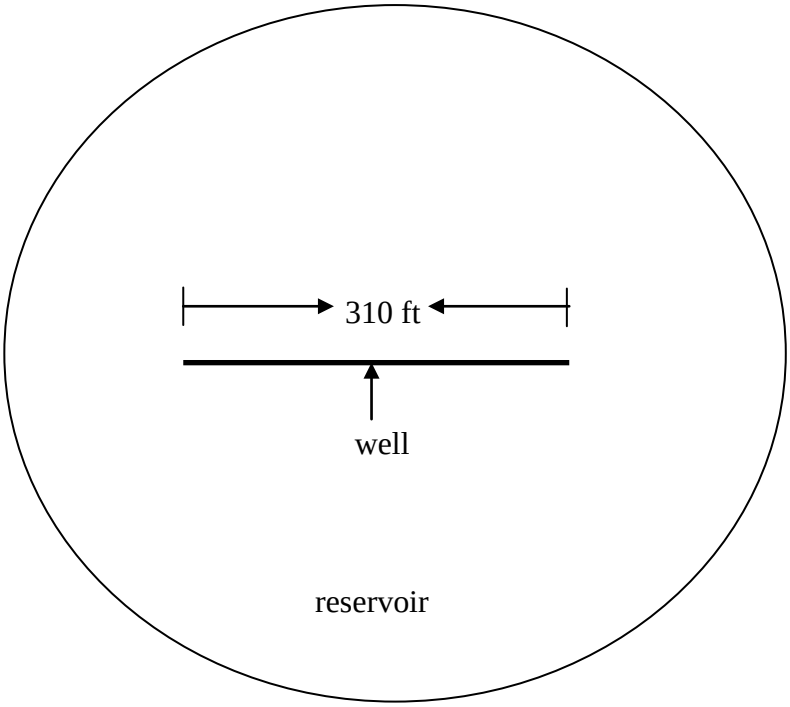

Figure V-10. A well is intersected with a fracture in a non-fractured reservoir.

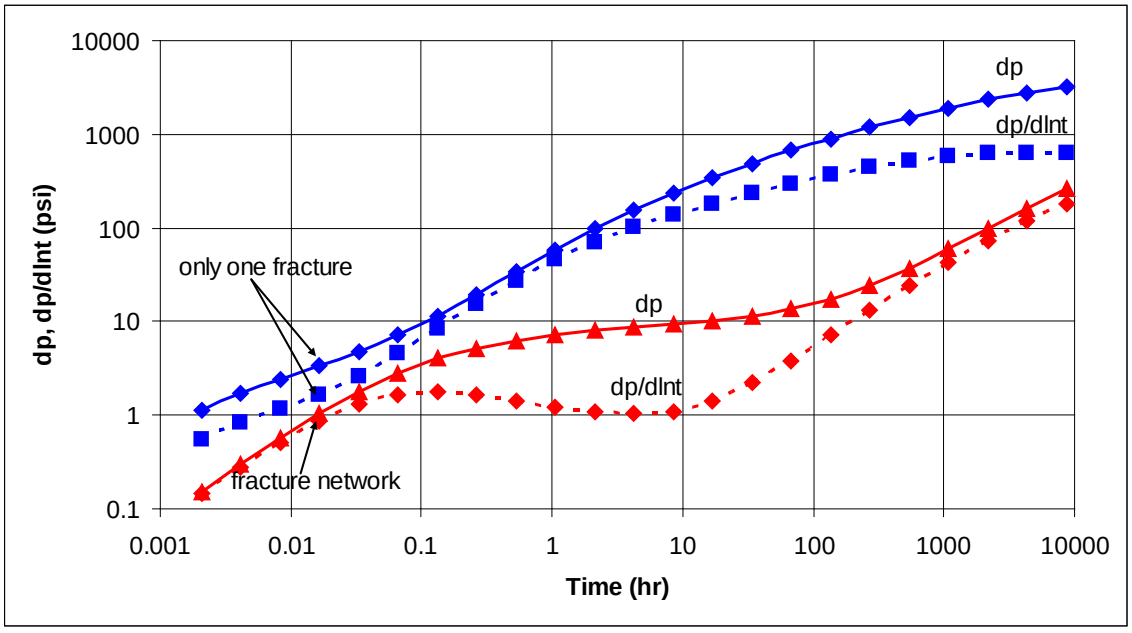

Figure V-11. Comparison of transient pressure behavior at bottom hole with constant production rate between the case with a well connected with a fracture network and the case with only one fracture in the reservoir.

Figure V-12 compares the previous stress dependent fracture network case to a well that does not intersect any natural fracture, with the well located at the center of the matrix element in the center of the fracture network. Except for that the fracture spacing of 290 ft (adjusted to make the fracture network area the same as in the other cases), all other parameters are the same as the case in which the well is connected with the fracture network. The bottomhole pressure drops much more compared with the case of a well connected with a fracture network (Figure V-13). Initially the pressure derivative for the case of the well that does not intersect a fracture shows the trend for infinite-acting radial flow in the matrix permeability. Later, when the pressure disturbance reaches the fracture network, the higher permeability in the fractures causes a leveling in the pressure change. At the late stage, for both cases the fracture network conducts the pressure disturbance to the outer matrix, and both cases have identical pressure derivative trends.

From the perspective of pressure transient testing, the case with the well not intersecting the fracture network is quite intriguing because it exhibits apparent classic dual porosity behavior, but for the opposite reason from that usually applied for this response. The initial and final dual porosity trend is that of the matrix, and not that of the natural fractures, and the valley trend in the pressure derivative does not represent recharge from the matrix; instead, it represents the higher permeability natural fractures encountered before the pressure disturbance encounters the outer matrix with effectively infinite extent.

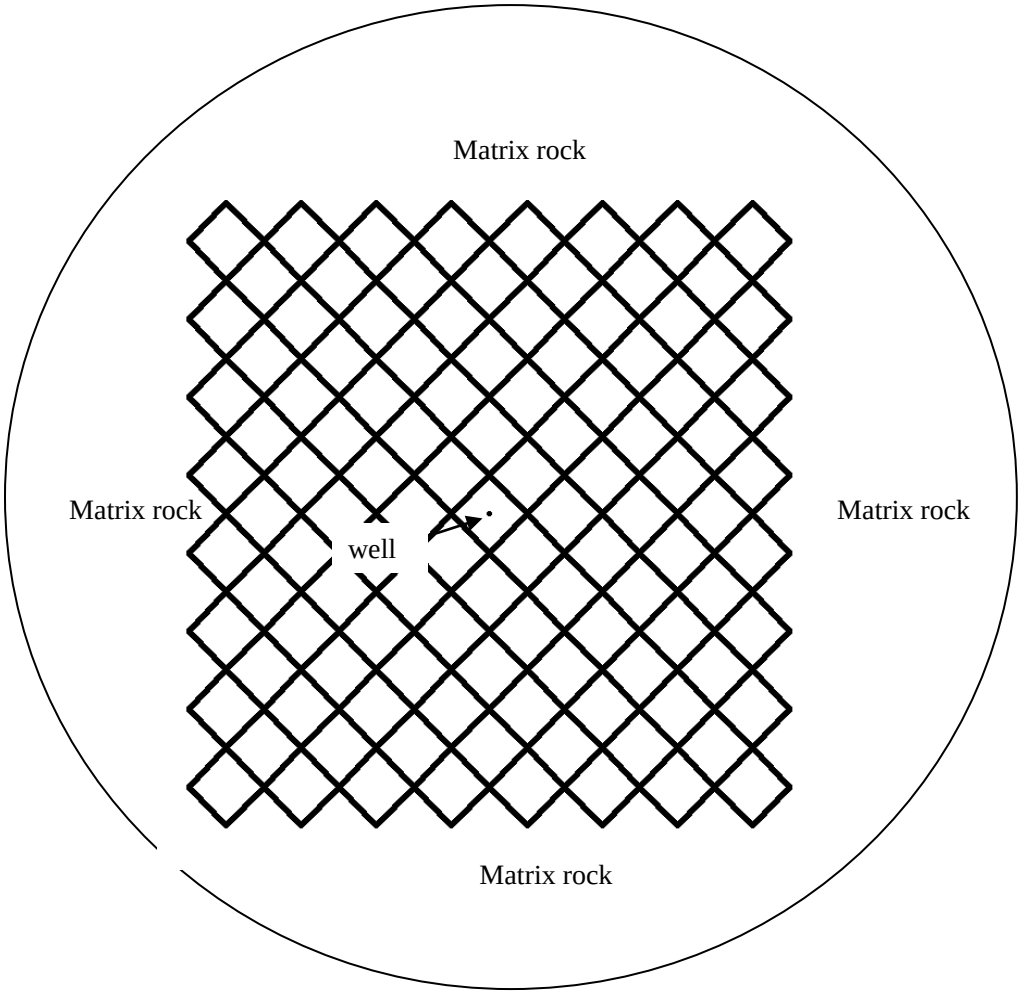

Figure V-12. A well is located at the center of a matrix in a fractured network surrounded by matrix rock.

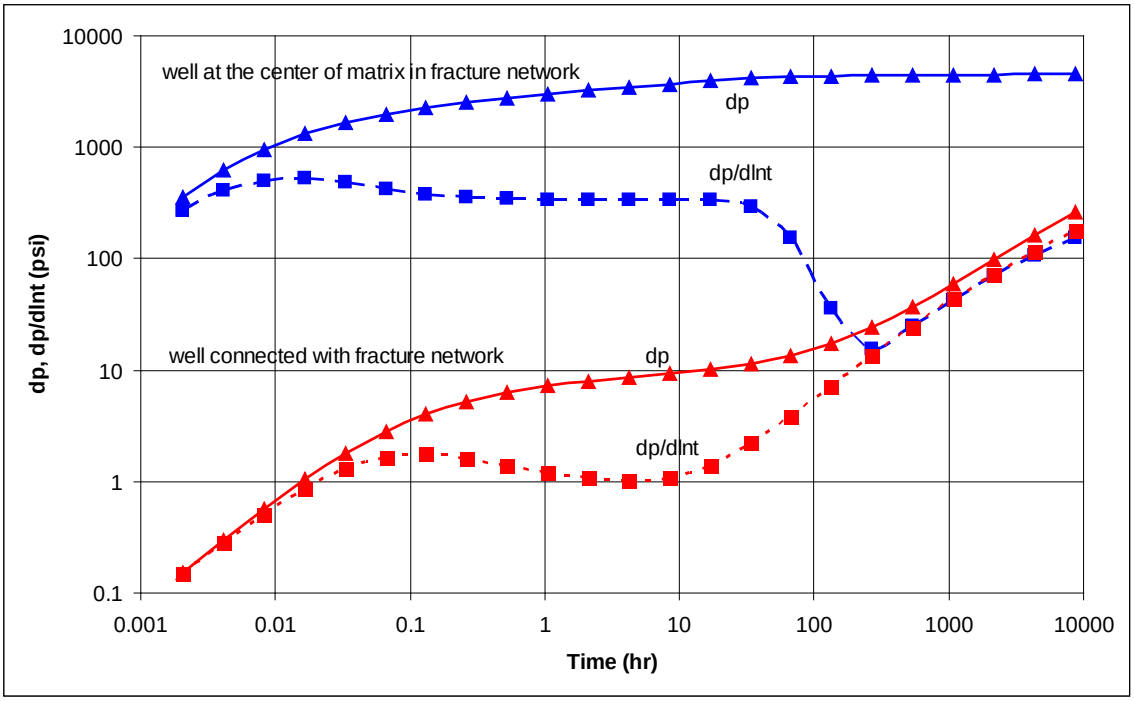

Figure V-13. Comparison of transient pressure behavior at bottom hole with constant production rate between the case with a well connected with a fracture network and the case with a well at the center of a matrix in a fracture network.

For the original stress dependent fracture network case as the fracture permeability declines with production, build up tests at different times show the change in the fracture network permeability. Figure V-14 shows three successive simulated build ups tests, conducted at different times. The rate history is listed in Table V-2. The pressure derivative level is higher before the transition to the outer matrix behavior with successively later buildup tests because the reservoir permeability declines with production. It is difficult to use a single buildup test to determine the rock and joint properties. However, these examples show that any one buildup test may indicate whether the natural fracture system is stress sensitive, and manual history matching with multiple pressure buildup tests may enable quantification of rock and joint properties.

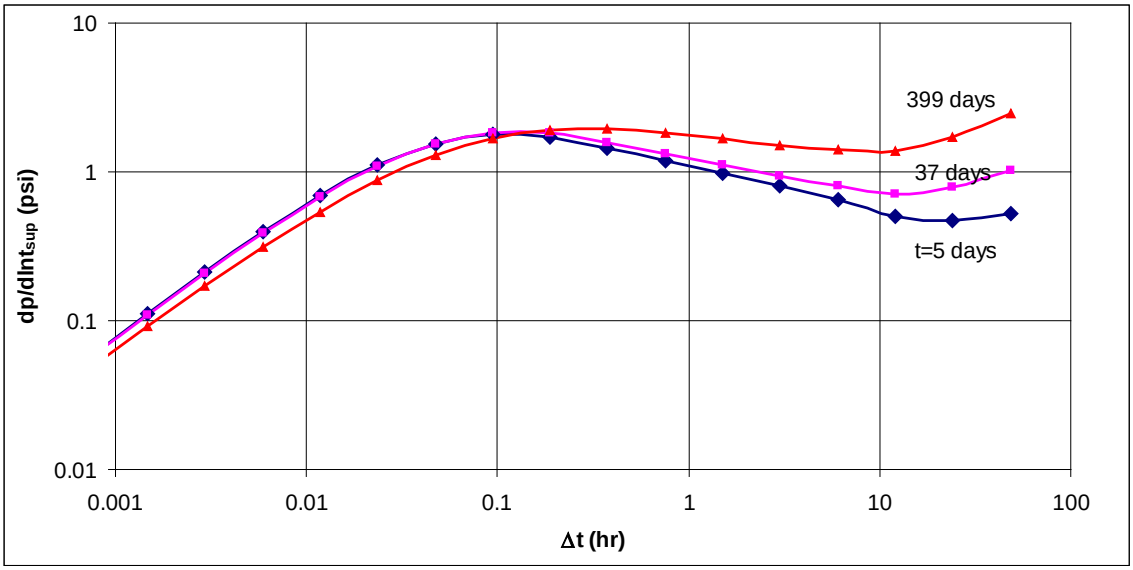

Figure V-14. Pressure derivative curves for successive build ups.

Table V-2. Production rate history.

Duration (days)	Production rate (Res bbl/day)
5	12.6
2	0
30	12.6
2	0
360	12.6
2	0

5.1.3 Effect of initial effective normal stress

The slope of the trend in Figure V-2 gives the normal fracture stiffness, which changes with the effective stress, from a small value at small effective stress to a rapidly increasing value at high effective stress. As such, the fracture is more deformable when

the reservoir pressure is close to the in situ stress than when there is a large contrast between them. To study the influence of a higher stiffness, consider the same initial fracture aperture of 9.02×10^{-3} in and fracture permeability of 4428 darcy before production, but set the initial in situ stress to a value that increases the effective stress while all other properties remain same. Figure V-15 shows the fracture permeability change at the well for different effective in situ stress conditions. The influence of production on the fracture permeability change strongly depends on the initial effective stress condition, and decreases rapidly with increase in the effective in situ stress. The fracture permeability only reduces 3.3% of the initial permeability of 4428 darcy for the case with an effective in situ stress of 1450 psi. However fracture permeability loss for the case with an effective in situ stress of 145 psi is 84.7% of the initial permeability.

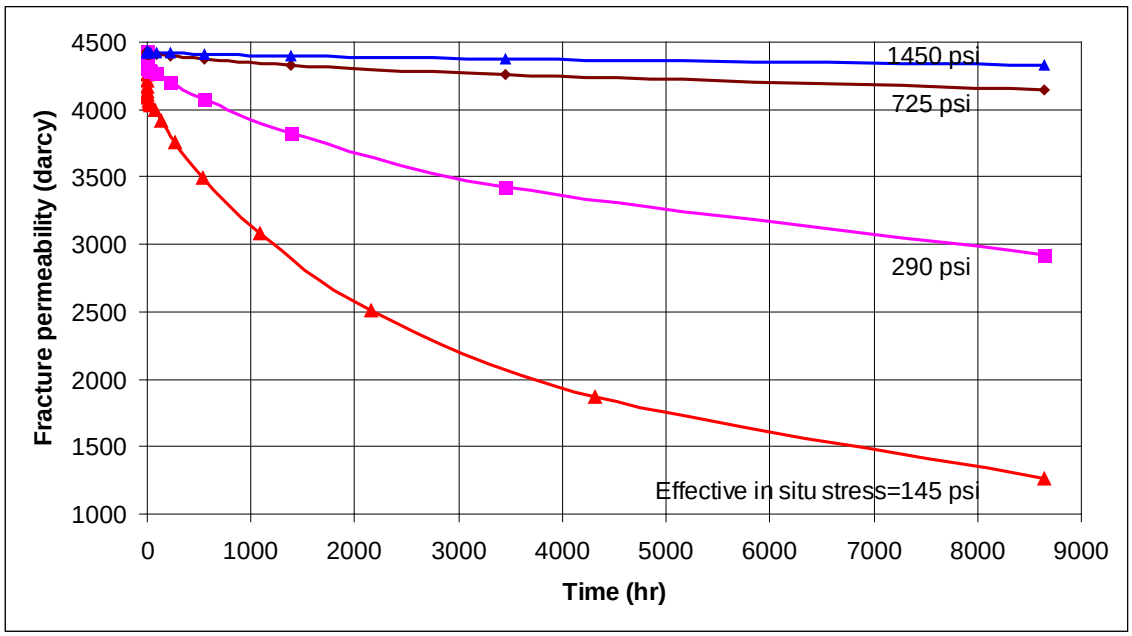

Figure V-15. Effect of initial effective in situ stress on the fracture permeability change.

5.1.4 Effect of ratio of hydraulic fracture aperture to mechanical fracture aperture (wef /w_f)

The ratio of effective hydraulic fracture aperture to mechanical fracture aperture (w_{ef}/w_f) is assumed as 1 in the above analysis. This assumption is only valid for fractures with wide fracture apertures and smooth fracture surfaces. The effective hydraulic fracture aperture w_{ef} is less than the mechanical fracture aperture w_f, and the ratio w_{ef}/w_f is dependent on w_f and the joint roughness coefficient (JRC) (Eq. (3-17)).

Figure V-16 compares cases with three different values for the w_{ef}/w_f ratio. In each case, the maximum fracture closure is 0.0393 in, and the initial mechanical fracture aperture w_f before production is 0.0131 in. In addition, the fracture aperture without stress loading is assumed to be 0.0393 in and it is assumed to be reduced to 0.0131 in for all fractures due to the compression in the reservoir before production. All other parameters remain the same as in the previous examples. Figure V-16 shows that the ratio w_{ef}/w_f increases linearly with the increase of w_f, the slope is a function of JRC and decreases with the decrease of JRC. But the ratio w_{ef}/w_f cannot exceed the limit value 1. Three cases are investigated for unit ratio w_{ef}/w_f, JRC=10.2 and JRC=12, respectively. The fracture permeability is calculated from w_{ef} using cubic law (Eq. (3-15)) and updated with the change of w_{ef} during the simulation.

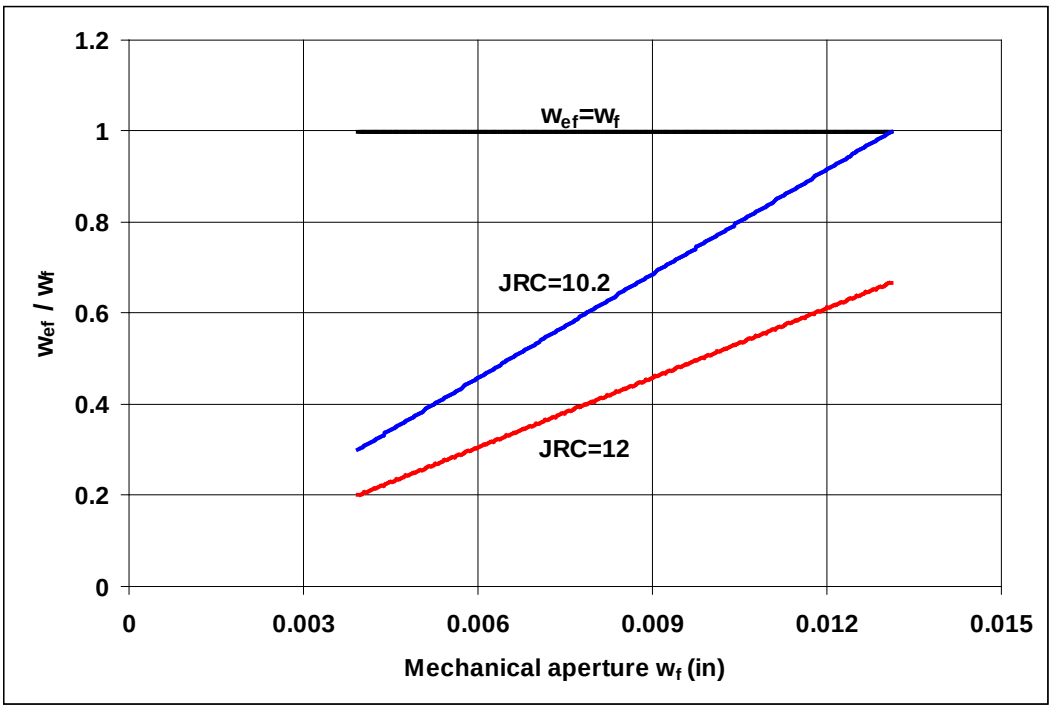

Figure V-16. The ratio w_{ef}/w_f as a function of w_f.

For the same mechanical aperture, the hydraulic aperture and permeability for the case with JRC=12 is lower than the other two cases. Consequently, the pressure drop for JRC=12 is higher than that in the other two cases, as seen in Figure V-17 and Figure V-18. The higher pressure drop in turn causes higher mechanical aperture change seen in Figure V-19 leading to higher hydraulic aperture change seen in Figure V-20, and thereby the high permeability loss seen in Figure V-21.

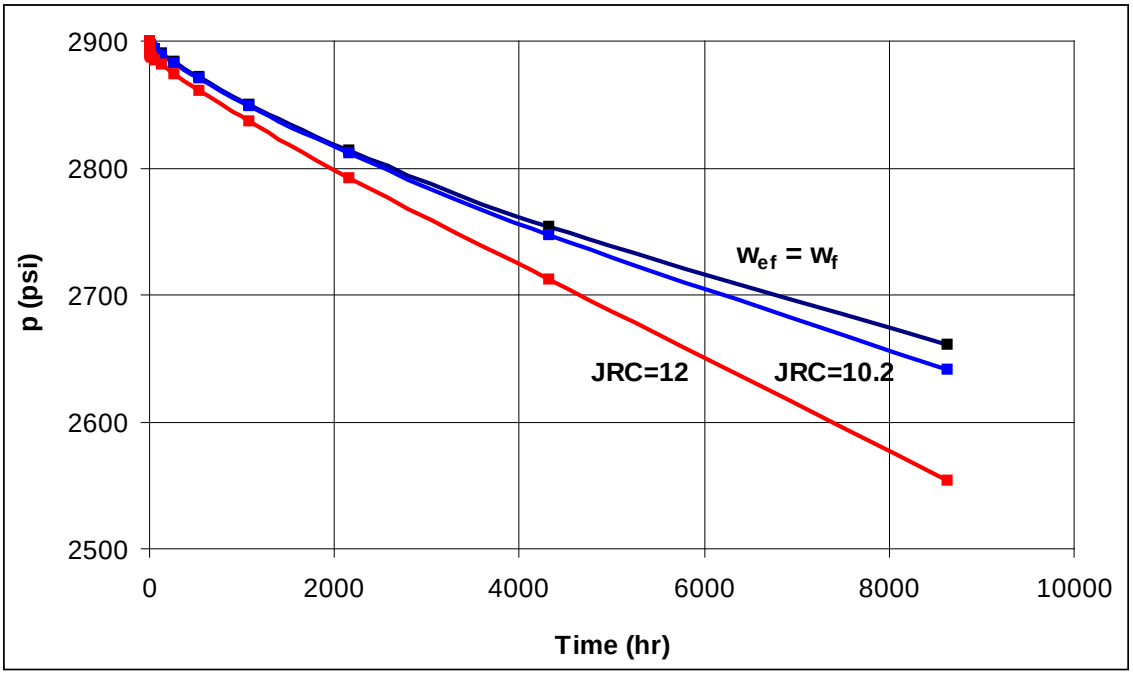

Figure V-17. Bottom hole pressure declines with time for three cases: $w_{ef}=w_f$, JRC=10.2 and JRC=12.

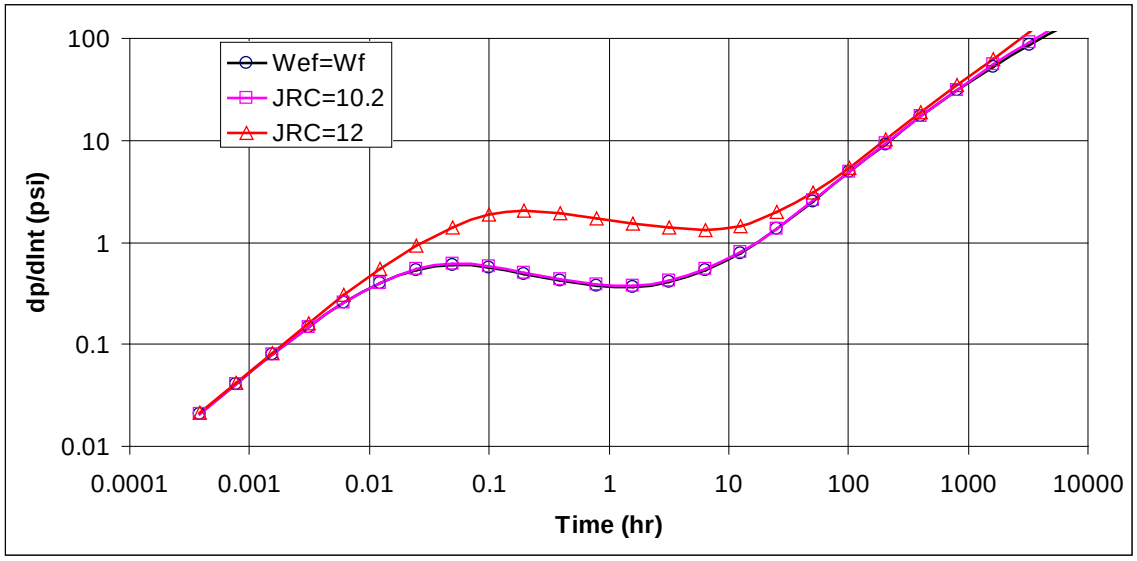

Figure V-18. Log-log plot of the pressure derivatives for three cases: $w_{ef}=w_f$, JRC=10.2 and JRC=12.

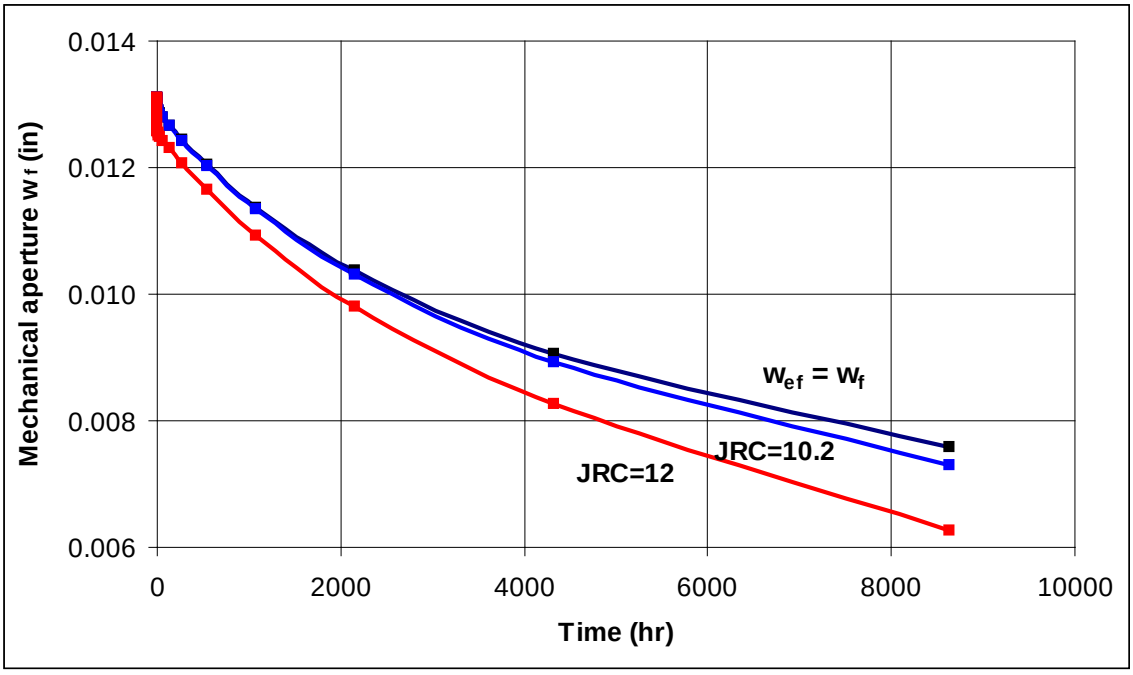

Figure V-19. The mechanical aperture of fracture intersected with well changes with time for three cases: $w_{ef}=w_f$, JRC=10.2 and JRC=12.

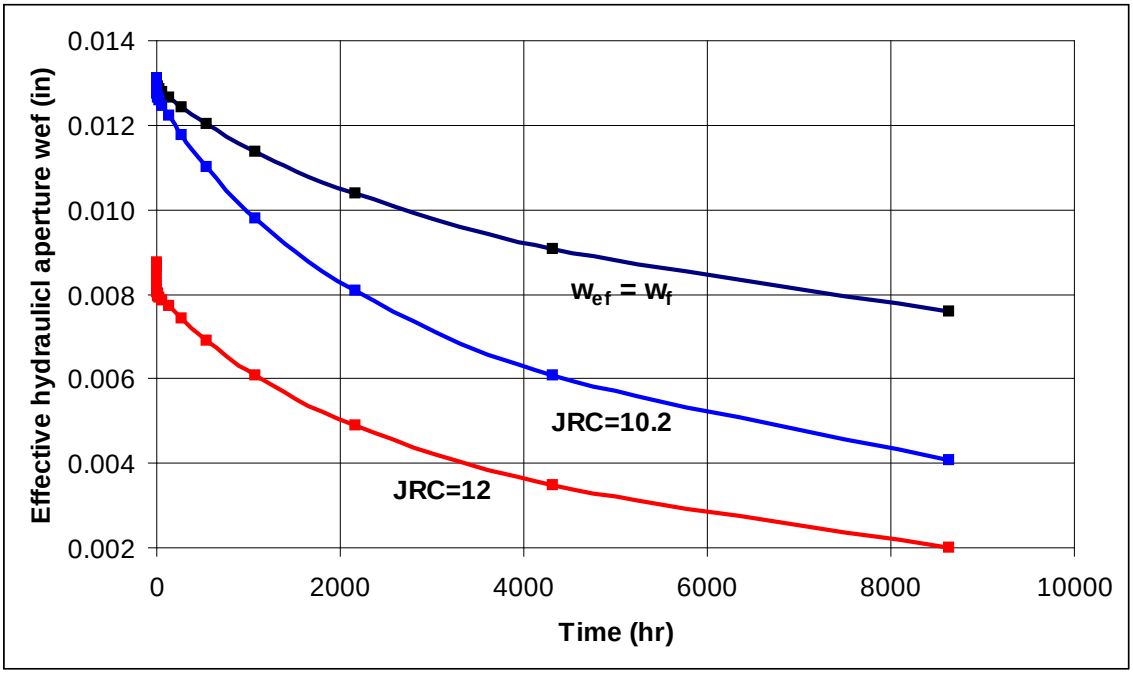

Figure V-20. The effective hydraulic aperture of fracture intersected with well changes with time for three cases: $w_{ef}=w_f$, JRC=10.2 and JRC=12.

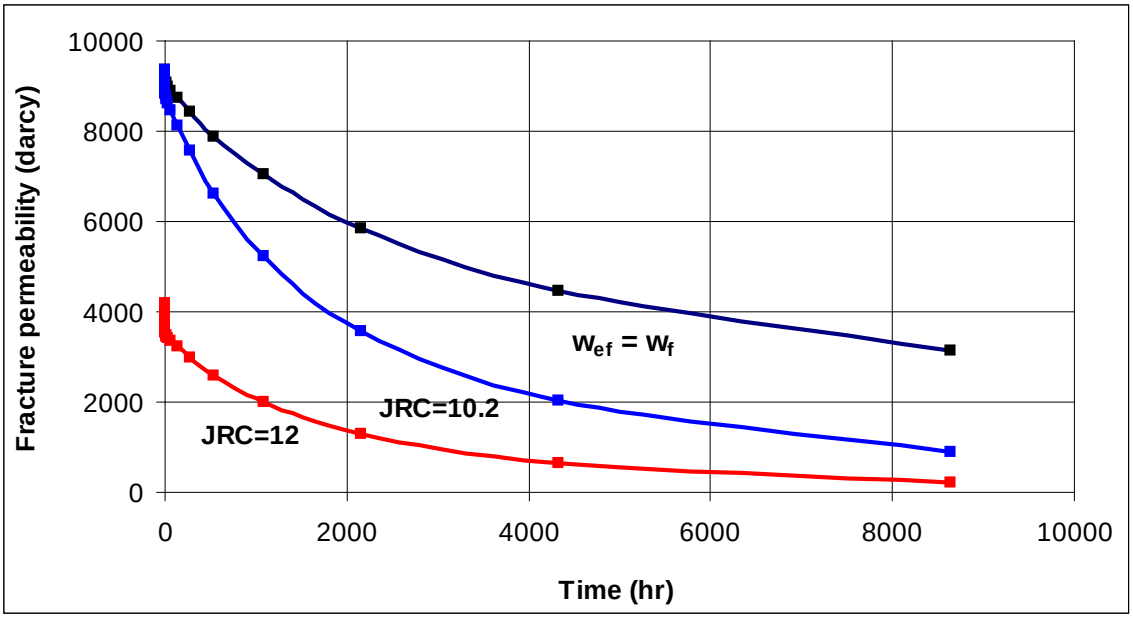

Figure V-21. The permeability of fracture intersected with well changes with time for three cases: $w_{ef}=w_f$, JRC=10.2 and JRC=12.

5.2 Fracture aperture and permeability change under high anisotropic in situ stress conditions

The examples in the previous section all assumed isotropic in situ stress conditions. This section considers anisotropic in situ stress conditions. The shear deformation of a fracture is approximately linear before yielding and is treated as linear here, as is characteristic of a constant shear stiffness value. The shear stiffness is abruptly reduced to zero after yielding as in Figure V-22. The yielding stress can be calculated using Eq. (3-1). But the simplified formula given in Eq. (5-1) is used in this study to calculate the yielding stress according the effective normal stress and the internal friction angle.

$$\tau_{peak} = \sigma_n^{'} \tan\phi_i \qquad (5\text{-}1)$$

where ϕ_i is the internal friction angle. For reservoirs already at the critical stress conditions the fractures are already yielded. Therefore the fractures are very week and the shear stress disturbance can result in large shear deformation. The shear deformation will induce some normal deformation by dilation.

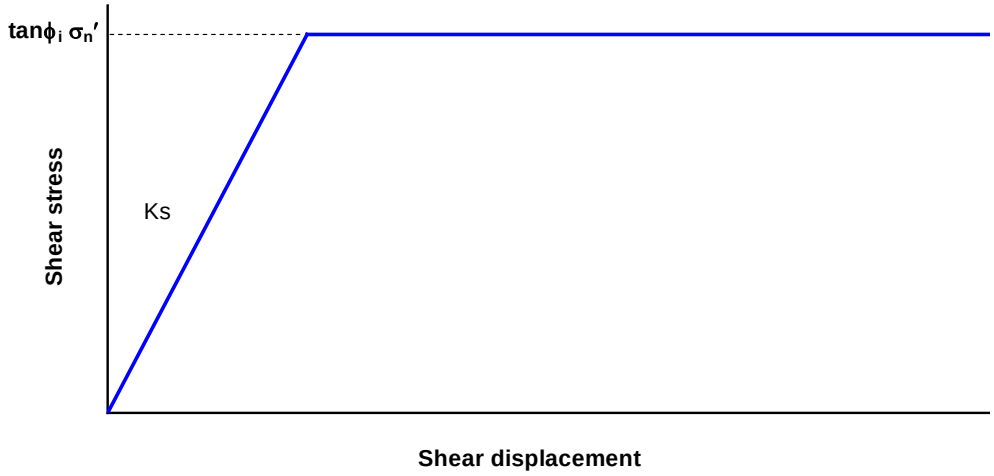

Figure V-22. The relation of shear stress and shear displacement used in the modeling.

In Figure V-23 a fractured reservoir with high anisotropic in situ stress (σ_1=4350 *psi*, σ_3=3335 *psi*) has are two sets of fractures with an angle of 60°. The shear stiffness before yielding is 3.7×10^5 psi/in, the internal friction angle is 30°, the dilation angle is 5°, the fracture spacing is 437 ft, and all other parameters are the same as those in the isotropic case listed in Table V-1. All fractures are already yielded before production and the production with a constant rate of 12.6 Res bbl/day induces not only the normal deformation but also large shear deformation. Figure V-24 shows the direction and

magnitude of the shear displacement after 360 days production. If the shear dilation induces more openness of the fracture than the closure induced by the increase of the effective normal stress, the fracture permeability will increase with production instead of reduction. Figure V-25 shows the fracture permeability distribution after 360 days production. There is still reduction of fracture permeability for those fractures in dark blue. But the fracture permeability for other fractures increases compared with the initial fracture permeability of 4428 darcy. The fracture permeability and shear displacement are compared and show consistent increase (Figure V-26). Figure V-27 shows that the fracture permeability increases with production both for the fracture intersected by the well and for a fracture at the boundary with the maximum enhancement. Figure V-28 shows the change and derivative of the bottomhole pressure, which also shows the enhancement of fracture permeability with production compared with the case of fixed fracture permeability. Therefore, under highly anisotropic stress conditions production may increase the fracture permeability.

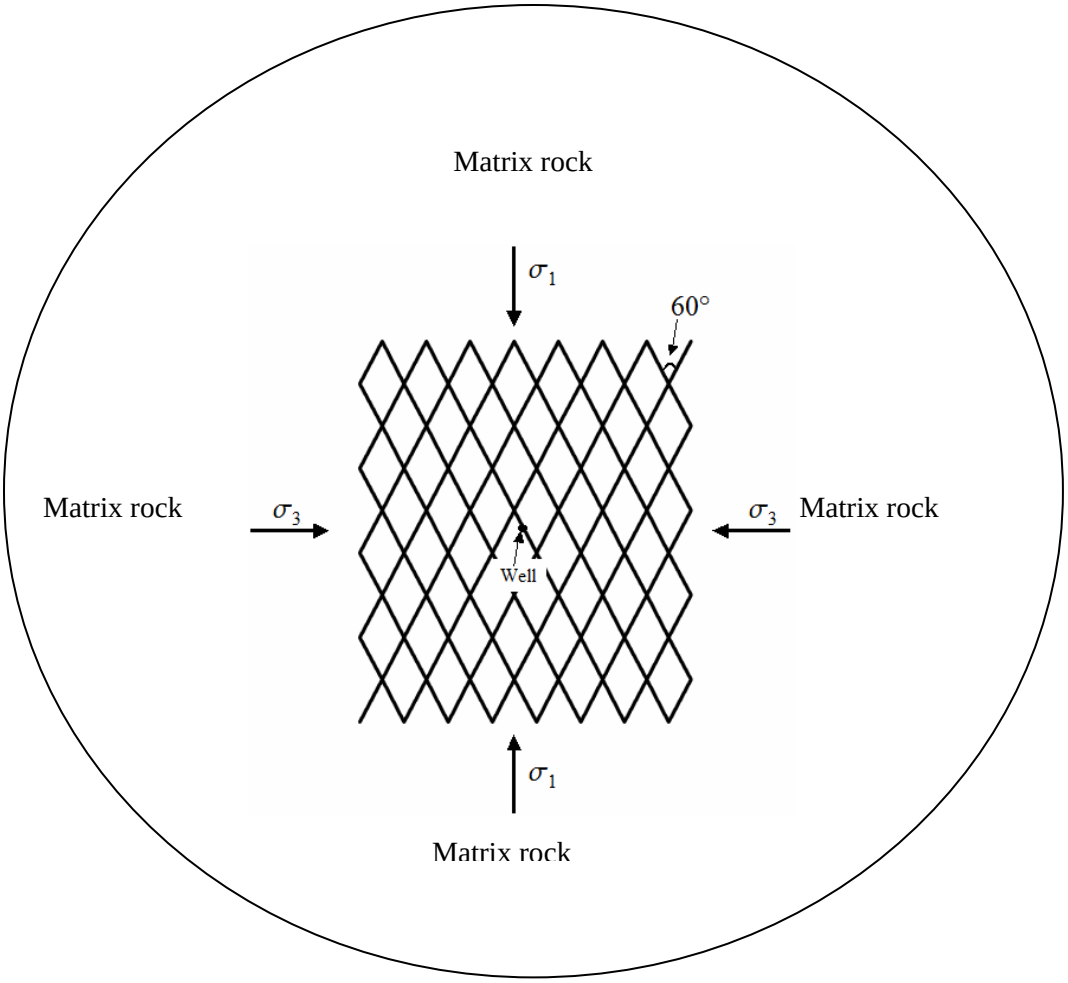

Figure V-23. Well located at the center of a fractured field under anisotropic stress field and the fractured network is surrounded by matrix rock.

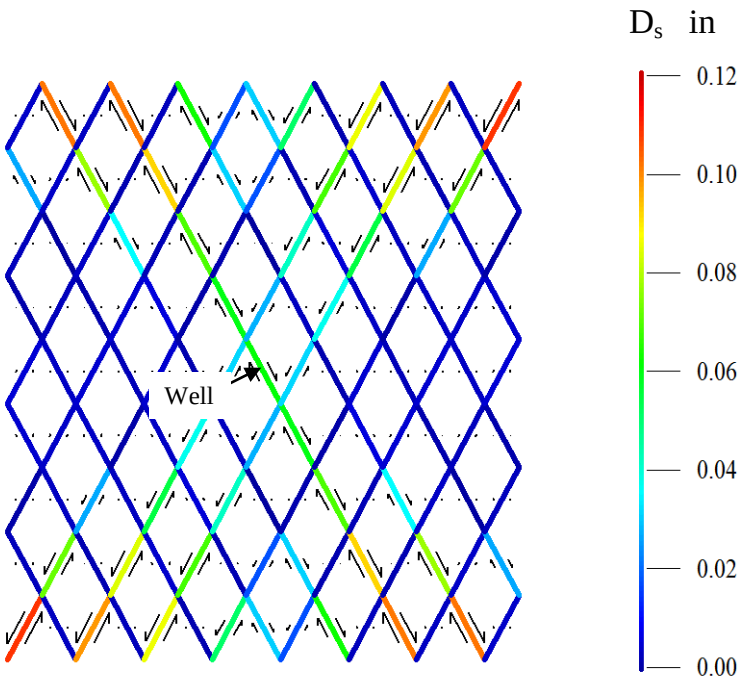

Figure V-24. Shear displacement distribution after 360 days production for the case fractures are already yielded before production. The arrow represents the shear direction.

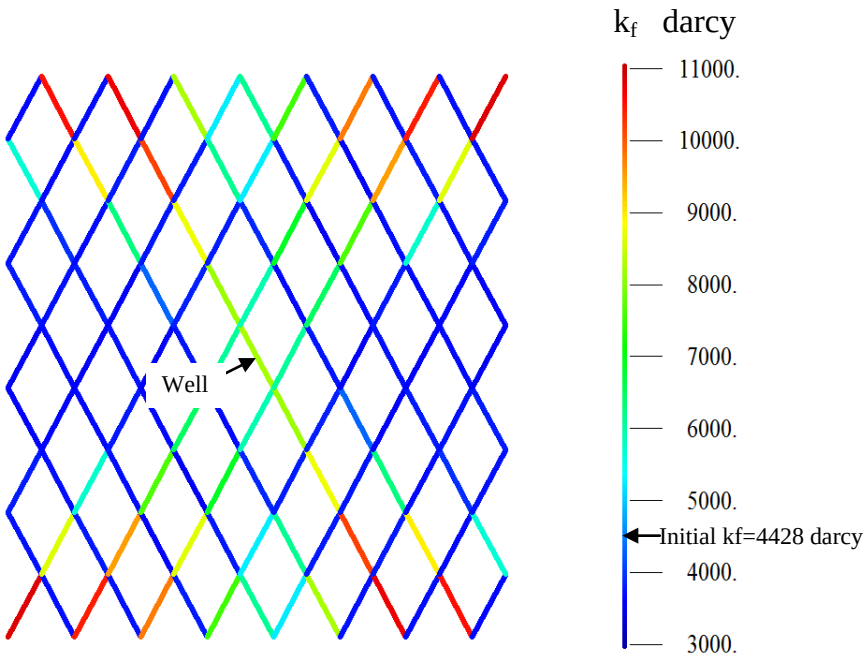

Figure V-25. Fracture permeability distribution after 360 days production for the case fractures are already yielded before production.

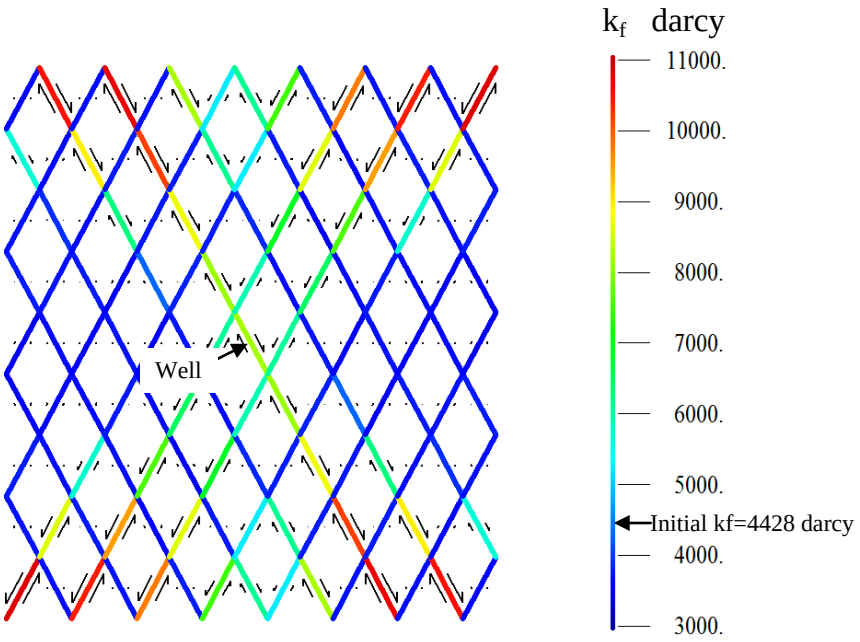

Figure V-26. Distribution of fracture permeability and shear displacement (shown with arrows) after 360 days production for the case fractures are already yielded before production.

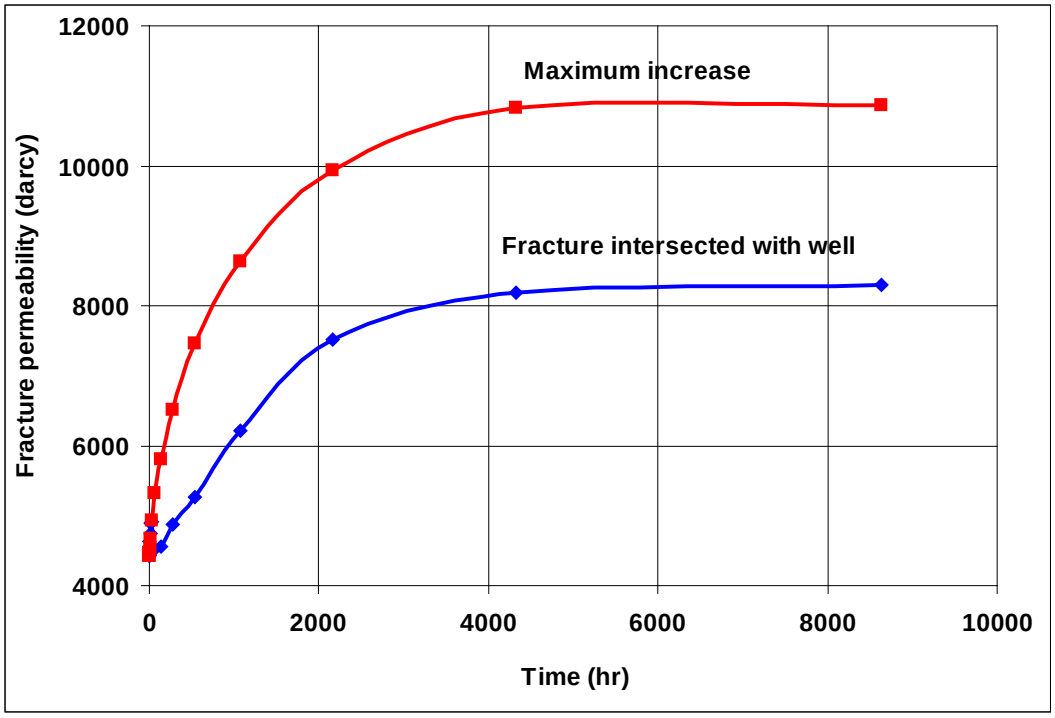

Figure V-27. Fracture permeability increases with production for the case the fracture are already yielded before production.

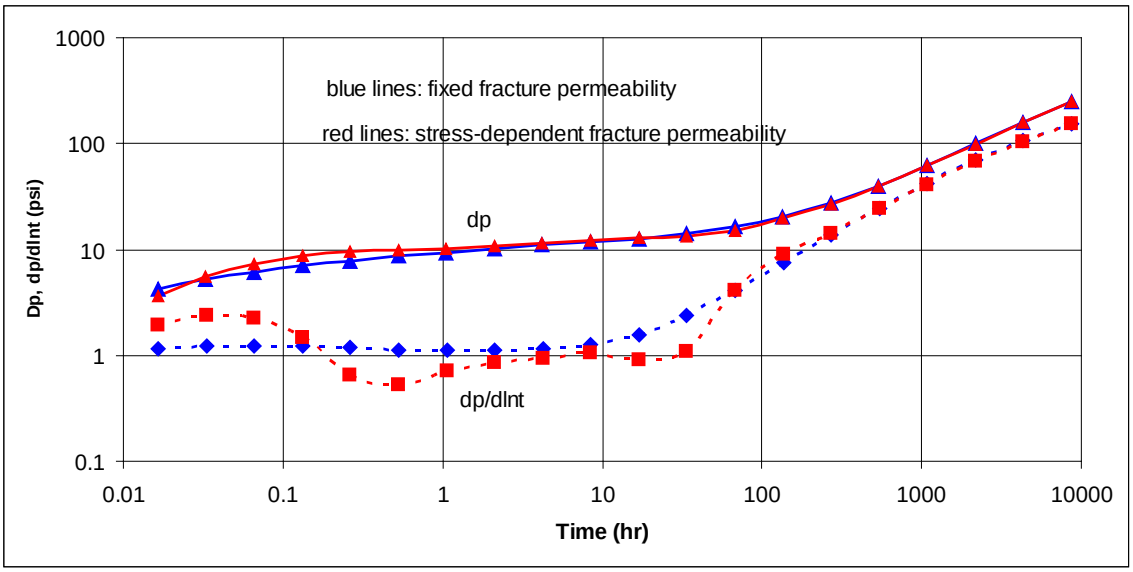

Figure V-28. Log-log plot of pressure drop and pressure derivative for the case in which the fracture permeability of most fractures are enhanced by production.

In Figure V-26 the shear displacement and fracture permeability distribution are not symmetric to lines through the well and parallel to x and y directions. For this case, neither the fracture network nor the fracture intersected with the well are symmetric. Before further comment on symmetries that do appear in this case, it is instructive to consider the example shown in Figure V-29 for a well producing from four fractures located at the center of the fracture network. In this case the resulting fracture network is symmetric about the well, and both the permeability and aperture changes are symmetric in x and y directions. It is now apparent that the asymmetries in Figure 5-27 arise from the asymmetries in both inner and outer boundary conditions.

In both cases permeability is enhanced in a similar way. Those fractures at the top and bottom which incline toward inside of the fracture network have larger shear displacement, thereby inducing higher permeability. As the whole fracture network is

compressed and moves inside with the reduction of reservoir pressure and the direction of maximum principal stress (Figure V-23) tends to have a larger displacement than the direction of minimum principal stress.

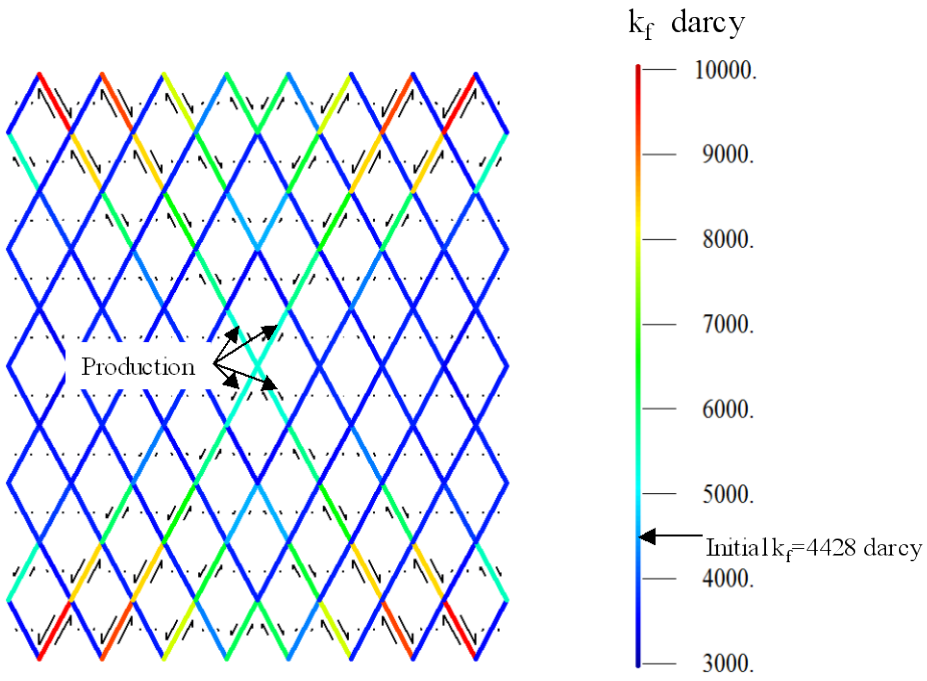

Figure V-29. Distribution of fracture permeability and shear displacement (shown with arrows) after 360 days production for the case with symmetric fracture network and production wells.

5.3 Chapter conclusions

This chapter provided applications of the method described in Chapter IV under isotropic in situ stress conditions and highly anisotropic in situ stress conditions. Fracture aperture and permeability decrease with pressure depletion in naturally fractured reservoirs under isotropic stress conditions, and the magnitude of the decrease is dependent on the initial effective in situ stress. For low initial effective in situ stress

(the reservoir pressure is very close to the magnitude of stress), the normal stiffness is small if the initial normal stiffness is small, i.e., weak fractures. The small change of reservoir pressure and effective stress can induce large fracture closure and permeability loss. But for hard rock (high initial normal stiffness) or high effective in situ stress, the normal stiffness is large, and the changes in fracture aperture and permeability are small even for large reservoir pressure change. For rough fractures, the effective hydraulic aperture is smaller than the average mechanical aperture. If the difference is neglected, the influence of production on the fracture permeability reduction at isotropic stress conditions will be underestimated. For highly anisotropic stress, the fractures can be at the critical stress condition and even a small change in the shear stress can induce large shear displacement. As a result, the fracture aperture and permeability can be enhanced due to shear dilation while the reservoir pressure is declining.

CHAPTER VI

CONCLUSIONS AND RECOMMENDATIONS

Production in naturally fractured reservoirs will cause reservoir pressure change, thereby changing the stress. The stress change will change the fracture aperture and permeability, thereby influencing the production. The coupled interactions exist in the fractured porous media: (i) fluid pressure change induces solid deformation and stress change; (ii) stress change induces fluid volume change and fluid pressure change; (iii) fracture deformation induces the change of pore pressure and stress in the whole field (the influence disappears at infinity); (iv) the change of pore pressure and stress at any point has an influence on the fracture and induces fracture deformation. A method is developed in this study to consider all of these coupled processes to model the fracture aperture and permeability change during production in naturally fractured reservoirs.

6.1 Conclusions

The main contributions and conclusions from this study are summarized as follows:

1. A method is developed to combine the fully coupled DDM with the Barton-Bandis model of fracture deformation. The fully coupled DDM gives the global fracture deformation and the Barton-Bandis fracture deformation model gives the local fracture deformation. The combination of the fully

coupled DDM and the Barton-Bandis fracture deformation model makes every fracture deformation comply with both local and global relations.

2. Fracture aperture and permeability decrease with pressure reduction caused by production in naturally fractured reservoirs under isotropic stress conditions, but the magnitude of the changes are dependent on the initial effective in situ stress. For low initial effective in situ stress (the reservoir pressure is very close to the magnitude of stress), the normal stiffness is small if the initial normal stiffness is small, i.e., weak fractures. The small change of reservoir pressure and effective stress can induce large fracture closure and permeability loss. But for hard rock (high initial normal stiffness) or high effective in situ stress, the normal stiffness is large. The change of fracture aperture and permeability is small even for large reservoir pressure change. Therefore, whether the reservoir is stress sensitive can be decided by laboratory tests on the properties of fractures and field tests of the in situ stress. For stress sensitive fractured reservoirs, the method developed in this study can be applied to evaluate the change of fracture permeability during production and its influence on production.
3. For rough fractures, the effective hydraulic aperture is smaller than the average mechanical aperture. If the difference is neglected, the influence of pressure reduction caused by production on the fracture permeability reduction under isotropic stress conditions will be underestimated.

4. For highly anisotropic stress, the fractures can be at the critical stress condition, and a small change of the shear stress can induce large shear displacement. The fracture aperture and permeability can be enhanced due to shear dilation while the reservoir pressure is decreasing.

6.2 Recommendations

The model is only for two-dimensional single-phase flow in a naturally fractured porous medium. A three-dimensional model will be better to consider the influences from all three principal stresses – the maximum horizontal stress, the minimum horizontal stress and the vertical stress. Single-phase flow rate is a simplified case for oil and gas reservoirs, and future work should consider two-phase or three-phase flow.

NOMENCLATURE

α	=	Biot's poroelastic coefficient
β	=	Angle counterclockwise from the x-axis to fracture segment.
γ^{ij}	=	$\pi/2+\beta_i-\beta_j$
ϕ	=	porosity
ϕ_d	=	dilation angle
ϕ_b	=	basic friction angle
ϕ_i	=	internal friction angle
ϕ_r	=	residual friction angle
ρ_f	=	fluid density
σ	=	stress tensor
σ_c	=	shear strength
σ'_n	=	effective normal stress
τ	=	shear strength
τ_ξ , τ_h	=	step time
τ_{peak}	=	peak shear strength
μ	=	fluid viscosity
υ	=	Poisson's ratio
υ_u	=	undrained Poisson's ratio

ζ_p	=	pore space change
ζ_s	=	solid grain deformation
ΔL	=	fracture length
a	=	half length of fracture segment
aa, b	=	constants related with fracture normal deformation
c	=	fluid diffusivity
c_0	=	cohesive strength
c_f	=	fluid compressibility
c_{fr}	=	fracture compressibility
c_t	=	total compressibility of fracture
c_{mt}	=	total compressibility of matrix
e	=	strain tensor
$f(x,y)$	=	a function defined in Eq. (2-2)
$\bar{f}(\bar{x},\bar{y})$	=	a function defined in Eq. (2-5)
k	=	permeability
k_f	=	fracture permeability
n	=	V_{ef}/V_f
p	=	pore pressure
q	=	flow rate
q_f	=	flow rate through fracture
q_{int}	=	interface flow rate between fracture and matrix /fluid source

q_s	=	injection/production rate
t	=	time
u	=	displacement
v	=	interface flow
w_f	=	fracture aperture
w_{ef}	=	effective hydraulic fracture aperture
x,y	=	co-ordinate positions in the global co-ordinate system
$\bar{x}$, $\bar{y}$	=	co-ordinate positions in the local co-ordinate system
$\overset{ij}{A}$	=	influence coefficient for normal stress by the normal displacement discontinuity defined in Eq. (2-10) for the elastic DDM or in Eq. (2-38) for the poroelastic DDM
$\overset{ij}{B}$	=	influence coefficient for normal stress by the shear displacement discontinuity defined in Eq. (2-10) for the elastic DDM or in Eq. (2-38) for the poroelastic DDM
$\overset{ij}{C}$	=	influence coefficient for normal stress by fluid source/interface flow rate defined in Eq. (2-38)
D	=	fracture displacement
D_n	=	normal fracture displacement
D_s	=	shear fracture displacment
D_{nmax}	=	maximum possible closure
$\overset{ij}{E}$	=	influence coefficient for shear stress by the normal displacement discontinuity defined in Eq. (2-10) for the elastic DDM or in Eq. (2-38) for the poroelastic DDM

F_{ij}	=	influence coefficient for shear stress by the shear displacement discontinuity defined in Eq. (2-10) for the elastic DDM or in Eq. (2-38) for the poroelastic DDM
G	=	shear modulus
H_{ij}	=	influence coefficient for pore pressure by the shear displacement discontinuity defined in Eq. (2-38)
JCS	=	joint compressive strength
JRC	=	joint roughness coefficient
K_{ij}	=	influence coefficient for shear stress by fluid source/interface flow rate defined in Eq. (2-38)
K_m	=	system bulk modulus
K_{ni}	=	initial normal stiffness
K_n	=	normal stiffness
K_s	=	shear stiffness or solid bulk modulus
L_{ij}	=	influence coefficient for pore pressure by the normal displacement discontinuity defined in Eq. (2-38)
M	=	Biot Modulus
N_{ij}	=	influence coefficient for pore pressure by fluid source/interface flow rate defined in Eq. (2-38)
S	=	fracture spacing
V_f	=	actual fracture void volume or pore space
V_{ef}	=	effective fracture void volume for fluid flow

Subscripts

0	=	initial
ξ	=	current time step
d	=	dilation
ef	=	effective
f	=	fluid or fracture
fr	=	fracture
h	=	index of time step
i, j	=	index of fracture segment
i	=	internal
inj	=	injection
int	=	interface
kk	=	bulk value
m	=	porous media system
mt	=	total of the porous media system
max	=	maximum
n	=	normal
o	=	oil
p	=	pore space
s	=	shear, solid/porous matrix, or source term
x,y,z	=	co-ordinate direction in the global co-ordinate system
$\bar{x}$, $\bar{y}$	=	co-ordinate direction in local co-ordinate system

Superscripts

q	=	fluid injection source/interface flow rate between fracture and matrix
dn	=	normal displacement discontinuity source
ds	=	shear displacement discontinuity source

Over scripts

ξ	=	Current time step
h	=	index of time step
i, j	=	index of fracture segment

REFERENCES

Aguilera, R., 1995. *Naturally Fractured Reservoirs (Second Edition)*. Tulsa, Oklahoma: Pennwell Books.

Asgian M., 1988. A Numerical Study of Fluid Flow in Deformable Naturally Fractured Reservoirs. Ph.D. dissertation, University of Minnesota, Minneapolis, Minnesota.

Asgian M., 1989. A Numerical-Model of Fluid-Flow in Deformable Naturally Fractured Rock Masses. *Int J. Rock Mech. Min. Sci.* **26** (3-4): 317-328.

Bagheri, M., 2006. Modeling Geomechanical Effects on the Flow Properties of Fractured Reservoirs. Ph.D. dissertation, University of Calgary, Calgary, Alberta, Canada.

Bagheri, M. and Setteri, A., 2008. Modeling of Geomechanics in Naturally Fractured Reservoirs. *SPEREE* **11** (1): 108-118.

Bandis, S.C., Lumsden, A.C. and Barton, N.R., 1981. Experimental Studies of Scale Effects on the Shear Behavior of Rock Joints. *Int J. Rock Mech. Min. Sci. and Geomech. Abstr.* **18** (1): 1-21.

Bandis, S.C., Lumsden, A.C. and Barton, N.R., 1983. Fundamentals of Rock Joint Deformation. *Int J. Rock Mech. Min. Sci. and Geomech. Abstr.* **20** (6): 249-268.

Barton N., 1976. The Shear Strength of Rock and Rock Joints. *Int. J. Rock Mech. Min. Sci. & Geomech. Abstr.* **13** (9): 255-279.

Barton, N. and Choubey, V., 1977. The Shear Strength of Rock Joints in Theory and Practice. *Rock Mech.* **10** (1-2): 1-54.

Barton, N., 1982. Modeliing Rock Joint Behaviour from *In Situ* Block Tests: Implications for Nuclear Waste Repository Design. Office of Nuclear Waste Isolation, Columbus, Ohio, ONWI-308, p. 96.

Barton, N., Bandis, S. and Bakhtar, K., 1985. Strength, Deformation and Conductivity Coupling of Rock Joints. *Int J. Rock Mech. Min. Sci. and Geomech. Abstr.* **22** (3): 121-140.

Biot, M.A.,1941. General Theory of Three-Dimensional Consolidation. *J. Appl. Phys.* **12** (2): 155-164.

Biot, M.A., 1956. General Solutions of the Equations of Elasticity and Consolidation for a Porous Material. *J. Appl. Mech., Trans. ASME* **78**, 91-96.

Boulon, M. J., Selvadurai, A. P. S., Benjelloun, Z. H., and Feuga, B., 1993. Influence of Rock Joint Degradation on Hydraulic Conductivity. *Int. J. Rock Mech. Min. Sci., Geomech. Abstr*. **30** (7): 1311-1317.

Buchsteiner, H., Warpinski, N.R. and Economides, M.J., 1993. Stress-Induced Permeability Reduction in Fissured Reservoirs. Paper SPE 26513 presented at 1993 SPE Annual Technical Conference and Exhibition, Houston, Texas, 3-6 October.

Byerlee, J. D., 1978. Friction of Rocks. *Pure Appl. Geophys.* **116** (4-5): 615–626.

Carvalho, J.L., 1990. Poroelastic Effects and Influence of Material Interfaces on Hydraulic Fracturing. Ph.D. dissertation, University of Toronto, Toronto, Canada.

Chen, H.Y., and Teufel, L.W., 1997. Coupling Fluid-Flow and Geomechanics in Dual-Porosity Modeling of Naturally Fractured Reservoirs. Paper SPE 38884 presented at 1997 SPE Annual Technical Conference and Exhibition, San Antonio, Texas, 5-8 October.

Cheng, A.H.-D. and Predeleanu, M., 1987. Transient Boundary Element Formulation for Linear Poroelasticity. *Applied Mathematical Modelling* **11** (4): 285–290.

Chin, L. Y., Raghavan, R., and Thomas, L. K., 1998. Fully Coupled Analysis of Well Responses in Stress-Sensitive Reservoirs. Paper SPE 48967 presented at the 1998 SPE Annual Technical Conference & Exhibition, New Orleans, Louisiana, 27-30 September.

Cinco, H. and Samaniego, F., 1982. Pressure Transient Analysis for Naturally Fractured Reservoirs. Paper SPE 11026 presented at the 1982 SPE Annual Technical Conference and Exhibition, New Orleans, Louisiana, 26-29 September.

Crouch S.L. and Starfield A.M, 1983. *Boundary Element Methods in Solid Mechanics*. London: Allen & Unwin.

Curran, J.H. and Carvalho, J.L., 1987. A Displacement Discontinuity Model for Fluid-Saturated Porous Media. Proc. 6th Cong. Int. Soc. Rock Mech., Vol. 1, Montreal, 1987.

Davies, J. P., and Davies, D. K., 1999. Stress-Dependent Permeability: Characterization and Modeling. Paper SPE 56813 presented at the 1999 SPE Annual Technical Conference and Exhibition, Houston, Texas, 3-6 October.

De Swaan, A., 1976. Analytical Solutions for Determining Naturally Fractured Reservoir Properties by Well Testing. *SPEJ* **16** (3): 117-122.

Detournay, E. and Cheng, A.H.-D., 1988. Poroelastic Response of a Borehole in a Non-Hydrostatic Stress Field. *Int. J. Rock Mech. Min. Sci. Geomech. Abstr.* **25** (3): 171–182.

Goodman R.E., 1976. *Methods of Geological Engineering in Discontinuous Rocks*. New York: West Publication Company.

Gray, D. H., Fatt, I., and Bergamini, G., 1963. The Effect of Stress on Permeability of Sandstone Cores. *SPEJ* **3** (2): 95-100.

Gutierrez, M., and Makurat, A.. 1997. Coupled THM Modelling of Cold Water Injection in Fractured Hydrocarbon Reservoirs. *Int J. Rock Mech. Min. Sci.* **34** (3–4): 429-443.

Huang, T.H., Chang, C.S. and Chao C.Y., 2002. Experimental and Mathematical Modeling for Fracture of Rock Joint with Regular Asperities. *Eng. Fract. Mech.* **69** (17): 1977–1996.

ISRM Commission on Standardization of Laboratory and Field Test, 1978. Suggested Methods for the Quantitative Description of Discontinuities in Rock Masses. *Int. J. Rock Mech. Min. Sci. Geomech. Abstr.* **15** (6): 319–368.

Iwai, K., 1976. Fundamental Studies of Fluid Flow Through a Single Fracture. Ph.D. dissertation, University of California, Berkeley, California.

Jones, F.O. and Owens, W.W., 1980. A Laboratory Study of Low-Permeability Gas Sands. *JPT* **32** (9): 1631-1640.

Lee, H.S. and Cho, T.F., 2002. Hydraulic Characteristics of Rough Fractures in Linear Flow Under Normal and Shear Load. *Rock Mech. Rock Eng.* **35** (4): 299–318.

Lee, J., Rollins, J. and Spivey, J., 2003. *Pressure Transient Testing*. Richardson, Texas: *SPE Textbook Series* Vol. 9.

Lewis, R.W., and Ghafouri, H.R., 1997. A Novel Finite Element Double Porosity Model for Multiphase Flow Through Deformable Fractured Porous Media. *Int. J. Numer. Anal. Methods Geomech.* **21** (11): 789–816.

Meng, F., 1998. Three-Dimensional Modeling of Two-Phase Fluid Flow in Deformable Fractured Reservoirs. Ph.D. dissertation, University of Oklahoma, Norman, Oklahoma.

Min, K.-B., Rutqvist, J., Tsang, C. -F., Jing, L., 2004. Stress-Dependent Permeability of Fractured Rock Masses: A Numerical Study. *Int. J. Rock Mech. Min. Sci.* **41** (7): 1191–1210.

Najurieta, H., 1980. A Theory for Pressure Transient Analysis in Naturally Fractured Reservoirs. *JPT* **32** (7): 1241-1250.

Nelson, R.A., 1985. *Geologic Analysis of Naturally Fractured Reservoirs*. Houston, Texas: Gulf Publishing Company.

Olson, R. and Barton, N., 2001. An Improved Model for Hydromechanical Coupling During Shearing of Rock Joints. *Int. J. Rock Mech. Min. Sci.* **38** (3): 317–329.

Ostensen, R. W., 1986. The Effect of Stress-Dependent Permeability on Gas Production and Well Testing. *SPEFE* **1** (3): 227-235.

Raghavan, R., Scorer, J. D. T., and Miller, F. G., 1972. An Investigation by Numerical Methods of the Effect of Pressure-Dependent Rock and Fluid Properties on Well Flow Tests. *SPEJ* **12** (3): 267-275.

Rice, J.R. and Cleary, M.P., 1976. Some Basic Stress Diffusion Solutions for Fluid-Saturated Elastic Porous Media With Compressible Constituents. *Rev. Geophys.* **14** (2): 227–241.

Samaniego V, F., Brigham, W. E., and Miller, F. G., 1976. Performance-Prediction Procedure for Transient Flow of Fluids Through Pressure-Sensitive Formations. Paper SPE 6051 presented at the SPE-AIME 51st Annual Fall Technical Conference & Exhibition, New Orleans, Louisiana, 3-6 October.

Samaniego V., F., Brigham, W. E., and Miller, F. G., 1977. An Investigation of Transient Flow of Reservoir Fluids Considering Pressure-Dependent Rock and Fluid Properties. *SPEJ* **17** (2): 140-150.

Samaniego V., F. and Cinco-Ley, H., 1989. On the Determination of the Pressure-Dependent Characteristics of a Reservoir Through Transient Pressure Testing. Paper SPE 19774 presented at the 1989 SPE Annual Technical Conference and Exhibition, San Antonio, Texas, 8-11 October.

Shu, Z., 1999. A Dual-Porosity Model for Two-Phase Flow in Deformable Porous Media. Ph.D. dissertation, University of Oklahoma, Norman, Oklahoma.

Sneddon, I.N., 1951. *Fourier Transforms*. New York: McGraw-Hill.

Snow,D . T., 1965. A Parallel Plate Model of Fractured Permeable Media. Ph.D. dissertation, University of California, Berkeley, California.

Sun, Y., 1994. A Three-Dimensional Model for Transient Fluid Flow Through Fractured Porous Media. Ph.D. dissertation, University of Minnesota, Minneapolis, Minnesota.

Sun, Z., Gerrard, C. and Stephanson, O., 1985. Rock Joint Compliance Tests for Compression and Shear Load. *Int. J. Rock Mech. Min. Sci. & Geomech. Abstr.* **22** (4): 197-213.

Thomas, R. D. and Ward, D. C., 1972. Effect of Overburden Pressure and Water Saturation on Gas Permeability of Tight Sandstone Cores. *JPT* **24** (2): 120-124.

Vairogs J., Hearn, C. L., Dareing, D. W., and Rhoades, V. W., 1971. Effect of Rock Stress on Gas Production From Low-Permeability Reservoirs. *JPT* **23** (9): 1161-1167.

Vairogs J. and Rhoades, V.W., 1973. Pressure Transient Test in Formations Having Stress-Sensitive Permeability. *JPT* **25** (8): 965-970.

Vandamme L.M. and Roegiers J.C., 1990. Poroelasticity in Hydraulic Fracturing Simulators. *JPT* **42** (9): 1199-1203.

Warren, R.E. and Root, P.J., 1963. The Behavior of Naturally Fractured Reservoirs. *SPEJ* **3** (3): 245-255.

Witherspoon, P.A., Wang, J.S.Y., Iwai, K., and Gale, J. E., 1980. Validity of Cubic Law for Fluid Flow in a Deformable Rock Fracture. *Water Resour. Res.* **16** (6): 1016-1024.

APPENDIX A

FUNDAMENTAL SOLUTIONS FOR FLUID SOURCE

Induced pore pressure p^q, displacement u^q and stress σ^q by continuous unit fluid source along a line fracture segment.

$$r^2 = \left(x - x^{'}\right)^2 + y^2 \tag{A-1}$$

where x' varies from $-a$ to $+a$.

$$E_1(x) = \int_x^{\infty} \frac{e^{-u}}{u} du \tag{A-2}$$

$$\xi = \frac{r}{2\sqrt{ct}} \tag{A-3}$$

Induced pore pressure:

$$p^q = \frac{\mu}{4\pi k} \int_{-a}^{a} Ei\left(\xi^2\right) dx^{'} \tag{A-4}$$

Induced displacement:

$$u_x^q = \frac{\alpha\mu(1-2\upsilon)}{16\pi k G(1-\upsilon)} \left[2cte^{-\xi^2} - \frac{r^2 E_1(\xi^2)}{2} - 2ct\left(\ln r^2 + E_1(\xi^2)\right) \right]\Bigg|_{-a}^{a} \tag{A-5}$$

$$\begin{aligned} u_y^q = \frac{\alpha\mu(1-2\upsilon)}{16\pi k G(1-\upsilon)} \Bigg\{ & \left[-4ct \arctan\left(\frac{x-x^{'}}{y}\right) \right]\Bigg|_{-a}^{a} + y\int_{-a}^{a} E_1\left(\xi^2\right) dx^{'} \\ & - 4cty\int_{-a}^{a} \frac{e^{-\xi^2}}{r^2} dx^{'} \Bigg\} \end{aligned} \tag{A-6}$$

Induced stress:

$$\sigma_{xx}^{q}=\frac{\alpha\mu(1-2\upsilon)}{8\pi k(1-\upsilon)}\left\{\left[-\left(x-x'\right)\left(\frac{1}{\xi^2}-\frac{e^{-\xi^2}}{\xi^2}+E_1\left(\xi^2\right)\right)\right]\Bigg|_{-a}^{a}-2\int_{-a}^{a}E_1\left(\xi^2\right)dx'\right\} \quad \text{(A-7)}$$

$$\sigma_{yy}^{q}=\frac{\alpha\mu(1-2\upsilon)}{8\pi k(1-\upsilon)}\left[\left(x-x'\right)\left(\frac{1}{\xi^2}-\frac{e^{-\xi^2}}{\xi^2}+E_1\left(\xi^2\right)\right)\right]\Bigg|_{-a}^{a} \quad \text{(A-8)}$$

$$\sigma_{xy}^{q}=\frac{\alpha\mu(1-2\upsilon)}{8\pi k(1-\upsilon)}\left[-y\left(\frac{1}{\xi^2}-\frac{e^{-\xi^2}}{\xi^2}+E_1\left(\xi^2\right)\right)\right]\Bigg|_{-a}^{a} \quad \text{(A-9)}$$

APPENDIX B

FUNDAMENTAL SOLUTION FOR DISPLACEMENT DISCONTINUITIES SOURCE

1. Induced pore pressure, displacement and stress by the continuous unit normal displacement discontinuity along a line fracture segment.

Induced pore pressure:

$$p^{dn} = -\frac{G(\upsilon_u - \upsilon)}{2\pi\alpha r^2(1-2\upsilon)(1-\upsilon_u)}\left[-\frac{2(x-x')}{r^2}\left(1-e^{-\xi^2}\right)\right]\Bigg|_{-a}^{a} \tag{B-1}$$

Induced displacement:

$$u_x^{dn} = -\frac{1}{4\pi(1-\upsilon)}\left\{(1-2\upsilon)\ln|r| - \left(\frac{\upsilon_u-\upsilon}{1-\upsilon_u}\right)\left[\left(\ln r + \frac{E_1(\xi^2)}{2}\right) - \frac{\left(1-e^{-\xi^2}\right)}{2\xi^2}\right] + \frac{y^2}{r^2}\left[1+\left(\frac{\upsilon_u-\upsilon}{1-\upsilon_u}\right)\left(1-\frac{1}{\xi^2}+\frac{e^{-\xi^2}}{\xi^2}\right)\right]\right\}\Bigg|_{-a}^{a} \tag{B-2}$$

$$u_y^{dn} = -\frac{1}{4\pi(1-\upsilon)}\left\{-2(1-\upsilon)\arctan\left(\frac{x-x'}{y}\right)\ln|r| - \frac{(x-x')y}{r^2}\left[1+\left(\frac{\upsilon_u-\upsilon}{1-\upsilon_u}\right)\left(1-\frac{1}{\xi^2}+\frac{e^{-\xi^2}}{\xi^2}\right)\right]\right\}\Bigg|_{-a}^{a} \tag{B-3}$$

Induced stress:

$$\sigma_{xx}^{dn} = -\frac{G}{2\pi(1-\upsilon)}\left\{\frac{(x-x')^3-(x-x')y^2}{r^4}+\left(\frac{\upsilon_u-\upsilon}{1-\upsilon_u}\right)\right.$$
$$\left.\left[\frac{(x-x')^3-(x-x')y^2}{r^4}+\frac{3(x-x')y^2-(x-x')^3}{r^4}\frac{1-e^{-\xi^2}}{\xi^2}-\frac{2(x-x')y^2e^{-\xi^2}}{r^4}\right]\right\}\Bigg|_{-a}^{a} \quad \text{(B-4)}$$

$$\sigma_{yy}^{dn} = -\frac{G}{2\pi(1-\upsilon)}\left\{\frac{(x-x')^3+3(x-x')y^2}{r^4}+\left(\frac{\upsilon_u-\upsilon}{1-\upsilon_u}\right)\right.$$
$$\left.\left[\frac{(x-x')^3+3(x-x')y^2}{r^4}+\frac{(x-x')^3-3(x-x')y^2}{r^4}\frac{1-e^{-\xi^2}}{\xi^2}-\frac{2(x-x')^3e^{-\xi^2}}{r^4}\right]\right\}\Bigg|_{-a}^{a} \quad \text{(B-5)}$$

$$\sigma_{xy}^{dn} = -\frac{G}{2\pi(1-\upsilon)}\left\{\frac{(x-x')^2y-y^3}{r^4}+\left(\frac{\upsilon_u-\upsilon}{1-\upsilon_u}\right)\right.$$
$$\left.\left[\frac{(x-x')^2y-y^3}{r^4}-\frac{3(x-x')^2y-y^3}{r^4}\frac{1-e^{-\xi^2}}{\xi^2}+\frac{2(x-x')^2ye^{-\xi^2}}{r^4}\right]\right\}\Bigg|_{-a}^{a} \quad \text{(B-6)}$$

where v_u is the undrained Poisson's ratio.

2. Induced pore pressure, displacement and stress by the continuous unit shear displacement discontinuity along a line fracture segment.

Induced pore pressure:

$$p^{ds} = -\frac{G(\upsilon_u-\upsilon)}{2\pi\alpha r^2(1-2\upsilon)(1-\upsilon_u)}\left[\frac{2y}{r^2}\left(1-e^{-\xi^2}\right)\right]\Bigg|_{-a}^{a} \quad \text{(B-7)}$$

Induced displacement:

$$u_x^{ds} = -\frac{1}{4\pi(1-\upsilon)}\left\{-2(1-\upsilon)\arctan\left(\frac{x-x'}{y}\right)\ln|r| + \frac{(x-x')y}{r^2}\left[1+\left(\frac{\upsilon_u-\upsilon}{1-\upsilon_u}\right)\left(1-\frac{1}{\xi^2}+\frac{e^{-\xi^2}}{\xi^2}\right)\right]\right\}\Bigg|_{-a}^{a} \tag{B-8}$$

$$u_y^{ds} = -\frac{1}{4\pi(1-\upsilon)}\left\{-(1-2\upsilon)\ln|r| + \left(\frac{\upsilon_u-\upsilon}{1-\upsilon_u}\right)\left[\left(\ln r + \frac{E_1(\xi^2)}{2}\right)+\frac{\left(1-e^{-\xi^2}\right)}{2\xi^2}\right] + \frac{y^2}{r^2}\left[1+\left(\frac{\upsilon_u-\upsilon}{1-\upsilon_u}\right)\left(1-\frac{1}{\xi^2}+\frac{e^{-\xi^2}}{\xi^2}\right)\right]\right\}\Bigg|_{-a}^{a} \tag{B-9}$$

Induced stress:

$$\sigma_{xx}^{ds} = -\frac{G}{2\pi(1-\upsilon)}\left\{-\frac{3(x-x')^2y+y^3}{r^4}+\left(\frac{\upsilon_u-\upsilon}{1-\upsilon_u}\right)\left[-\frac{3(x-x')^2y+y^3}{r^4}+\frac{3(x-x')^2y-y^3}{r^4}\frac{1-e^{-\xi^2}}{\xi^2}+\frac{2y^3e^{-\xi^2}}{r^4}\right]\right\}\Bigg|_{-a}^{a} \tag{B-10}$$

$$\sigma_{yy}^{ds} = -\frac{G}{2\pi(1-\upsilon)}\left\{\frac{(x-x')^2y-y^3}{r^4}+\left(\frac{\upsilon_u-\upsilon}{1-\upsilon_u}\right)\left[\frac{(x-x')^2y-y^3}{r^4}-\frac{3(x-x')^2y-y^3}{r^4}\frac{1-e^{-\xi^2}}{\xi^2}+\frac{2(x-x')^2ye^{-\xi^2}}{r^4}\right]\right\}\Bigg|_{-a}^{a} \tag{B-11}$$

$$\sigma_{xy}^{ds} = -\frac{G}{2\pi(1-\upsilon)}\left\{\frac{(x-x')^3-(x-x')y^2}{r^4}+\left(\frac{\upsilon_u-\upsilon}{1-\upsilon_u}\right)\right.$$
$$\left.\left[\frac{(x-x')^3-(x-x')y^2}{r^4}+\frac{3(x-x')y^2-(x-x')^3}{r^4}\frac{1-e^{-\xi^2}}{\xi^2}-\frac{2(x-x')y^2e^{-\xi^2}}{r^4}\right]\right\}\Bigg|_{-a}^{a} \quad \text{(B-12)}$$

APPENDIX C

COEFFICIENT MATRIX, $\overset{ij}{C}_p$, FOR FLUID DIFFUSION IN A REGULAR FRACTURE NETWORK

For a regular fracture network with *nc* columns and *nr* rows, the fracture segment divided by the intersection points is the discretized fracture element. The fracture segment is numbered according to the row (*ir*) and column (*jc*) as:

$$nf = (ir - 1) \times nc + jc \tag{C-1}$$

where *nf* is the index of fracture segment in the discretized fracture network. The fracture segments are divided into two types – type (*a*) and type (*b*) according to the orientation shown in Figure C-1. For any fracture segment (*i, j*) of type (*a*), there are 6 fracture segments directly connected with the segment and they are (*i, j-1*), (*i, j+1*), (*i-1, j*), (*i+1, j*), (*i-1, j-1*), (*i+1, j+1*) shown in Figure C-2. For any fracture segment (*i, j*) of type (b), there are also 6 fracture segments directly connected with the segment and they are (*i, j-1*), (*i, j+1*), (*i-1, j*), (*i+1, j*), (*i-1, j+1*), (*i+1, j-1*) shown in Figure C-3. Finally, for any fracture segment (*i, j*) of either type (*a*) or (*b*), the connected fracture segments can be expressed as (*i, j-1*), (*i, j+1*), (*i-1, j*), (*i+1, j*), (*i-1, j-(-1)*$^{j+1}$*×(-1)*$^{i+1}$), (*i+1, j+(-1)*$^{j+1}$*×(-1)*$^{i+1}$).

Using the Darcy's law, the flow rate from the directly connected fracture segments to the fracture segment (*i, j*) can be calculated.

From (*i, j-1*):

$$q_W = \frac{p^{l+1}(i, j-1) - p^{l+1}(i, j)}{\mu\left[\frac{a(i, j-1)}{k_f(i, j-1)\ w_f(i, j-1)} + \frac{a(i, j)}{k_f(i, j)\ w_f(i, j)}\right]} \tag{C-2}$$

From (*i, j+1*):

$$q_E = \frac{p^{l+1}(i, j+1) - p^{l+1}(i, j)}{\mu\left[\frac{a(i, j+1)}{k_f(i, j+1)\ w_f(i, j+1)} + \frac{a(i, j)}{k_f(i, j)\ w_f(i, j)}\right]} \tag{C-3}$$

From (*i-1, j*):

$$q_{S1} = \frac{p^{l+1}(i-1, j) - p^{l+1}(i, j)}{\mu\left[\frac{a(i-1, j)}{k_f(i-1, j)\ w_f(i-1, j)} + \frac{a(i, j)}{k_f(i, j)\ w_f(i, j)}\right]} \tag{C-4}$$

From (*i+1, j*):

$$q_{N1} = \frac{p^{l+1}(i+1, j) - p^{l+1}(i, j)}{\mu\left[\frac{a(i+1, j)}{k_f(i+1, j)\ w_f(i+1, j)} + \frac{a(i, j)}{k_f(i, j)\ w_f(i, j)}\right]} \tag{C-5}$$

From ($i-1, j-(-1)^{j+1}\times(-1)^{i+1}$):

$$q_{S2} = \frac{p^{l+1}\left(i-1, j-(-1)^{j+1}(-1)^{i+1}\right) - p^{l+1}(i, j)}{\mu\left[\frac{a\left(i-1, j-(-1)^{j+1}(-1)^{i+1}\right)}{k_f\left(i-1, j-(-1)^{j+1}(-1)^{i+1}\right)w_f\left(i-1, j-(-1)^{j+1}(-1)^{i+1}\right)} + \frac{a(i, j)}{k_f(i, j)w_f(i, j)}\right]} \tag{C-6}$$

From ($i+1, j+(-1)^{j+1}\times(-1)^{i+1}$):

$$q_{N2} = \frac{p^{l+1}\left(i+1, j+(-1)^{j+1}(-1)^{i+1}\right) - p^{l+1}(i, j)}{\mu\left[\frac{a\left(i+1, j+(-1)^{j+1}(-1)^{i+1}\right)}{k_f\left(i+1, j+(-1)^{j+1}(-1)^{i+1}\right)w_f\left(i+1, j+(-1)^{j+1}(-1)^{i+1}\right)} + \frac{a(i, j)}{k_f(i, j)w_f(i, j)}\right]} \tag{C-7}$$

where the superscript *l+1* denote the new time step, *a* is the half length of fracture segment, k_f is the fracture permeability, w_f is the fracture aperture. *a(i, j)*, $k_f(i, j)$ and $w_f(i, j)$ denote the half length, permeability and aperture of the fracture segment (*i, j*). The net flow rate into the fracture segment (*i, j*) is:

$$q_{net} = q_W + q_E + q_{S1} + q_{N1} + q_{S2} + q_{N2} \tag{C-8}$$

Substituting Eqs. (C-2)-(C-7) into Eq. (C-8) yields:

$$\begin{aligned} & q_{net} = \\ & COE_W p^{l+1}(i, j-1) + COE_E p^{l+1}(i, j+1) + COE_{S1} p^{l+1}(i-1, j) + COE_{N1} p^{l+1}(i+1, j) \\ & + COE_{S2} p^{l+1}\left(i-1, j-(-1)^{j+1}(-1)^{i+1}\right) + COE_{N2} p^{l+1}\left(i+1, j+(-1)^{j+1}(-1)^{i+1}\right) \\ & - \left(COE_W + COE_E + COE_{S1} + COE_{N1} + COE_{S2} + COE_{N2}\right) p^{l+1}(i, j) \end{aligned} \tag{C-9}$$

where

$$\begin{aligned} COE_W &= \frac{1}{\mu\left[\dfrac{a(i, j-1)}{k_f(i, j-1)\ w_f(i, j-1)} + \dfrac{a(i, j)}{k_f(i, j)\ w_f(i, j)}\right]} \\ COE_E &= \frac{1}{\mu\left[\dfrac{a(i, j+1)}{k_f(i, j+1)\ w_f(i, j+1)} + \dfrac{a(i, j)}{k_f(i, j)\ w_f(i, j)}\right]} \\ COE_{S1} &= \frac{1}{\mu\left[\dfrac{a(i-1, j)}{k_f(i-1, j)\ w_f(i-1, j)} + \dfrac{a(i, j)}{k_f(i, j)\ w_f(i, j)}\right]} \\ COE_{N1} &= \frac{1}{\mu\left[\dfrac{a(i+1, j)}{k_f(i+1, j)\ w_f(i+1, j)} + \dfrac{a(i, j)}{k_f(i, j)\ w_f(i, j)}\right]} \end{aligned} \tag{C-10}$$

$$COE_{S2} = \frac{1}{\mu\left[\dfrac{a\left(i-1,\, j-(-1)^{j+1}(-1)^{i+1}\right)}{k_f\left(i-1,\, j-(-1)^{j+1}(-1)^{i+1}\right)w_f\left(i-1,\, j-(-1)^{j+1}(-1)^{i+1}\right)} + \dfrac{a(i,j)}{k_f(i,j)w_f(i,j)}\right]}$$

$$COE_{N2} = \frac{1}{\mu\left[\dfrac{a\left(i+1,\, j+(-1)^{j+1}(-1)^{i+1}\right)}{k_f\left(i+1,\, j+(-1)^{j+1}(-1)^{i+1}\right)w_f\left(i+1,\, j+(-1)^{j+1}(-1)^{i+1}\right)} + \dfrac{a(i,j)}{k_f(i,j)w_f(i,j)}\right]}$$

The fluid volume change (the first right term in Eq. (4-10)) from the old time step *l* to new time step *l+1* in the fracture segment is:

$$COE_c\left(p^{l+1}(i,j) - p^{l+1}(i,j)\right) \tag{C-11}$$

where

$$COE_c = 2n\, w_f(i,j)a(i,j)c_o \tag{C-12}$$

The fracture length ΔL is substituted by $2a$ in Eq. (C-11).

Combining Eqs. (C-9) and (C-11), Eq. (4-10) for the fracture network in Figure C-1 is discretized into:

$$\begin{aligned}
&COE_W p^{l+1}(i,j-1) + COE_E p^{l+1}(i,j+1) + COE_{S1} p^{l+1}(i-1,j) + COE_{N1} p^{l+1}(i+1,j) \\
&+ COE_{S2} p^{l+1}\left(i-1,\, j-(-1)^{j+1}(-1)^{i+1}\right) + COE_{N2} p^{l+1}\left(i+1,\, j+(-1)^{j+1}(-1)^{i+1}\right) \\
&-\left(COE_W + COE_E + COE_{S1} + COE_{N1} + COE_{S2} + COE_{N2} + COE_c\right)p^{l+1}(i,j) \\
&= -COE_c p^l(i,j) - 2na(i,j)\Delta D_n + 2a(i,j)q_{\text{int}} + q_s
\end{aligned} \tag{C-13}$$

The index of fracture segment can be calculated from the row number and column number using Eq. (C-1). Therefore, Eq. (C-13) is rewritten using the index of fracture segment.

$$\begin{aligned} &C_p^{nf\,nf_W}\, p^{l+1}_{nf_W} + C_p^{nf\,nf_E}\, p^{l+1}_{nf_E} + C_p^{nf\,nf_{S1}}\, p^{l+1}_{nf_{S1}} + C_p^{nf\,nf_{N1}}\, p^{l+1}_{nf_{N1}} + C_p^{nf\,nf_{S2}}\, p^{l+1}_{nf_{S2}} + C_p^{nf\,nf_{N2}}\, p^{l+1}_{nf_{N2}} + C_p^{nf\,nf}\, p^{l+1}_{nf} \\ &= COE_c\, p^{l}_{nf} + 2n_a^{nf}\, \Delta D_n^{nf} - 2\, a^{nf\,nf}\, q_{\text{int}} - q_s^{nf} \end{aligned} \tag{C-14}$$

where

$$\begin{aligned} nf &= (i-1)\times nc + j \\ nf_W &= (i-1)\times nc + j - 1 \\ nf_E &= (i-1)\times nc + j + 1 \\ nf_{S1} &= (i-2)\times nc + j \\ nf_{N1} &= i\times nc + j \\ nf_{S2} &= (i-2)\times nc + j - (-1)^{j+1}(-1)^{i+1} \\ nf_{N2} &= i\times nc + j + (-1)^{j+1}(-1)^{i+1} \end{aligned} \tag{C-15}$$

$$\begin{aligned} &C_p^{nf\,nf_W} = -COE_W \quad C_p^{nf\,nf_E} = -COE_E \quad C_p^{nf\,nf_{S1}} = -COE_{S1} \\ &C_p^{nf\,nf_{N1}} = -COE_{N1} \quad C_p^{nf\,nf_{S2}} = -COE_{S2} \quad C_p^{nf\,nf_{N2}} = -COE_{N2} \\ &C_p^{nf\,nf} = COE_W + COE_E + COE_{S1} + COE_{N1} + COE_{S2} + COE_{N2} + COE_c \end{aligned} \tag{C-16}$$

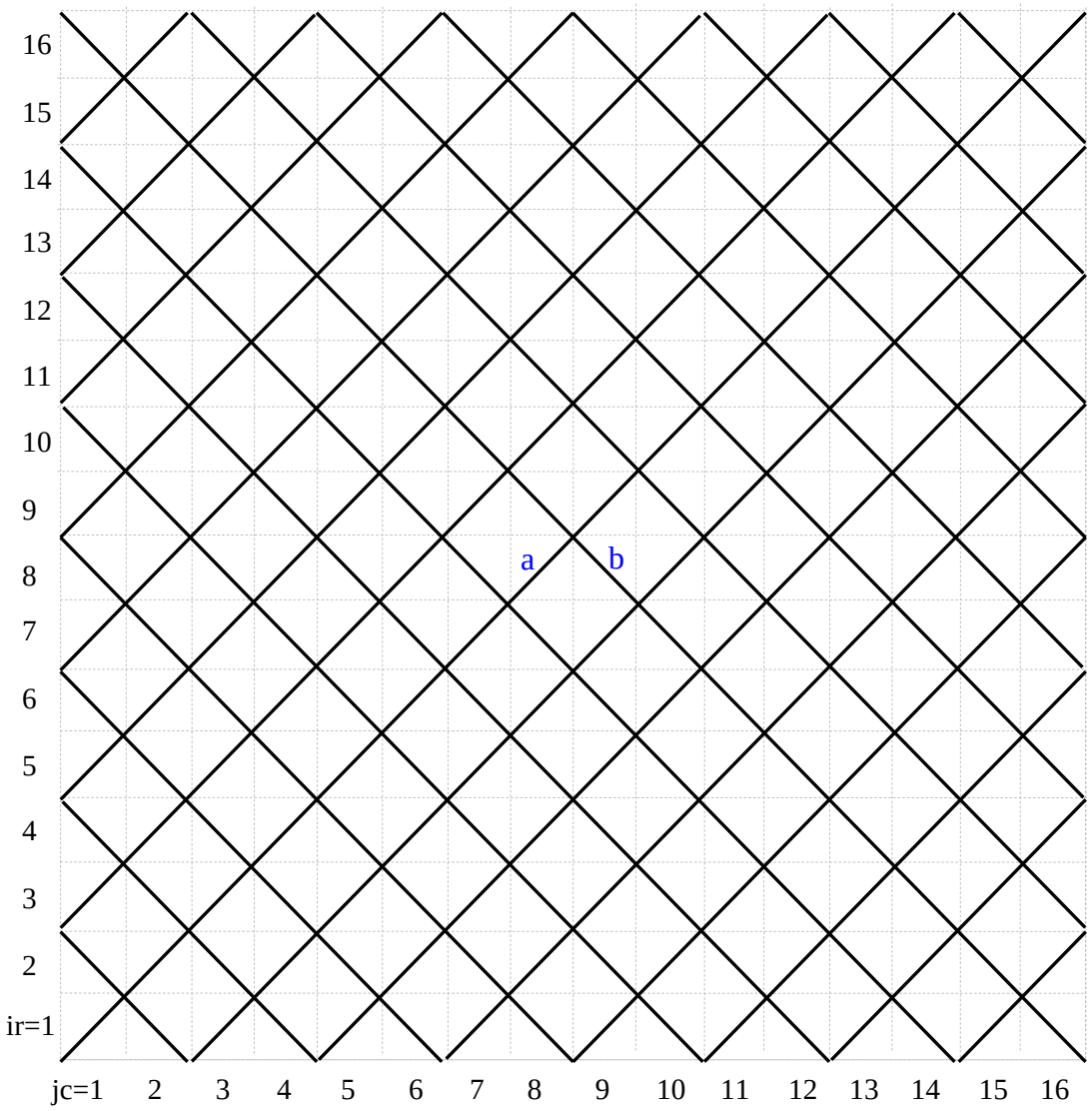

Figure C-1. A regular fracture network.

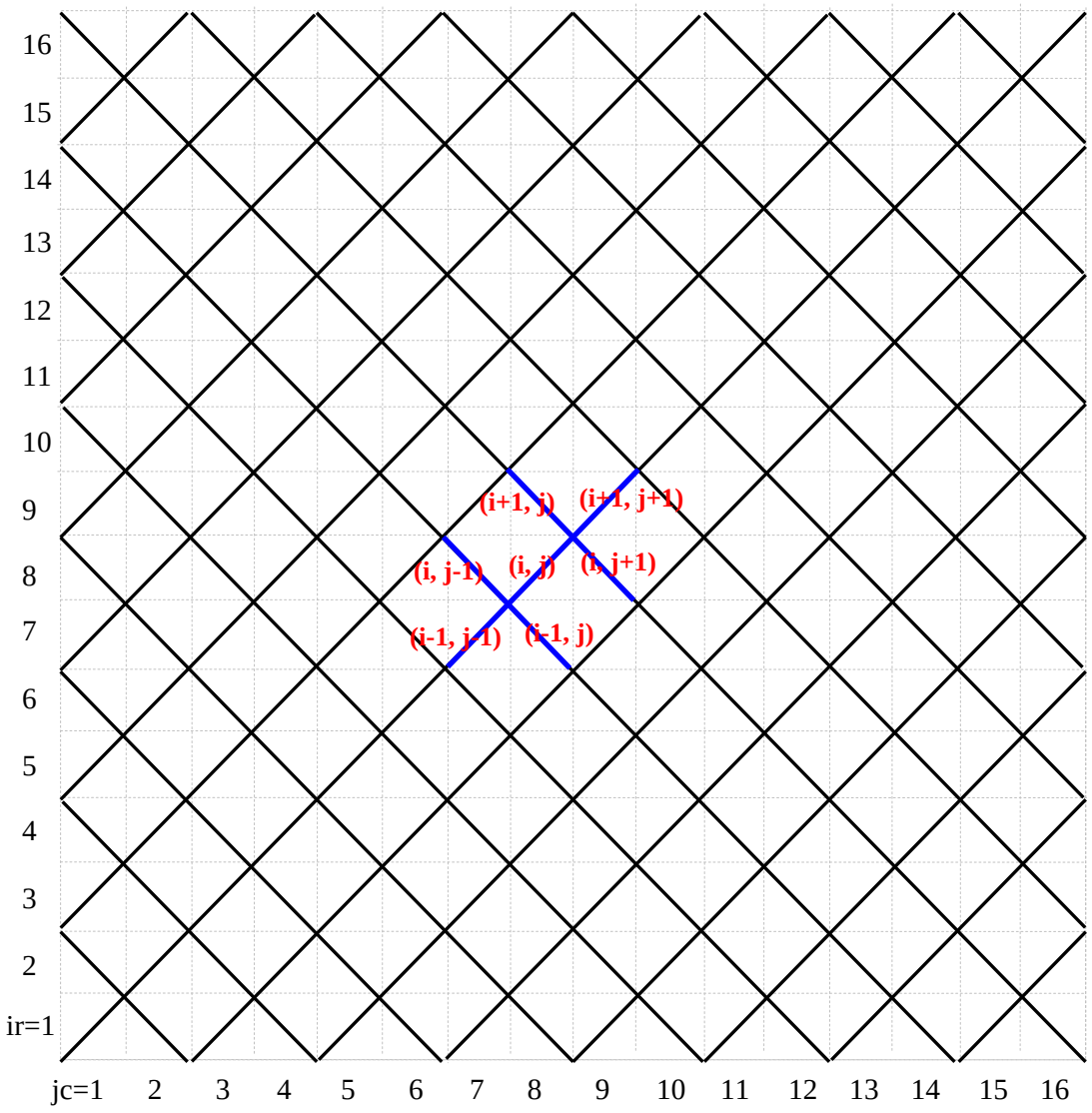

Figure C-2. Discretization of type (a) fracture segment.

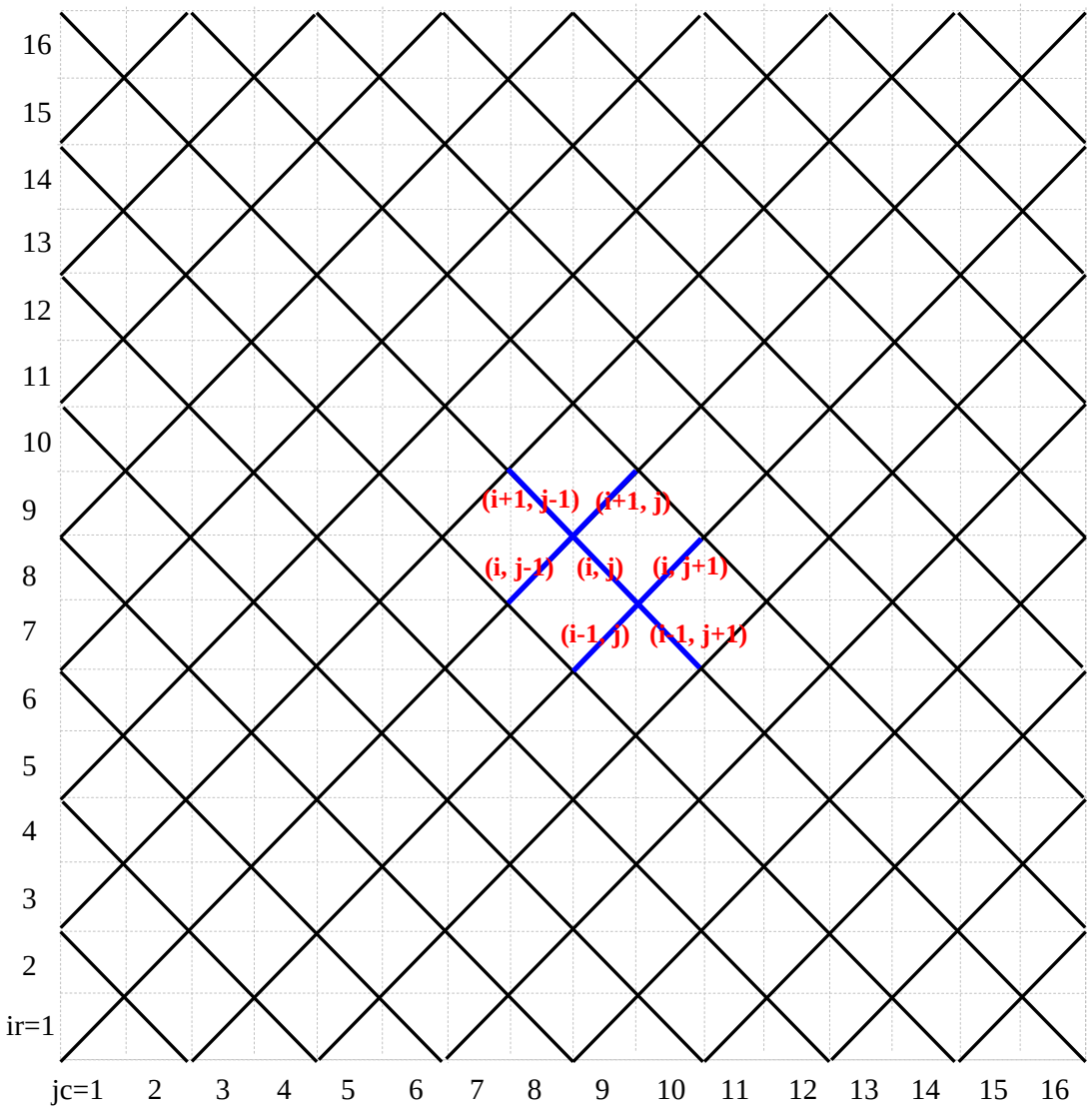

Figure C-3. Discretization of type (b) fracture segment.

APPENDIX D

COMBINED SET OF LINEAR EQUATIONS IN MATRIX FORM FOR A REGULAR FRACTURE NETWORK

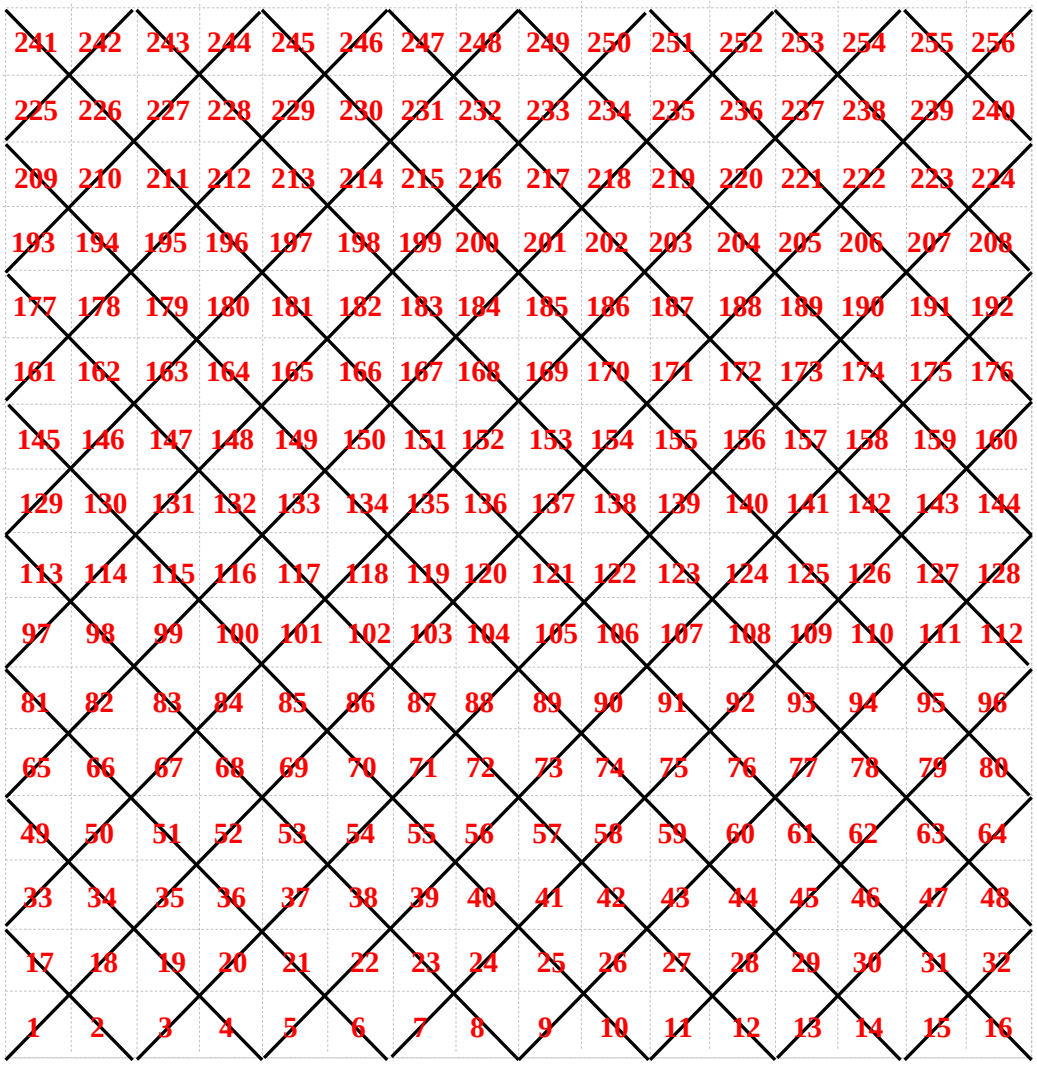

Figure D-1. A regular fracture network with indices of fracture segments.

For the fracture network and discretized fracture segments shown in Figure D-1, a set of linear equations can be built from Eqs. (4-30) and (4-31), and the unknowns (p,

ΔD_n, ΔD_s and Δq_{int}) for all fracture segments can be obtained by solving the following equations in matrix form.

$$
\begin{pmatrix}
1 & {}^{1,1}_{1}A+K_n & {}^{1,1}_{1}B+K_n\tan\phi_d & {}^{1,1}C & \cdots & 0 & {}^{1,i}A & {}^{1,i}B & {}^{1,i}C & \cdots & 0 & {}^{1,256}A & {}^{1,256}B & {}^{1,256}C \\
0 & {}^{1,1}E & {}^{1,1}_{1}F-K_s & {}^{1,1}K & \cdots & 0 & {}^{1,i}E & {}^{1,i}E & {}^{1,i}K & \cdots & 0 & {}^{1,256}A & {}^{1,256}B & {}^{1,256}C \\
-1 & {}^{1,1}L & {}^{1,1}H & {}^{1,1}N & \cdots & 0 & {}^{1,i}L & {}^{1,i}H & {}^{1,i}N & \cdots & 0 & {}^{1,256}L & {}^{1,256}H & {}^{1,256}N \\
{}^{1,1}C_p & -2n\,{}^{1}a & 0 & 2\,{}^{1}a & \cdots & {}^{1,i}C_p & 0 & 0 & 0 & \cdots & {}^{1,256}C_p & 0 & 0 & 0 \\
\vdots & \vdots & \vdots & \vdots & \ddots & \vdots & \vdots & \vdots & \vdots & \ddots & \vdots & \vdots & \vdots & \vdots \\
0 & {}^{i,1}A & {}^{i,1}B & {}^{i,1}C & \cdots & 1 & {}^{i,i}A+K_n & {}^{i,i}B+K_n\tan\phi_d & {}^{i,i}C & \cdots & 0 & {}^{i,256}A & {}^{i,256}B & {}^{i,256}C \\
0 & {}^{i,1}E & {}^{i,1}E & {}^{i,1}K & \cdots & & {}^{i,i}E & {}^{i,i}F-K_s & {}^{i,i}K & \cdots & 0 & {}^{i,256}E & {}^{i,256}F & {}^{i,256}K \\
0 & {}^{i,1}L & {}^{i,1}H & {}^{i,1}N & \cdots & -1 & {}^{i,i}L & {}^{i,i}H & {}^{i,i}N & \cdots & 0 & {}^{i,256}L & {}^{i,256}H & {}^{i,256}N \\
{}^{i,1}C_p & 0 & 0 & 0 & \cdots & {}^{i,i}C_p & -2n\,{}^{i}a & 0 & 2\,{}^{i}a & \cdots & {}^{i,256}C_p & 0 & 0 & 0 \\
\vdots & \vdots & \vdots & \vdots & \ddots & \vdots & \vdots & \vdots & \vdots & \ddots & \vdots & \vdots & \vdots & \vdots \\
0 & {}^{256,1}A & {}^{256,1}B & {}^{256,1}C & \cdots & 0 & {}^{256,i}A & {}^{256,i}B & {}^{256,i}C & \cdots & 1 & {}^{256,256}_{256}A+K_n & {}^{256,256}_{256}B+K_n\tan\phi_d & {}^{256,256}C \\
0 & {}^{256,1}E & {}^{256,1}F & {}^{256,1}K & \cdots & 0 & {}^{256,i}E & {}^{256,i}F & {}^{256,i}K & \cdots & 0 & {}^{256,256}E & {}^{256,256}_{256}F-K_s & {}^{256,256}K \\
0 & {}^{256,1}L & {}^{256,1}H & {}^{256,1}N & \cdots & 0 & {}^{256,i}L & {}^{256,i}H & {}^{256,i}N & \cdots & -1 & {}^{256,256}L & {}^{256}H & {}^{256}N \\
{}^{256,1}C_p & 0 & 0 & 0 & \cdots & {}^{256,i}C_p & 0 & 0 & 0 & \cdots & {}^{256,256}C_p & -2n\,{}^{256}a & 0 & 2\,{}^{256}a
\end{pmatrix}
\begin{pmatrix}
{}^{1}p(t) \\ {}^{1\xi}\Delta D_n \\ {}^{1\xi}\Delta D_s \\ {}^{1\xi}\Delta q_{\text{int}} \\ \vdots \\ {}^{i}p(t) \\ {}^{i\xi}\Delta D_n \\ {}^{i\xi}\Delta D_s \\ {}^{i\xi}\Delta q_{\text{int}} \\ \vdots \\ {}^{256}p(t) \\ {}^{256\xi}\Delta D_n \\ {}^{256\xi}\Delta D_s \\ {}^{256\xi}\Delta q_{\text{int}}
\end{pmatrix}
=
\begin{pmatrix}
{}^{1}bD_n \\ {}^{1}bD_s \\ {}^{1}bq_{\text{int}} \\ {}^{1}bp \\ \vdots \\ {}^{i}bD_n \\ {}^{i}bD_s \\ {}^{i}bq_{\text{int}} \\ {}^{i}bp \\ \vdots \\ {}^{256}bD_n \\ {}^{256}bD_s \\ {}^{256}bq_{\text{int}} \\ {}^{256}bp
\end{pmatrix}
\tag{D-1}
$$

where

$$
\begin{aligned}
{}^{i}bD_n &= -\sum_{h=0}^{\xi-1}\sum_{j=1}^{m}{}^{ij}A\left(t-\tau_h\right)\Delta\,{}^{jh}D_n - \sum_{h=0}^{\xi-1}\sum_{j=1}^{m}{}^{ij}B\left(t-\tau_h\right)\Delta\,{}^{jh}D_s - \sum_{h=0}^{\xi-1}\sum_{j=1}^{m}{}^{ij}C\left(t-\tau_h\right){}^{jh}q_{\text{int}} - {}^{i}K_n\left(\sum_{h=0}^{\xi-1}\Delta\,{}^{ih}D_n + \tan\phi_d\sum_{h=0}^{\xi-1}\Delta\,{}^{ih}D_s\right) + {}^{i}p_0 \\
{}^{i}bD_s &= -\sum_{h=0}^{\xi-1}\sum_{j=1}^{m}{}^{ij}E\left(t-\tau_h\right)\Delta\,{}^{jh}D_n - \sum_{h=0}^{\xi-1}\sum_{j=1}^{m}{}^{ij}F\left(t-\tau_h\right)\Delta\,{}^{jh}D_s - \sum_{h=0}^{\xi-1}\sum_{j=1}^{m}{}^{ij}K\left(t-\tau_h\right){}^{jh}q_{\text{int}} + {}^{i}K_s\sum_{h=0}^{\xi-1}\Delta\,{}^{ih}D_s \\
{}^{i}bq_{\text{int}} &= -{}^{i}p_0 - \sum_{h=0}^{\xi-1}\sum_{j=1}^{m}{}^{ij}L\left(t-\tau_h\right)\Delta\,{}^{jh}D_n - \sum_{h=0}^{\xi-1}\sum_{j=1}^{m}{}^{ij}H\left(t-\tau_h\right)\Delta\,{}^{jh}D_s - \sum_{h=0}^{\xi-1}\sum_{j=1}^{m}{}^{ij}N\left(t-\tau_h\right){}^{jh}q_{\text{int}} \\
{}^{i}bp &= 2n\,w_f\,{}^{i}a\,{}^{i}c_f\,{}^{i}p(\tau_\xi) - \Delta L\sum_{h=0}^{\xi-1}\Delta\,{}^{ih}q_{\text{int}} - \sum_{h=0}^{\xi}{}^{ih}q_s
\end{aligned}
\tag{D-2}
$$

VITA

Name:	Qingfeng Tao
Address:	Department of Petroleum Engineering, Texas A&M University, College Station, TX 77840
Email Address:	taoqingfeng@gmail.com
Education:	B.S., Geology, China University of Geosciences, 2000 M.S., Geological Engineering, The University of North Dakota, 2006